Università degli Studi Roma TRE

e

Consorzio Nazionale Interuniversitario per le Scienze Fisiche della Materia

Dottorato di Ricerca in Scienze Fisiche della Materia
XXIV ciclo

Spin splitting in high-density GaN two-dimensional electron gas

Tesi di dottorato del dott. Davide Spirito

Relatore
Prof. Florestano Evangelisti
Dott.ssa Luciana Di Gaspare

Coordinatore Dottorato
Prof. Settimio Mobilio

a. a. 2010/2011

CONTENTS

INTRODUCTION AND MOTIVATION

The word "spintronics" has become a ubiquitous term to define a new field of study in material science and in electronics. Its use has been spreading in the last decade, as can be seen in figure I. It is "an emerging technology that exploits both the intrinsic spin of the electron and its associated magnetic moment, in addition to its fundamental electronic charge, in solid-state devices" [107]; in a broader sense, it is "a multidisciplinary field whose central theme is the active manipulation of spin degrees of freedom in solid-state systems" [102], with full application of experimental characterisation techniques and theoretical models.

Spintronics promises large enhancements to present day information and communication technologies, to fulfil the requirements of reduction in size and power consumption and enhancement in speed from industries and consumers. Moreover, it gives to scientists the possibility to investigate fascinating physical phenomena.

The starting point of spintronics can be pinpointed with the discovery of giant magnetoresistance in the 1980s. This effect, observed in metallic systems, is now exploited in commercial applications such as hard drives. Other effects in metals (e.g., spin torque) are still being investigated.

Beside metals, semiconductors spintronics has also been tackled. The interest in semiconductors is of course related to the electronic industry: sophisticated spin-based devices which can be implemented in semiconductors can bring new features to electronics [9].

This thesis deals with what lies behind the devices, i. e. materials. In particular, the properties of nitrides semiconductors will be addressed.

Before introducing these materials, let me describe the paradigm of the semiconductor spintronic device, the spin transistor. A number of devices have been proposed (see Ref. [39, chap. V]), but the seminal idea was presented in a 1990 paper by Datta and Das [34]. This paper is often referred to as the motivation of studies related to the spin effects in semiconductors (see figure I); feasibility of their device has been questioned [20], but the working principle was recently demonstrated in a device similar to that of the original proposal [62]. I will use it to introduce the points of interest for this thesis.

The spin field effect transistor they proposed is an "electronic analog of the electro-optic modulator". The spin polarisation plays the role of the photon polarisation: the suggested device has a polariser–analyser pair formed by ferromagnetic contacts, and a two dimensional or one dimensional channel where the spin precedes by defined amount, tuned by an external

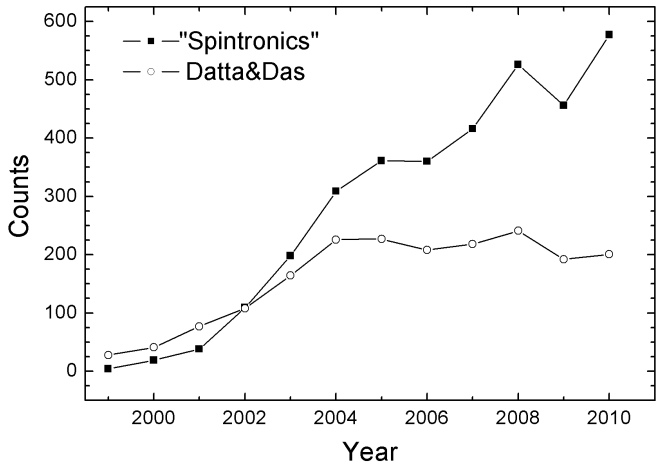

Fig. I: Survey of "spintronics" papers using the on-line database Scopus (`www.scopus.com`). Full symbols: number of papers containing the word *spintronics* or *spintronic* in title, abstract and keywords, since 1999 to 2010; the counts from a query on all records fields (including full text) is about four times larger. Empty symbols: number of citations of the paper by Datta and Das about the spin transistor [34].

electric field. The two ferromagnetic contacts are magnetised in the same direction; if, at the end of the channel, the spin points in the same direction of this magnetisation, the device is in the "on" state; if it is in the opposite direction, the device is "off".

The fabrication of such a device, as proposed by the authors themselves, requires: (1) reliable spin polarising junctions; (2) semiconductor materials where the spin polarisation is not relaxed (so that the electron spin is transported "ballistically"); (3) tuning of the spin-orbit interaction in the channel through the Rashba mechanism, an effect which yields (in principle) the externally controlled spin precession. These features (spin injection, transport, manipulation and detection) are basic requirements for spintronics devices, independently of the particular design.

The actual implementation of these requirements has proved to be difficult. The direct spin injection (or extraction) from ferromagnetic metals into semiconductors is demonstrated to be inefficient because of the so-called "conductivity mismatch problem"; it has been bypassed using composite metal-oxide-semiconductor structures or magnetic semiconductors [39, chap. II].

As for the spin manipulation, spin-orbit interaction is the physical mechanism which may make it possible. The spin-orbit interaction is a well known effect in atomic and solid state physics. However, in the standard atomic picture for solids, the spin degeneracy is not completely removed. In the spin transistor, the required precession needs the two spin states to be non-degenerate. Additional terms to the standard spin-orbit coupling can yield such a degeneracy removal; one of these terms is the Rashba effect. To fulfil the spin manipulation requirement, the effect should be large enough to rotate the spin by π rad within a mean free path; thus, the

spin-splitting energy is often taken as a figure of merit for spintronics materials. This thesis will deal with these additional effects, and in the following of this introduction I will use the expression "spin-orbit interaction" with this special meaning.

Spin-orbit interaction has been investigated in several materials, mainly III-V semiconductors, demonstrating that narrow gap semiconductors and large carrier densities yield large spin splitting [39, chap. III]. Manipulation of its intensity has been demonstrated to be operative with an external electric field [54, 53, 78].

Experimental evaluation of the spin-splitting energy on gallium nitride has given instead conflicting results. This problem has been addressed in this thesis.

Gallium nitride (GaN) and the related alloys (InGaN, AlGaN) have attractive properties for the semiconductor industry, such as a wide bandgap, high mobility, high breakdown field; its use is assessed for high-power, high-frequency devices and in UV optoelectronics. Heterojunctions between GaN alloys yield a two dimensional electron gas (2DEG), and this feature is exploited in high electron mobility transistors (HEMT). The industrial interest has led to a reliable technology for material and device fabrication [27, 81, 87].

Moreover, the 2DEG is interesting for fundamental research as well. Integer and fractional quantum Hall effect [75], quantisation of conductance [25], single electron transistors [26] have been demonstrated on this system.

On the spintronics side, two features have highlighted GaN as a suitable material. Room temperature ferromagnetism has been predicted and measured for dilute magnetic alloys of GaN [70, 86]. This property is useful for the implementation of the spin injector and detector in the spin transistor paradigm. The second feature is related to the possibly large spin-orbit effect in 2DEGs, useful for the spin manipulation.

The interest in nitrides semiconductors for spintronics is shown in figure II. The observed decrease after 2005, different from the general interest on spintronics (see figure I), could be related to the complicated nature of spin-orbit coupling in it.

The issue of spin-orbit coupling in gallium nitride is intriguing both experimentally and theoretically. The most common lattice for gallium nitride is the wurtzite lattice, differently from the more common (in semiconductors) zinc-blende lattice; this lattice is at the origin in several different terms in the spin-orbit coupling. Moreover, despite its large bandgap, large spin-splitting values comparable with those of narrow gap materials have been reported. Nevertheless, also small values have been reported, and a clear dependence on sample parameters has not been determined as yet.

As for the experimental techniques capable of measuring the strength of spin-orbit interaction, the behaviour of the resistivity as a function of a magnetic field has proved to be a suitable method for these investigations. However, a careful data analysis is required to exclude parasitic

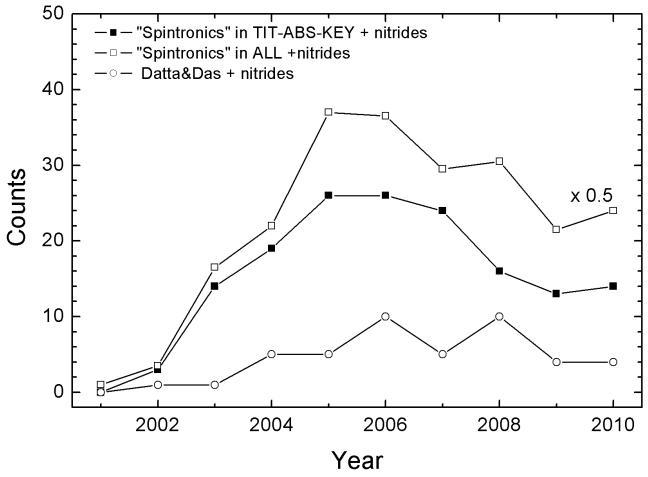

Fig. II: Survey of "spintronics on GaN" papers with the words *GaN*, *AlGaN* or *InGaN* in title, abstract or keywords using the on-line database Scopus. Full squares: number of papers with the words *spintronics* or *spintronic* in title, abstract or keywords; empty squares: number (divided by two) of papers with *spintronics* or *spintronic* in all the fields. Empty circles: number of papers citing the paper by Datta and Das [34].

effects and to achieve a reliable extraction of the parameters.

This work aims at the study of the spin degeneracy removal due to spin-orbit interaction in GaN-based 2DEGs. The effect was investigated performing magnetotransport experiments. The data were analysed in depth to get further information beyond the usual analysis.

The organisation of the thesis mirrors the ideal steps toward the study of spin-orbit interaction in two dimensional electron gases. First, a 2DEG is needed; the properties of this system and its achievement in GaN-based heterostructures are described in chapter 1. Second, the system should have a non-negligible spin-orbit coupling: the mechanisms of this interaction are discussed in chapter 2 (again with regard to GaN), together with a review of literature results. Then, some phenomena affected by spin-orbit interaction needs to be observable: consequently, the magnetotransport phenomena investigated in this thesis, i.e. the Shubnikov–deHaas and the weak antilocalisation, and are described in chapter 3. Finally, the sample and the experimental set-up used, the experiments made, and the methods developed to analyse the data are the subject of chapter 4. In the Appendixes, some further details of the data analysis are reported.

Beside the main topic of this thesis, i.e. the spin-orbit interaction in GaN 2DEGs, other characterisations of this material have been made during this work. In particular, a study of one dimensional devices, such as split gates and quantum point contacts, was used to verify the quality of the material, and was a useful training in the electric measurements techniques; the results of this investigation is presented in appendix E.

In the last period of the thesis work, I have also been involved in an activity aimed at the investigation of spin injection using junctions between ferromagnetic metals and semiconductors, in particular silicon and germanium. However, presently, only preliminary results have been

found, and I have chosen not to include them in this presentation, where I have chosen to focus on magnetotransport experiments on GaN.

The results of the research activity on gallium nitride have been reported in research papers and communications in conferences, as listed below.

Publications:

- **D. Spirito**, L. Di Gaspare, F. Evangelisti, A. Di Gaspare, A. Notargiacomo E. Giovine, "Weak antilocalisation in a two-dimensional electron gas", to be submitted to Physical Review B
- **D. Spirito**, L. Di Gaspare, G. Frucci, F. Evangelisti, A. Di Gaspare, A. Notargiacomo, E. Giovine, S. Roddaro, F. Beltram, "Magnetotransport investigation of conducting channels and spin splitting in high-density AlGaN/AlN/GaN two-dimensional electron gas", Physical Review B, 83, 155318 (2011), doi: 10.1103/PhysRevB.83.155318
- **D. Spirito**, G. Frucci, A. Di Gaspare, L. Di Gaspare, E. Giovine, A. Notargiacomo, S. Roddaro, F. Beltram, F. Evangelisti, "Quantum Transport in Low-Dimensional AlGaN/GaN Systems", Journal of Nanoparticle Research, 13, 5699 (2011), doi: 10.1007/s11051-010-0136-7

Presentations:

- Oral presentation: 35th WOCSDICE (Workshop on Compound Semiconductors Devices and Integrated Circuits), Catania, 29/05/2011-01/06/2011, "Spin properties and ballistic transport in low-dimensional AlGaN/AlN/GaN systems", **D. Spirito**, L. Di Gaspare, G. Frucci, A. Di Gaspare, A. Notargiacomo, E. Giovine, S. Roddaro, F. Beltram, F. Evangelisti
- Poster presentation: X International Conference on Nanostructured Materials, Roma, 13-17/09/2010, "Quantum Transport in Low-Dimensional AlGaN/GaN Systems", **D. Spirito**, G. Frucci, A. Di Gaspare, L. Di Gaspare, E. Giovine, A. Notargiacomo, S. Roddaro, F. Beltram, F. Evangelisti
- Poster presentation: 2nd Transalp' Nano 2010 Conference, Como, 3-5/06/2010, "Quantum Transport in Low -Dimensional AlGaN/GaN Systems", **D. Spirito**, G. Frucci, A. Di Gaspare, L. Di Gaspare, E. Giovine, A. Notargiacomo, S. Roddaro, F. Beltram, F. Evangelisti
- Poster presentation: IEEE Nano 2009, Genoa, 26-30/07/2009, "Conductance Anomalies in Quantum Point Contacts", G. Frucci, A. Di Gaspare, L. Di Gaspare, A. Notargiacomo, E. Giovine, **D. Spirito**, F. Evangelisti

1. TWO DIMENSIONAL ELECTRON GAS IN GAN

1.1 Two dimensional electron gases

Two dimensional electron gases (2DEGs) are fundamental building blocks for semiconductor devices and nanoelectronics.

A 2DEG is the result of an engineered heterostructure, designed to have a band alignment suitable for confining electrons in a potential well and to have free carriers to be collected in the well. The case of gallium nitride based heterostructures — of interest for this thesis work — is treated in section 1.2. In this section, I will briefly review the general features of a two dimensional electron system, in particular the energy spectrum, the density of states and the effect of a magnetic field. Detailed discussions, derivations and reviews on this topic can be found in a number of books and review articles (see, for example, [35, 7, 18]).

The two dimensional system in a semiconductor heterostructure is described on the basis of a three dimensional crystal in the effective mass approximation. The confining potential is taken along the z direction; the electrons are free in the xy plane. In the following, a single electron scheme is also assumed, and the effective mass is assumed to be the same in the different layers of the heterostructure.

With these assumptions, the time-independent Schrödinger equation for this problem reads:

$$\left[-\frac{\hbar^2}{2m}\left(\frac{\partial^2}{\partial x^2}+\frac{\partial^2}{\partial y^2}\right)-\frac{\hbar^2}{2m}\frac{\partial^2}{\partial z^2}+V(z)\right]\psi(x,y,z)=E\,\psi(x,y,z), \tag{1.1}$$

where $V(z)$ is the confining potential. The wavefunction can be separated as

$$\psi(x,y,z)=e^{ik_x x}e^{ik_y y}u_n(z), \tag{1.2}$$

and the energy eigenvalues are given by

$$E_n(k_x,k_y)=\frac{\hbar^2k_x^2}{2m}+\frac{\hbar^2k_y^2}{2m}+\epsilon_n=\frac{\hbar^2\mathbf{k}^2}{2m}+\epsilon_n, \tag{1.3}$$

so that the quantum numbers are k_x, k_y (two-dimensional wavevector components, and $\mathbf{k}$ =

(k_x, k_y)) and n (quantum number of the confinement potential); m is the effective mass suitable for the investigated system.

The eigenfunction $u_n(z)$ and the eigenvalues ϵ_n are the solution of the z-part of the equation:

$$\left[-\frac{\hbar^2}{2m}\frac{\partial^2}{\partial z^2} + V(z)\right] u_n(z) = \epsilon_n u_n(z). \tag{1.4}$$

In this discussion, a discrete spectrum will be assumed. The total energy is thus given by parabolic subbands, whose minima are the ϵ_n values.

The density of states (DOS) per unit area $D(E)$, for one subband and for a system with degeneracy g_s, is constant and equal to $g_s m/2\pi\hbar^2$ when the energy is greater than ϵ_n. The DOS is a step-like function when more subbands are considered.

The electron density per unit area is the integral of the DOS multiplied by the Fermi–Dirac distribution $f(E, E_F)$ (E_F being the Fermi energy):

$$n_{2D} = \int_0^{+\infty} D(E) f(E, E_F) \mathrm{d}E, \tag{1.5}$$

and, in the low temperature limit,

$$n_{2D} = \frac{m}{\pi\hbar^2} \sum_j (E_F - \epsilon_j)\Theta(E_F - \epsilon_j), \tag{1.6}$$

where the sum runs over the subbands with minimum at ϵ_j, and spin degeneracy is assumed ($g_s = 2$).

1.1.1 Landau levels in a magnetic field

Let's consider the effect of a magnetic field parallel to the confinement direction z, and thus perpendicular to the plane containing the 2DEG.

The magnetic field B is included through the vector potential and the minimal substitution in the Schrödinger equation. The vector potential can be chosen in the Landau gauge as $\mathbf{A} = (0, Bx, 0)$, and the hamiltonian becomes

$$H = \frac{\hbar^2}{2m}k_x^2 + \frac{1}{2m}\left(\hbar k_y + eBx\right)^2 + \frac{\hbar^2}{2m}k_z^2 + V(z). \tag{1.7}$$

The separation of z-part yields again the discrete eigenvalues ϵ_n; the xy-part solution is modified by the magnetic field. The Hamiltonian does not depend on y, but has a quadratic term in x; the y-part of the wavefunction is a plane wave $\exp(ik_y y)$, so that the solution is a product of this plane wave and a function $v(x)$. Then, after rearranging the terms, and substituting the y-part

of the wavefunction, we can find that the x-part is a harmonic oscillator Hamiltonian:

$$\left[-\frac{\hbar^2}{2m}\frac{\partial^2}{\partial x^2} + \frac{1}{2}m\omega_c^2\left(x - \frac{\hbar k}{eB}\right)^2\right] v(x) = E\, v(x), \tag{1.8}$$

where the angular frequency

$$\omega_c \equiv \frac{eB}{m} \tag{1.9}$$

is known as cyclotron frequency. The magnetic field acts as a parabolic confinement potential in the x direction. The centre of the cyclotron orbit is k-dependent: $x_k = \hbar k/eB = l_B^2 k$, where the length scale is $l_B = \sqrt{\hbar/eB}$; the energy however is not affected by this parameter. The discrete energies are

$$E_n = \hbar\omega_c\left(n + \frac{1}{2}\right), \quad n = 0, 1, 2\ldots \tag{1.10}$$

These discrete levels are called "Landau levels"; the wavefunction is $v_{nk}(x) \propto H_{n-1}((x - x_k)/l_B)\exp(-(x - x_k)^2/2l_B^2)$, where $H_n(x)$ is the n-th Hermite polynomial.

The effect of the Landau states on the electrical properties of the 2DEG, as well as issues on their lineshape, are described in details in section 3.2.

1.2 GaN-based heterostructures and 2DEGs

Nitride semiconductors can crystallise in the zinc-blende structure and in the wurtzite structure; all the samples investigated in this thesis have the wurtzite structure; its properties will thus be described in details.

The lattice is shown in figure 1.1. This lattice belongs to C_{6v} point group; it can be described as two interpenetrating hexagonal close-packed lattices, an is defined by three parameters: a, c and u. a is the hexagon side, c the height of the prism, and u is an adimensional parameter equal to the ratio of the inter-ion distance $d_\parallel$ in the $[0\,0\,0\,1]$ direction (parallel to the height) and c, $u = d_\parallel/c$; in the ideal structure, $u = 0.375$ and $c/a = 1.633$. Every ion is surrounded by a tetrahedron of ions of different species, as shown in figure 1.1b. The tetrahedra are piled up as in figure 1.1a, and form hexagonal lattice layers alternating anion (N) and cation (Al, Ga, In) layers. As a reference, table 1.1 reports the main parameters for GaN and AlN.

This lattice is non-centrosymmetric, since the layer sequence is reversed along the $[0\,0\,0\,1]$ and $[0\,0\,0\,\bar{1}]$ directions; correspondingly, the surfaces $(0\,0\,0\,1)$ and $(0\,0\,0\,\bar{1})$ have different polarity, and are labelled as *Ga-(Al-)face* and *N-face*.

The crystal grows with a Ga- or N-face depending on the details of the growth process [4, 6].

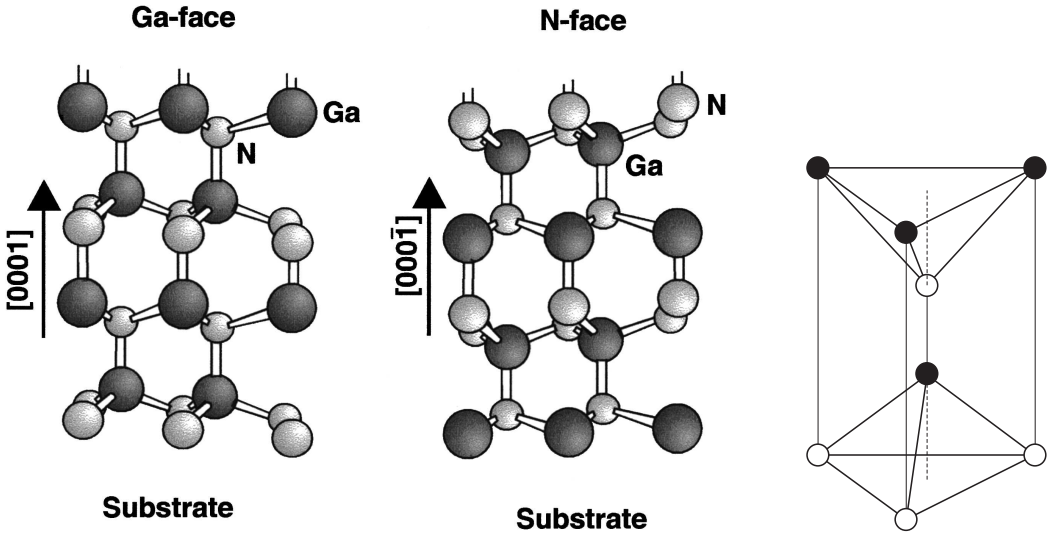

Fig. 1.1: (a) Wurtzite crystal lattice for GaN, in the two different polarity: Ga-face and N-face; (b) alignment of tetrahedra.

	GaN	AlN
a (Å)	3.189	3.112
c (Å)	5.185	4.982
u	0.376	0.380
$E_G(eV)$	3.42	6.13
m (m_e)	0.22	0.22
ε_r	10.4	10.1

Tab. 1.1: Lattice parameters (a, c, u), energy gap E_G, effective mass m (in units of the electron mass), relative dielectric constant ε_r of gallium nitride and aluminium nitride (from Ref. [6] and references therein).

1.2.1 Two dimensional gas formation

In wurtzite nitride heterostructures, grown in the [0 0 0 1] direction (or *c*-direction), a 2DEG can originate because of the internal electric polarisation only, without intentional doping [5]. This polarisation is the sum of spontaneous polarisation P_{SP}, due to the ionic bonds, and of piezoelectric polarisation P_{PE}, due to layers deformation.

The spontaneous polarisation depends on structural parameters; the polarisation vector always points toward the N-face. This sense of the vector is defined as negative, thus P_{SP} is always negative. For Ga-face heterostructures it points toward the substrate, while for N-face it points toward the surface.

Piezoelectric polarisation depends on the strain of the heterostructure layers. For GaN/AlGaN heterostructures there are three cases (sketched in figure 1.2): (i) relaxed AlGaN on relaxed GaN, without piezoelectric polarisation; (ii) tensile-strained AlGaN on relaxed GaN; (iii) compressive-strained GaN on relaxed AlGaN.

Piezoelectric polarisation is calculated from piezoelectric coefficients e_{ij} as:

$$P_{PE} = e_{33}\epsilon_z + e_{31}(\epsilon_x + \epsilon_y), \tag{1.11}$$

where $\epsilon_z = (c - c_0)/c_0$ is the strain in the growth direction and $\epsilon_x = \epsilon_y = (a - a_0)/a_0$ is the strain in the plane; these values are related by

$$\epsilon_z = -2\frac{C_{13}}{C_{33}}\epsilon_x, \tag{1.12}$$

where C_{13} and C_{33} are the elastic coefficients. Inserting this formula in (1.11), we get

$$P_{PE} = 2\frac{a - a_0}{a_0}\left(e_{31} - e_{33}\frac{C_{13}}{C_{33}}\right). \tag{1.13}$$

Since the quantity in brackets is negative both for $Al_xGa_{1-x}N$ (independent of Al content x) and GaN, piezoelectric polarisation is negative for a tensile strain and positive for a compressive strain (case (iii), GaN on AlGaN).

Since the spontaneous polarisation is negative, the two polarisations are parallel for tensile strain and antiparallel for compressive strain. If the surface polarity changes, both polarisations change their sign. Figure 1.2 describes the polarisation configurations in the case of an AlGaN/GaN structure [5]. In the case of more complex structures, analogous considerations can be made.

In general, the total polarisation is different in a AlGaN layer and in a GaN layer; following the electrostatic relation $\nabla \cdot \mathbf{P} = \rho_{pol}$, which relates an induced charge density to a non-zero polarisation divergence, when a polarisation discontinuity is present at an interface there is an

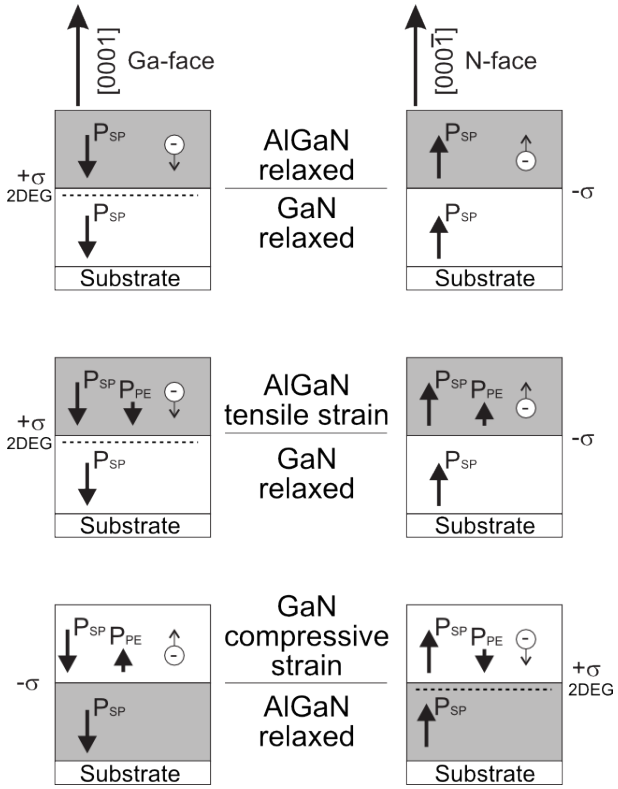

Fig. 1.2: Polarisation charge induced in a AlGaN/GaN heterostructure, in different cases of strain and polarity. The formation of a 2DEG is marked. (Adapted from Ref. [5]).

induced sheet charge.

The induced charge density is thus given by:

$$\sigma = P^u - P^l = (P^u_{SP} - P^l_{SP}) - (P^u_{PE} - P^l_{PE}), \tag{1.14}$$

where superscripts u e l refer to the upper and lower layer, respectively.

When the induced charge is positive, electrons accumulate and a two dimensional electron gas forms; when the induced charge is negative, a two dimensional hole gas can form. The induced charge sign depends both on the absolute value of polarisations in the two layers and on their alignment (parallel or antiparallel); these properties depend on the heterostructure polarity, on the aluminium content in the AlGaN layer and on the pseudomorphic or relaxed growth of this layer [6]. These parameters thus determine the gas formation and its density; the conditions when a 2DEG can form are marked in figure 1.2.

In a pseudomorphic AlGaN on GaN heterostructure, charge density is given by

$$|\sigma(x)| = |P_{PE}(\mathrm{Al_xGa_{1-x}N}) + P_{SP}(\mathrm{Al_xGa_{1-x}N}) - P_{SP}(\mathrm{GaN})|. \tag{1.15}$$

In Ga-face heterostructures the sign is positive, and an electron gas forms. Thus, the total

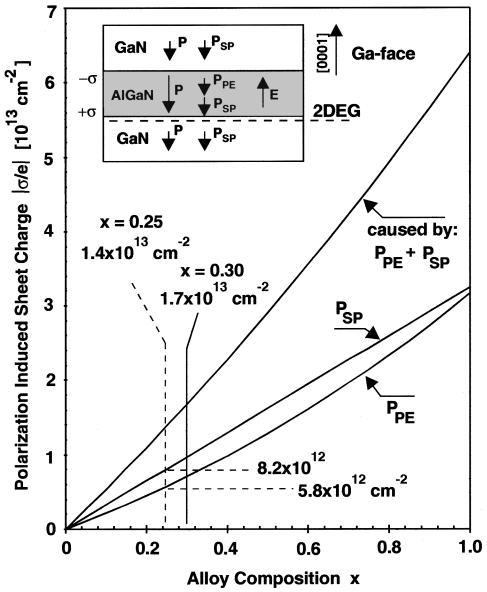

Fig. 1.3: Charge density due to spontaneous and piezoelectric polarisation, as a function of AlGaN composition (from Ref. [5]).

polarisation in the AlGaN layer as a function of aluminium content x is

$$|\sigma(x)| = \left|2\frac{a(0)-a(x)}{a(x)}\left(e_{31}(x) - e_{33}(x)\frac{C_{13}(x)}{C_{33}(x)}\right) + P_{SP}(x) - P_{SP}(0)\right|, \tag{1.16}$$

where the dependence of the different parameters on x can be approximated by a linear interpolation of GaN and AlN parameters.

Figure 1.3 shows the charge density as a function of x, calculated for a AlGaN/GaN heterostructure in the [0 0 0 1] direction.

The sheet carrier density at the interface can be calculated with the polarisation charge density in equation (1.16) and with an electrostatic analysis [111]:

$$n_{2D}(x) = +\frac{\sigma(x)}{e} - \left(\frac{\varepsilon_0\varepsilon(x)}{de^2}\right)\Big[e\phi_b(x) + E_F(x) - \Delta E_C(x)\Big] \tag{1.17}$$

where d is the AlGaN layer thickness, ε the permittivity, E_F the Fermi energy (with respect to the GaN conduction band edge at the interface), and ΔE_C is the conduction band discontinuity; $e\phi_b$ represents the barrier at surface, due to the pinning of the Fermi level because of surface states, or to the formation of a Schottky junction with a gate electrode, if present.

AlGaN parameters $\varepsilon(x)$ and $e\phi_b(x)$ can be approximated, as function of x, by linear interpolation of GaN and AlN parameters.

The conduction band discontinuity is given by

$$\Delta E_C = 0.7\Big[E_g(x) - E_g(0)\Big], \tag{1.18}$$

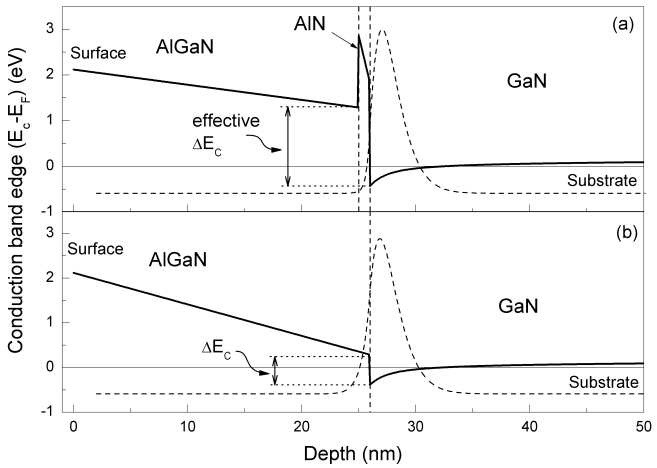

Fig. 1.4: Sketch of the conduction band edge for (a) AlGaN/AlN/GaN heterostructure, with exclusion layer, (b) AlGaN/GaN heterostructure. Wavefunctions are drawn as dashed lines. The conduction band discontinuity ΔE_c and the effective conduction band discontinuity are also marked. (Adapted from Ref. [90]).

where E_g is the bandgap, given by [17]:

$$\begin{aligned} E_g(x) &= xE_g(\mathrm{AlN}) + (1-x)E_g(\mathrm{GaN}) - x(1-x)1.0\ \mathrm{eV} \\ &= x\,6.13\ \mathrm{eV} + (1-x)\,3.42\ \mathrm{eV} - x(1-x)1.0\ \mathrm{eV}. \end{aligned} \tag{1.19}$$

The Fermi level is calculated as

$$E_F(x) = E_0(x) + \frac{\hbar^2\pi}{m} n_{2D}(x), \tag{1.20}$$

where E_0 is the energy level in the potential well; the effective mass m is assumed to be independent on x.

1.2.2 Heterostructures with exclusion layer

An improvement in charge density and mobility can be attained in AlGaN/GaN heterostructures by inserting a thin AlN layer between the other two layers, the so-called exclusion layer [90, 92].

Figure 1.4 shows a comparison of AlGaN/GaN and AlGaN/AlN/GaN structures with a sketch of the conduction band edge and of the wavefunction of the first quantum well energy state.

Since AlN bandgap is 6.13 eV, it creates at the interface a barrier, which increases the electron confinement; moreover, also the effective conduction band discontinuity (defined as the difference between band edge in AlGaN and in GaN at the respective interfaces with AlN, see also figure 1.4a) is increased, because of the AlN polarisation-induced electric dipole [90, 60], as shown in figure 1.4.

These effects allow to have a large carrier density. Moreover, the thin AlN layer reduces the alloy scattering, that is the scattering mechanism due to disordered distribution of aluminium and gallium in the lattice sites of AlGaN: since penetration of wavefunction in the AlGaN layer is reduced because of the barrier, this mechanism is less effective. Mobility is thus largely improved in this kind of heterostructure: for example, in Ref. [10] is reported (at 77 K) an increase in the mobility from 2991 $cm^2V^{-1}s^{-1}$ (in a sample without exclusion layer) to 8080 $cm^2V^{-1}s^{-1}$ in sample similar to the first, but with the exclusion layer. Since the mobility is found to be a decreasing function of the carrier density [5, 40], the exclusion layer allows to have a large mobility at the largest densities.

2. SPIN-ORBIT INTERACTION IN GAN-BASED HETEROSTRUCTURES

2.1 Spin-orbit interaction in solids and heterostructures

Spin-orbit interaction (SOI) is an effect related to the motion of an electron in an electric field. In the rest frame of the electron, the electric field is seen as a magnetic field, which acts on the magnetic dipole of the electron (due to the spin). This effective magnetic field for a particle moving with velocity $\mathbf{v}$ in a field $\mathbf{E}$ is given, in SI units, by

$$\mathbf{B} = -\left(\frac{\mathbf{v}}{c^2} \times \mathbf{E}\right), \tag{2.1}$$

c being the speed of light.

The SOI Hamiltonian for a given electric potential $V(\mathbf{x})$ can be calculated classically as $H = -\boldsymbol{\mu} \cdot \mathbf{B}$; this is correct in its form, but a relativistic theory is required to have the correct proportionality constant.The Dirac equation in the non-relativistic limit [51, chap. 5] yields

$$H_{SO} = \frac{e\hbar}{4m^2c^2}\mathbf{p} \cdot (\boldsymbol{\sigma} \times \boldsymbol{\nabla} V(\mathbf{x})), \tag{2.2}$$

where m is the electron mass, and $\boldsymbol{\sigma}$ is the Pauli matrices vector.

In the atomic case, i.e. in a central potential, we can rewrite $\boldsymbol{\nabla} V(\mathbf{x}) = (dV/dr)(\mathbf{r}/r)$, and, rearranging the triple product, find $H_{SO} \propto (\mathbf{r} \times \mathbf{p}) \cdot \boldsymbol{\sigma} = \mathbf{L} \cdot \mathbf{S}$, ($\mathbf{L}$, $\mathbf{S}$ being the orbital angular momentum and the spin); this Hamiltonian is usually treated using the total angular momentum $\mathbf{J}$. In solids, the description of spin-orbit interaction is complicated by the details of the crystal lattice. Qualitatively, if the electronic states are represented in an atomic orbitals picture, one can say that the p-like ($L = 1$) bands are affected by the spin-orbit, while the s-like ($L = 0$) are not. This "atomic" part of the SOI is usually taken into account in band structure calculations, and is found to affect mainly the valence band.

Valence bands of semiconductors are (at the zone centre) p-like states. The 3-fold degeneracy is removed by SOI, and the $j = 3/2$ and $j = 1/2$ states are split. A simple model to describe this band structure is the 4-band Kane model (for an introduction see Ref. [35, chap X]). Within this model, atomic-like states are utilised as basis functions. The SOI effect on s-like conduc-

tion band is only in the value of the effective mass. In analogy with the atomic case, the SOI affects the "orbital motion" of electrons, but retains the J_z degeneracy.

Extended models and more sophisticated band structure calculations can give a better estimation of this effect [109]; in the case of GaN, a removal of spin degeneracy in the conduction band is also found, as discussed below.

To remove the spin degeneracy, an inversion-asymmetric potential is required [109, chap. 6]. Such a potential can be related to asymmetry in the bulk lattice (referred as BIA, bulk inversion asymmetry), or, in the case of a quantum well, to the confinement potential (SIA, structural inversion asymmetry). These terms can be included in band structure calculations.

The subject of the thesis is indeed this degeneracy removal as effect of the spin-orbit interaction.

Finally, note that the degeneracy removal is described in terms of an effective magnetic field, which leads to an energy splitting as in the Zeeman effect; often, also the vector $\mathbf{\Omega}$ is defined to describe the spin precession in this effective field (after rewriting the Hamiltonian as $H_{SO} = \hbar\boldsymbol{\sigma} \cdot \mathbf{\Omega}$).

2.2 Spin-orbit interaction in wurtzite semiconductors

The spin-orbit interaction in semiconductors with the wurtzite structure, such as GaN and AlN, and in 2DEGs hosted in them, is a somewhat puzzling topic. On the theoretical side, the involved mechanisms are different and more subtle than those acting in the more common (and more widely investigated, both theoretically and experimentally) zinc-blende semiconductors (see Ref. [39, chap. III] for a review of SOI in zinc-blende). On the experimental side, the measured spin-splitting energy has been found to differ markedly, from 0 (i.e., non detectable) to 13 meV, without a clear correlation of the energy values with the sample parameters.

In this section, a summary of the theoretical studies of SOI in wurtzite is reported, with a particular attention to the case of 2DEGs. The experimental results are summarised in section 2.4.

As mentioned above, the terms leading to spin splitting in conduction band can be classified as BIA or SIA, according to their origin; the latter is usually called "Rashba effect" or "Byckhov-Rashba effect", while the former is called "Dresselhaus term". Before describing the physical mechanisms behind SOI in details, I will briefly mention the angular dependence of the vector $\mathbf{\Omega}$, and remark the differences between wurtzite and zinc-blende. A comparison of the different terms is shown in table 2.1. The Rashba term is the same in the two lattices; in wurtzite, Rashba and Dresselhaus have the same angular dependence, while in zinc-blende Rashba and Dresselhaus have different angular dependence.

In the case of a 2DEG in the xy-plane, only the x and y components are retained, and the k_z is

	Wurtzite	Zinc-blende
Rashba	$\alpha_R(k_y, -k_x, 0)$	$\alpha_R(k_y, -k_x, 0)$
Dresselhaus	$\gamma(bk_z^2 - k_\parallel^2)(k_y, -k_x, 0)$	$\gamma\left(k_x(k_y^2 - k_z^2), k_y(k_z^2 - k_x^2), k_z(k_x^2 - k_y^2)\right)$

Tab. 2.1: Comparison of the vector $\hbar\mathbf{\Omega}$ in the case of bulk wurtzite and zinc-blende for the different SOI terms [42, 78].

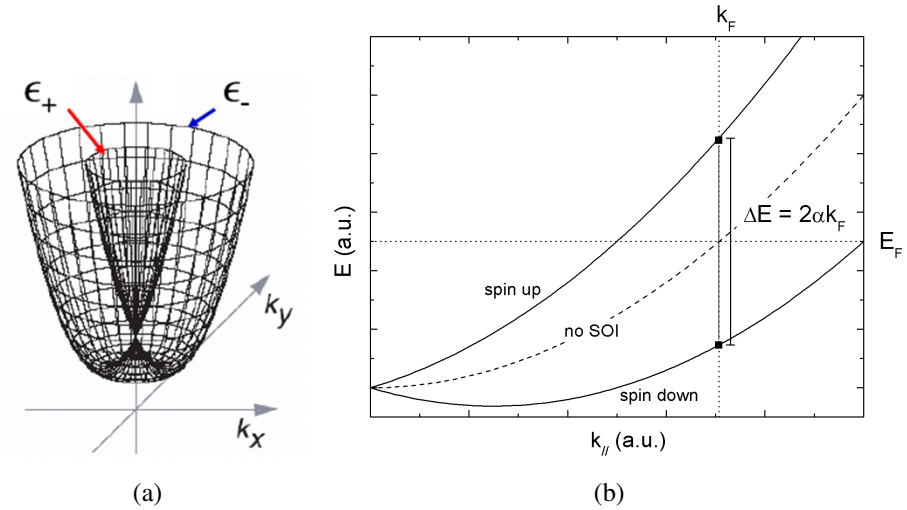

(a) (b)

Fig. 2.1: Energy spectrum for a 2DEG with Rashba spin-orbit interaction. Panel (b) reports the dependence on the $\mathbf{k}$ in the radial direction, and a comparison with the energy spectrum without the interaction. The construction of the energy splitting, as described in section 2.4, is also shown.

replaced by its average value in the quantum well. If we introduce the expressions $k_x = k_\parallel \cos\theta$ and $k_y = k_\parallel \sin\theta$, for the case of wurtzite it is found that

$$\mathbf{\Omega} \propto k_\parallel(\sin\theta, -\cos\theta), \tag{2.3}$$

with $k_\parallel = (k_x^2 + k_y^2)^{1/2}$. This angular dependence shows that the Rashba interaction is isotropic. Figure 2.1 shows the energy dispersion of a 2DEG with a spin-orbit interaction of the Rashba type. The original parabolic band splits in two concentric bands for the two spin projection; the Fermi surface in the k_xk_y plane, which is a single, spin-degenerate circumference without SOI, becomes two concentric circumferences.

In the case of a 2DEG, for the zinc-blende the Rashba term has the angular dependence of equation (2.3), while the Dresselhaus term can be rewritten, with the help of trigonometric identities, as

$$\begin{aligned}\mathbf{\Omega} =&\gamma k_z^2(-k_x, k_y) + \gamma(k_x k_y^2, -k_y k_x^2) = \\ =&\gamma k_z^2 k_\parallel(-\cos\theta, \sin\theta) + \gamma\frac{k_\parallel^3}{4}(\cos\theta - \cos 3\theta, -\sin\theta - \sin 3\theta) = \\ =&\gamma\left(k_z^2 - \frac{k_\parallel^2}{4}\right)k_\parallel(-\cos\theta, \sin\theta) + \gamma\frac{k_\parallel^3}{4}(-\cos 3\theta, -\sin 3\theta);\end{aligned} \tag{2.4}$$

the first term is usually referred as linear Dresselhaus term, the second being the cubic Dresselhaus (or Dresselhaus *tout court*) term. The SOI in zinc-blende is thus anisotropic, and this feature has been observed experimentally [78, 46]. This does not occur in wurtzite.

Byckhov-Rashba effect This effect, in its original formulation [19], originates from the presence of an electric field which creates an asymmetric potential for the electrons. In a heterostructure, the electric field is the internal built-in field, as well as any external field, in particular the one due to a bias on a gate electrode. The magnitude of this effect depends on the material. In the case of nitride semiconductors, the electric fields due to spontaneous and piezoelectric polarisation are relevant as well.

For an electron in the xy plane, the Hamiltonian is

$$H_{BR} = \alpha_{BR}(\boldsymbol{\sigma} \times \mathbf{k}) \cdot \hat{\mathbf{z}} = \alpha_{BR}(\sigma_x k_y - \sigma_y k_x). \tag{2.5}$$

The coefficient α_{BR} depends both on the details of the heterostructure (width and shape of the well, composition of the barriers) and on the band structure of the underlying materials. For wurtzite semiconductors it can be calculated according to the theory developed by Litvinov in Refs. [68, 69]. This theory obtains the coefficient in the framework of a $\mathbf{k}\cdot\mathbf{p}$ 8×8 band structure calculation. It takes into account external electric fields, electric fields in the heterostructure (including polarisation fields), strain, crystal field and spin-orbit interaction in the valence band. The coefficient α_{BR} can be written as

$$\alpha_{BR} = P_1 P_2 \left|\left\langle \frac{d\beta(z)}{dz} \right\rangle\right|, \tag{2.6}$$

where $P_{1,2}$ are the momentum matrix elements. In a heterostructure, the function $\beta(z)$ is the sum of terms describing the Rashba effect for the different layers. It depends on the band structure and the material parameters, and on the external fields. The triangle brackets represent the average over the ground state of the quantum well ($\langle f \rangle \equiv \int \Phi^* f \Phi \, \mathrm{d}z$, Φ being the ground state envelope function).

As an example, we can consider the case of a quantum well W with two barriers L and R

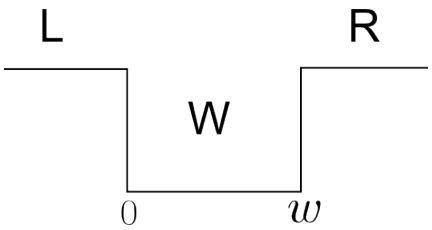

Fig. 2.2: Sketch of the quantum well considered in equation (2.7).

(see figure 2.2). In the chosen reference frame, the well extends from 0 to w. In this case

$$\left\langle \frac{d\beta(z)}{dz} \right\rangle = \Phi^2(0)(\beta_W - \beta_L) + \Phi^2(w)(\beta_R - \beta_W) + e\langle B_L F_L \rangle + e\langle B_W F_W \rangle + e\langle B_R F_R \rangle. \tag{2.7}$$

In this equation, the triangle brackets represent the average over the corresponding region. The coefficients B_i and β_i are involved functions of the band structure and material parameters of the i-th layer; the exact formulae can be found in Ref. [68]. F_i is the electric field in the layer.

This formulation highlights that the Rashba coefficient is determined mainly by the electric field inside the quantum well; this field is determined by the charge density in the well. However, the charge is a function of the barriers composition, especially in the case of polarisation doped heterostructures (see figure 1.3); in particular, the electric field increases with x [47], and, from equation (2.7), the Rashba parameter is expected to increase accordingly. Moreover, the contribution of the barriers is proportional to the penetration of the wavefunction in them.

In Ref. [68] the spin-splitting energy of a 2DEG hosted in an AlGaN/GaN heterostructure is calculated, comprising both the effect of doping and polarisation. The splitting is found to be strongly dependent on x, but does not exceed 1 meV (figure 2.3). However, in actual samples (as those reviewed in section 2.4) the Al content and the density do not exceed 0.35 and $1.2{\cdot}10^{17}$ m^{-2}, respectively. From the calculated carrier density it is possible to recover the Rashba parameter α_{BR}. It depends on x with an approximately linear relation; it is also found that α_{BR} depends approximately linearly on the carrier density too ($\alpha_{BR} = gn$), with a coefficient $g \approx 0.57 \cdot 10^{-30}$eV m^3. This linear relation is indeed expected since α is proportional to the electric field in the channel, which is proportional to the carrier density.

Dresselhaus effect in bulk wurtzite and WSIA The bulk inversion asymmetry (BIA) of lattices such as wurtzite and zinc-blende contributes to the spin splitting with an additional term. In zinc-blende this yields, for electrons in conduction band, a term proportional to k^3 (see also table 2.1), namely the Dresselhaus effect.

In wurtzite, Lew van Voon *et al.* [66] found, in addition to the Dresselhaus cubic term, a linear term called *wurtzite structural inversion asymmetry* (WSIA) or Rashba effect in bulk wurtzite. These terms have been investigated in band structure calculation using the $\mathbf{k} \cdot \mathbf{p}$ approximation and the tight binding method.

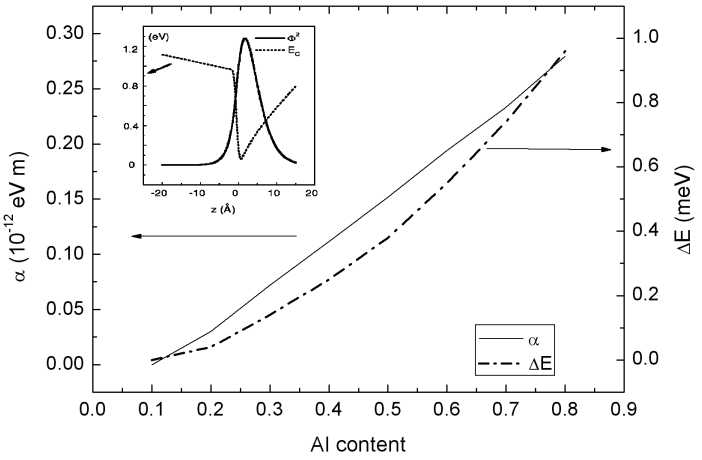

Fig. 2.3: Calculation of Rashba parameter α and spin-splitting energy ΔE as a function of the aluminium content x in the barrier in a $Al_xGa_{1-x}N$/GaN heterostructure. The barrier is 10-nm-thick with doping concentration of 10^{18} cm^{-2}. Inset shows the shape of the quantum well considered in this calculation. Adapted from Ref. [68].

In particular, in Ref. [42] an 8×8 Kane model is constructed, and the two terms are retrieved. The chosen basis functions are given by linear combination of four band edge states with s-like and p-like symmetry, taken with spin-up and spin-down. The Dresselhaus term is

$$H_D = \gamma_{wz}(bk_z^2 - k_{\|}^2)(\sigma_x k_y - \sigma_y k_x). \tag{2.8}$$

The linear WSIA term can be written as

$$H_{WSIA} = \alpha_{WSIA}(\sigma_x k_y - \sigma_y k_x). \tag{2.9}$$

To calculate the parameters b, γ_{wz} and α_{WSIA}, the linear combination of atomic orbital (LCAO) method has been applied. In the case of ideal wurtzite lattice, in a first-neighbours LCAO approximation, only the Dresselhaus term is found. Second-neighbours interaction of cations and anions leads to an s-p_z mixing in the conduction band, which yields the WSIA. Deviations from the ideal structure (caused by crystal field and strain) also lead to a WSIA-like term [103]. The model in Ref. [42] includes these effects as well. From calculations in Refs. [42, 104], the values of the parameters are found to be $b \approx 4$, γ_{wz}=0.32 ·10^{-30} eV m^3 and α_{WSIA}=0.9·10^{-12} eVm.

Conduction bands coupling When the band structure of a wurtzite material is calculated from that of a zinc-blende material, a band folding effect arises, as remarked by Lo *et al.* [72]. They calculated the band structure with the LCAO method for gallium nitride, shown in figure 2.4.

From a single zinc-blende band, two wurtzite bands ($C1$ and $C3$) are generated; along the ΓA

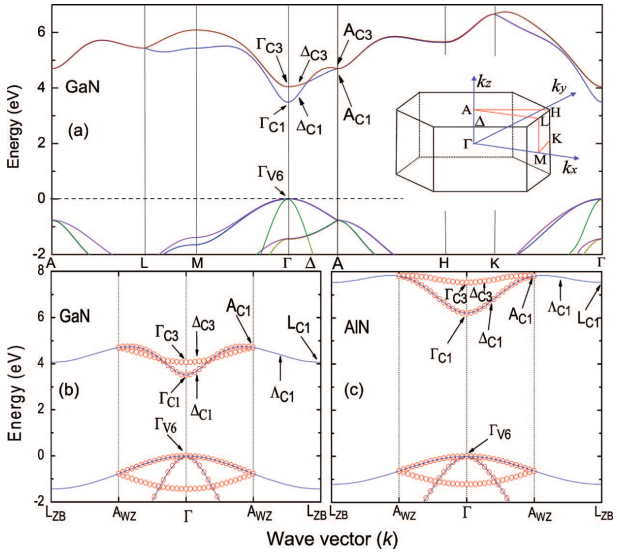

Fig. 2.4: Band structure of gallium nitride with wurtzite lattice (from Ref. [72]). (a) Band structure in the first Brillouin, along the directions shown in the inset (b) Detail of the zone centre (c) Detail of the aluminium nitride bands.

direction (i.e., along the k_z direction in the first Brillouin zone), they are labelled Δ_{C1} and Δ_{C3}; Δ_{C1} is an s-like state, while Δ_{C3} has a large p-component. These calculations show that these two bands are separated at $\mathbf{k} = 0$. In GaN, the bands are actually coupled, and an anticrossing appears at a point along the ΓA direction with $k_{\|} \neq 0$. Because of this coupling, the p-like component is enhanced in the lowest conduction band; this is shown in figure 2.5b. This hybrid configuration enhances the spin-orbit interaction in the lowest conduction band, and causes spin-splitting in it, as shown in the figure 2.5c. It is found that the spin-splitting is a function of k_z. In particular, as shown in figure 2.5a there is a discontinuity at the value of k_z corresponding to the anticrossing point: before this point, the energy splitting is increasing and smaller than 2 meV; at the discontinuity the energy splitting jumps to 6 meV, but then it has a decreasing trend. According to Ref. [73], this effect is taken into account in the Hamiltonian with a coefficient γ_{band} which sums to the γ_{wz} coefficient.

In the case of a quantum well, the $\Delta_{C1} - \Delta_{C3}$ coupling is enhanced by the presence of the electric field, and is inversely proportional to the well width; in Ref. [72] a spin splitting energy between 2 and 5 meV is calculated for a AlN/GaN quantum well.

2.2.1 Total spin-orbit interaction and spin splitting in 2DEGs

In summary, the spin-orbit Hamiltonian for a 2DEG in a wurtzite lattice can be written as a sum of the different terms described in the previous section [103]:

$$H_{SO} = \left[\alpha_{BR} + \alpha_{WSIA} - (\gamma_{wz} + \gamma_{bands})\left(b\langle k_z^2\rangle - k_{\|}^2\right)\right](\sigma_x k_y - \sigma_y k_x), \tag{2.10}$$

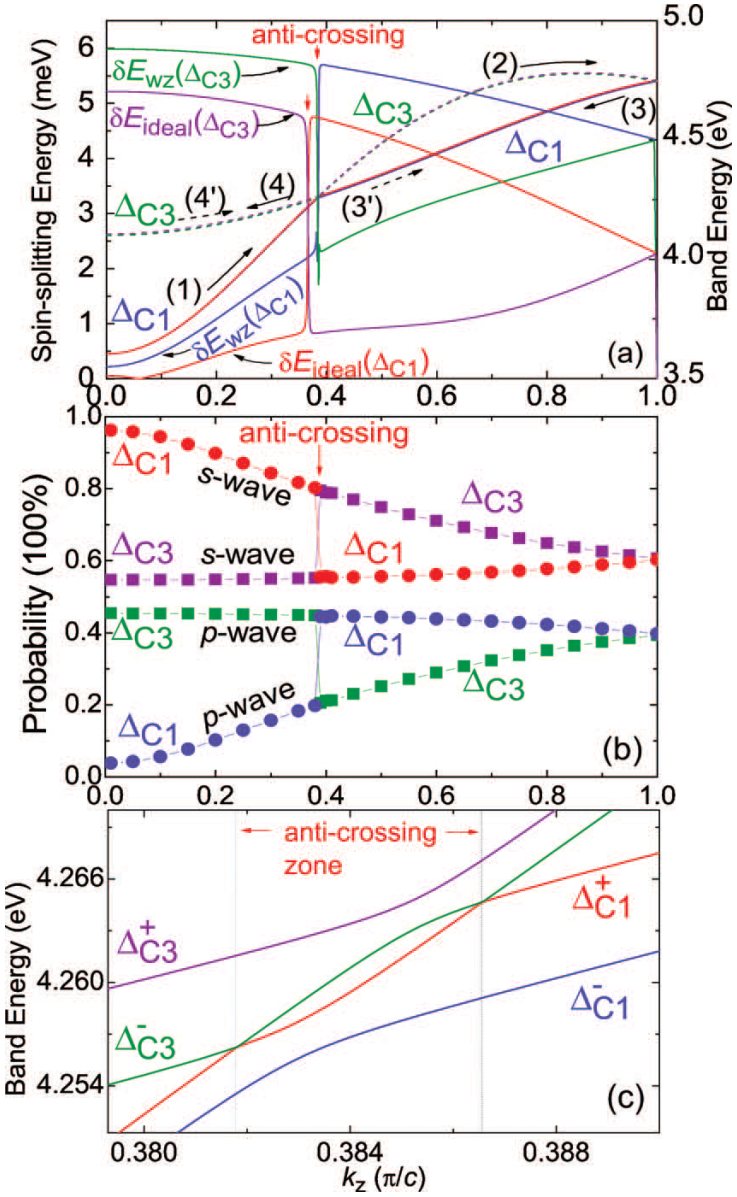

Fig. 2.5: (a) Energy dispersion and spin-splitting for the Δ_{C1} and Δ_{C3} bands as a function of the wavevector k_z (along the ΓA direction). The labels "ideal" and "wz" refer to a calculation with or without the WSIA effect, respectively. (b) Probabilities of *s*- and *p*-components for the Δ_{C1} and Δ_{C3} bands. (c) Details of the band structure near the anticrossing point. From Ref. [72].

where α_{BR} describes the effect of the electric field, both external (if tuned with a gate electrode) and internal, α_{WSIA} the WSIA effect, the coefficient γ_{wz} describes the Dresselhaus term and γ_{bands} the $\Delta_{C1} - \Delta_{C3}$ coupling. $\langle k_z^2 \rangle$ is the mean square of the momentum in the direction z, calculated for the ground state of the quantum well. The interaction depends on the quantum well shape and on the 2DEG density (through $k_\parallel$ and $\langle k_z^2 \rangle$, because of the electric field due to the 2DEG).

The total energy splitting is

$$\Delta E = 2\left[\alpha_{BR} + \alpha_{WSIA} - (\gamma_{wz} + \gamma_{bands})\left(b\langle k_z^2\rangle - k_\parallel^2\right)\right]k_\parallel. \tag{2.11}$$

The parameters α_{WSIA}, γ_{wz}, γ_{bands} and b can be estimated from band structure calculation, as reported above; moreover, calculations for a specific heterostructure should be considered, as described in Ref. [72].

As for the Rashba parameter α_{BR}, its dependence can be calculated for every heterostructure using the theory developed by Litvinov and reported above.

The value of $\langle k_z^2 \rangle$ should be evaluated by solving the coupled Schrödinger and Poisson equation for the quantum well. It is given by $\int |\partial\Phi/\partial z|^2 \mathrm{d}z$, Φ being the wavefunction.

When all the terms are taken into account, the energy splitting dependence on $k_\parallel$ can be more complex than those sketched in figure 2.1. If either the linear or the cubic term dominates, the energy splitting will be monotone; in this case, ΔE is zero only at $k_\parallel$=0. In intermediate configurations, the spin splitting can be zero at finite $k_\parallel$; this condition is found when

$$\alpha_{BR} + \alpha_{WSIA} - (\gamma_{wz} + \gamma_{bands})\left(b\langle k_z^2\rangle - k_\parallel^2\right) = 0. \tag{2.12}$$

In this case, the Fermi surfaces of the two non-spin-degenerate subbands are two distinct circles in the $k_x k_y$ plane.

In magnetotransport measurements, to be discussed in the following, the energy split is measured at the Fermi wavevector k_F. Indeed, when different samples are compared, the parameter assumed to control the spin splitting is the carrier density n, or $k_F = \sqrt{2\pi n}$. In the estimation of ΔE as a function of n (or k_F), it is necessary to take into account the dependence of α_{BR} and $\langle k_z^2 \rangle$ on n itself. Moreover, discontinuities may appear, since the spin splitting due to the conduction band coupling is discontinuous as a function of k_z (see figure 2.5a).

However, since the entity of different contributions to SOI can differ from sample to sample, a comparison of a group of samples as a whole to the theoretical estimations reported above may only be approximate, and a simple parametrisation of the experimental data could be hard.

2.3 Observable effects of spin-orbit interaction

Different effects bearing traces of the spin-orbit interaction have been experimentally investigated in semiconductor heterostructures (for a review see Ref. [112]): resonant Raman scattering, where a split peak in intrasubband excitation reveals the SOI [58]; photogalvanic effect experiments, where a peculiar dependence of the photocurrent on the incidence angle of the light is the SOI signature [44]; and magnetotransport experiments, which is the subject of this work. In nitrides semiconductors, in particular, circular photogalvanic effect [106] and magnetotransport have been exploited.

The presence of SOI can be observed in the magnetoconductance through two different effects and in two different magnetic field regimes: the weak antilocalisation effect (WAL) at low field, and a double frequency component in Shubnikov–deHaas (SdH) oscillations at high field. SOI affects these two kinds of measurement in two very different ways.

WAL is an effect of interference between the 2DEG electrons scattered by impurities (details in sections 3.3); the SOI can affect it in two ways. First, it can lead to a relaxation of spin, i.e. the spin is randomly changed during the electron trajectory, changing the interference amplitude. This relaxation occurs through the so-called D'yakonov-Perel' mechanisms [39, chap. IV]: the electron feels the SOI effective field, which depends on the momentum; upon scattering, the effective field changes randomly with the momentum; this random effective field relaxes the spin. As for the second way, SOI affects WAL acting as a spin-dependent vector potential. In particular, this effect is relevant when the impurity scattering is very small, as in high mobility 2DEGs, where the SOI can rotate the spin without randomising it. The WAL experiment reveals the change in the relative orientation of interfering electrons, and allows extracting the SOI parameters.

SdH effect (described in details in section 3.2) manifests itself as oscillations of the magnetoresistivity whose frequency spectrum is sensitive to carrier density and to the presence of parallel conductive channels in the sample. The effect of SOI is to split the conduction band (as shown in figure 2.1); the two spin channels will have slightly different carrier density, and thus they will be revealed by a SdH measurements as two frequency oscillations (beatings pattern). The energy splitting between the two spin levels, referred as zero-field spin splitting (to distinguish from Zeeman splitting), or simply spin splitting, is then directly measured.

The observation of the double frequency in Shubnikov–deHaas effect imposes strict requirements on the electron mobility and the carrier density. The mobility damps the oscillations at low field, and thus it is required to be high enough in order to see the effect at reasonably low fields. As for the carrier density, at low carrier density the frequency can be too low to allow an observation of a sufficient number of oscillations and detect the two frequencies behaviour.

2.4 Literature review

Table 2.2 is a summary of the magnetotransport experiments reported in the literature on spin-orbit interaction in AlGaN/GaN heterostructures. In figures 2.6, 2.7, 2.8 I show the values reported in the literature for the energy splitting and the Rashba parameter as a function of the carrier density and mobility. Note that the mobility values are not reported for all samples.

The strength of the spin-orbit interaction is usually reported as spin-splitting energy ΔE or as the Rashba coefficient α; note that α an effective parameter, since, as described previously, ΔE depends on several mechanisms; the two quantities are related by $\Delta E = 2\alpha k_F$, taking k_F as the Fermi vector in the absence of spin-orbit interaction (see figure 2.1).

Small splitting is usually reported from WAL measurements, whereas SdH gives larger values; only Zhou *et al.* [115] reported a value smaller than 2 meV from SdH, and verified it in WAL measurements. Thillosen *et al.* [98] found a small splitting in WAL measurements and beatings in SdH, which would yield a larger splitting value; however, they attributed the SdH beatings to inhomogeneities in the sample (these values are marked in table 2.2 with a question mark).

Note also that in two cases reported in the table the value of the spin splitting could not be measured, in the limit of the employed experimental technique; that is, in the case of SdH, no beatings or no double frequency in the Fourier transform can be resolved, and, in the case of WAL, only weak localisation observed. In this case the symbol "n.d." (not detected) is used in the table.

The spin splitting is usually reported as a function of carried density, and referred to be proportional to n [67]; nevertheless, small values have been reported at the highest carrier density. Olshanetsky *et al.* [82] could not measure the splitting at the highest carrier density reported for this kind of studies.

To combine the information about carrier density, mobility and energy splitting, figure 2.9 reports the density and the mobility on the x and y axes, respectively, while the different marker types depend on the splitting ΔE. The energy values are arbitrarily classified as "small" ($\Delta E <$ 2 meV), "medium" ($2 < \Delta E < 5$ meV), and "large" ($\Delta E > 5$ meV). In figure 2.6 the three groups are separated by dotted lines.

We note that some authors [89, 64, 98, 101] changed the carrier density in the sample through a gate bias; for two of them [89, 64], the results are reported in the table. However, the Rashba parameter is found to be constant in the investigated density range. Lo *et al.* [73] reported the control of the density via persistent photoconductivity effect; while they could control the density in a narrow range, the energy splitting was varied from zero (in the dark) to about 10 meV.

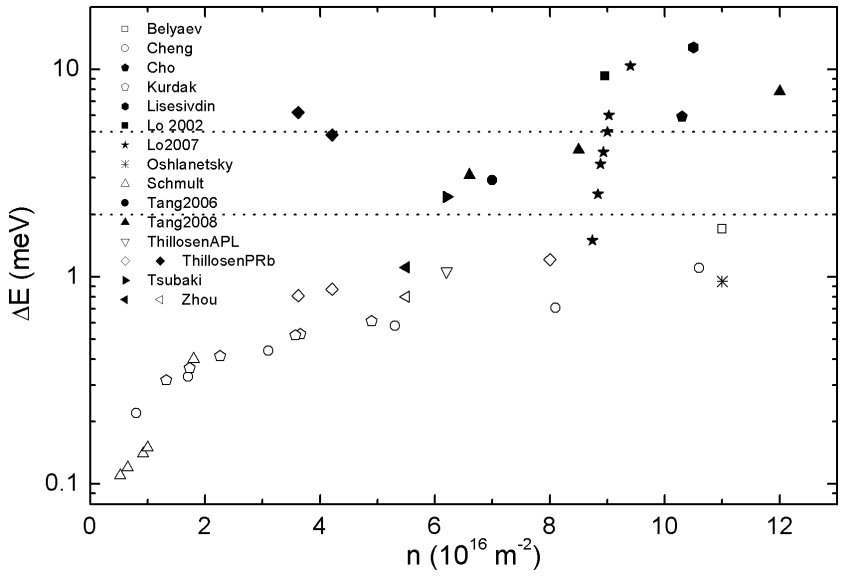

Fig. 2.6: Energy splitting as a function of carrier density for samples in table 2.2. Empty symbols mark WAL measurements, solid symbols SdH measurements; different symbols refer to different references: see table 2.2. Horizontal lines separate three groups of samples according to their splitting energy as described in the text.

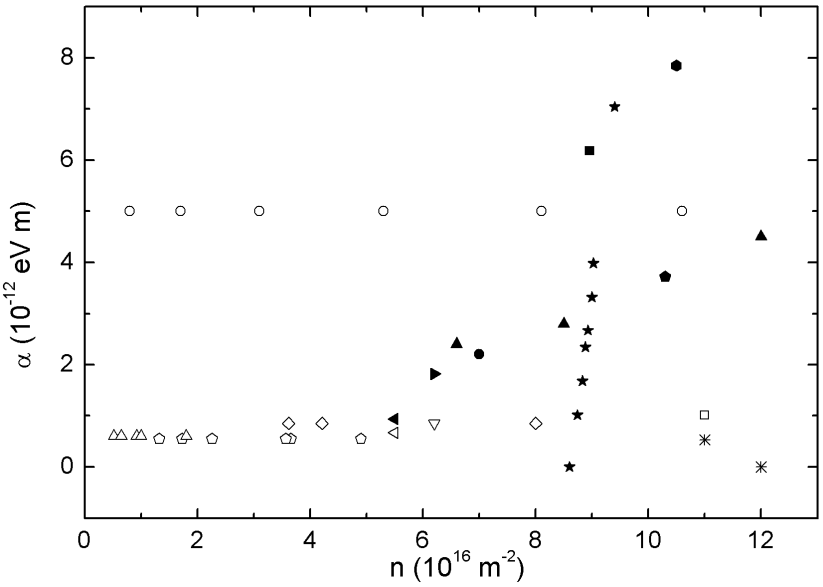

Fig. 2.7: Rashba coefficient as a function of carrier density for samples in table 2.2. Legend: see figure 2.6.

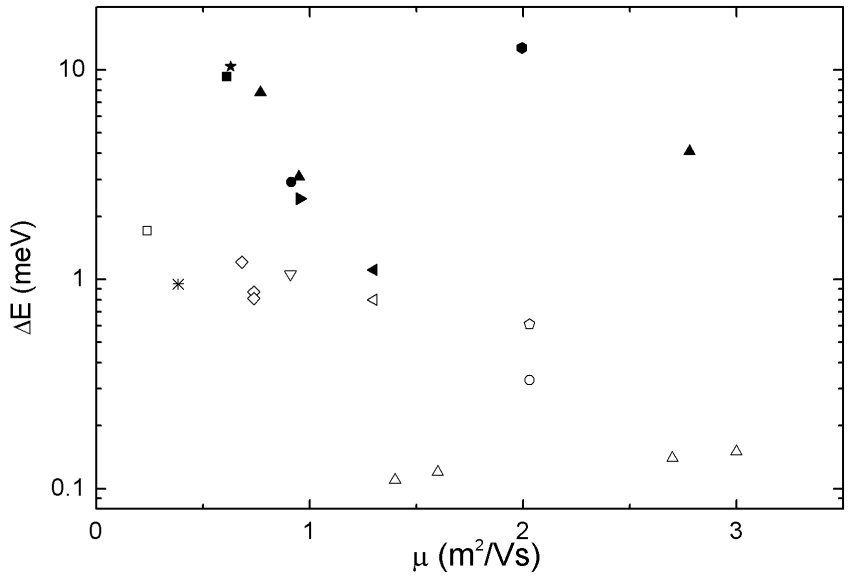

Fig. 2.8: Energy splitting as a function of electron mobility for samples in table 2.2. Legend: see figure 2.6.

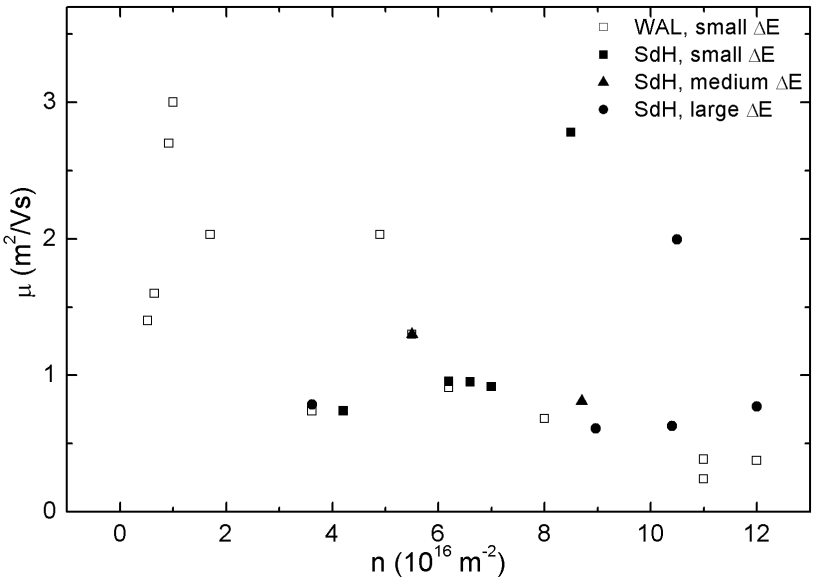

Fig. 2.9: Mobility as a function of carrier density for samples in table 2.2. Symbols are defined by measurement type and energy splitting.

Ref/sample	T K	Doping Si 10^{18}cm^{-3}	d_{AlGaN} (x) nm	d_{AlN} nm	n 10^{16}m^{-2}	μ m^{2}V^{-1}s^{-1}	method	α 10^{-12}eV m	ΔE meV
Belyaev[13]	0.3	0	23(0.33)	0	11	0.24	WALb	1.01	1.7
Cheng[22]A	1.8	0	25(0.1)	1	0.8		WALd	5	0.22
Cheng[22]B	1.8	0	25(0.15)	1	1.7	2.03	WALd	5	0.33
Cheng[22]C	1.8	0	25(0.25)	1	3.1		WALd	5	0.44
Cheng[22]D	1.8	0	25(0.3)	1	5.3		WALd	5	0.58
Cheng[22]E	1.8	0	25(0.35)	1	8.1		WALd	5	0.71
Cheng[22]F	1.8	0	25(0.35)	1	10.6		WALd	5	1.1
Cho[24]D	0.3	3	30(0.31)	0	10.30		SdHf	3.72	5.91
Kurdak[64]A	1.6	0	25(0.1)	1	1.32		WALd	0.55	0.32
Kurdak[64]B	1.6	0	25(0.15)	1	4.9	2.03	WALd	0.55	0.61
Kurdak[64]B	1.6	0	25(0.15)	1	1.73		WALd	0.55	0.36
Kurdak[64]B	1.6	0	25(0.15)	1	2.26		WALd	0.55	0.41
Kurdak[64]B	1.6	0	25(0.15)	1	3.57		WALd	0.55	0.52
Kurdak[64]C	1.6	0	25(0.25)	1	3.66		WALd	0.55	0.53
Lisesivdin[67]	2	0	25(0.22)	1.5	10.5	1.99	SdHf	7.85	12.75
Lo2002[71]3	1.2	0.17	30(0.25)	0	8.96	0.61	SdHf	6.18	9.27
Lo2007[73]dark	0.38	0	25(0.22)	0	8.6	0.81	SdHf	n.d.	n.d.
Lo2007[73]light	0.38	0	25(0.22)	0	8.7		SdHf	1.0	1.5
Lo2007[73]light	0.38	0	25(0.22)	0	8.83		SdHf	1.7	2.5
Lo2007[73]light	0.38	0	25(0.22)	0	8.88		SdHf	2.3	3.5
Lo2007[73]light	0.38	0	25(0.22)	0	8.93		SdHf	2.7	4.0
Lo2007[73]light	0.38	0	25(0.22)	0	9.0		SdHf	3.3	5
Lo2007[73]light	0.38	0	25(0.22)	0	9.02		SdHf	4.0	6

Ref/sample	T	Doping Si	$d_{AlGaN}(x)$	d_{AlN}	n	μ	method	α	$2\alpha k$
Lo2007[73]light	0.38	0	25(0.22)	0	9.4	0.63	SdHf	7.04	10.38
Olshanetsky[82]07	0.3	0	30(–)	0	11	0.38	WALd	0.53	0.95
Olshanetsky[82]03	0.3	0	100(0.3)	0	12	0.37	WALd	n.d.	n.d.
Schmult[89]B	0.3	0	16(0.12?)	0	0.52	1.4	WALd	0.6	0.11
Schmult[89]B	0.3	0	16(0.12?)	0	0.65	1.6	WALd	0.6	0.12
Schmult[89]B	0.3	0	16(0.12?)	0	0.92	2.7	WALd	0.6	0.14
Schmult[89]B	0.3	0	16(0.12?)	0	1.0	3.0	WALd	0.6	0.15
Tang2006[96]	2	0	30(0.11)	0	7	0.92	SdHf	2.2	2.92
Tang2008[97]A	2	0	30(0.11)	0	6.6	0.95	SdHf	2.4	3.09
Tang2008[97]B	2	0	28(0.25)	0	8.5	2.78	SdHf	2.8	4.09
Tang2008[97]C	2	0	25(0.28)	0	12	0.77	SdHf	4.5	7.81
ThillosenAPL[99]	0.1	0	20(0.3)	0	6.2	0.91	WALd	0.85	1.06
ThillosenPRb[98]1	1	0	35(0.15)	0	4.21	0.74	WALd	0.85	0.87
ThillosenPRb[98]2	1	0	35(0.15)	0	3.62	0.74	WALd	0.85	0.81
ThillosenPRb[98]3	1	0	30(0.3)	0	8	0.68	WALd	0.85	1.21
ThillosenPRb[98]1	1	0	35(0.15)	0	4.21	0.74	SdHf	4.7?	4.8?
ThillosenPRb[98]2	1	0	70(0.15)	0	3.62	0.78	SdHf	6.5?	6.2?
Tsubaki[101]	0.4	5	27(0.15)	0	6.2	0.95	SdHf	1.82	2.43
Zhou[115]	1.5	0	23(0.11)	0	5.5	1.3	WALb	0.67	0.81
Zhou[115]	1.5	0	23(0.11)	0	5.5	1.3	SdHn	0.94	1.11

Tab. 2.2: Survey of literature on spin-splitting in AlGaN/GaN 2DEGs. Sample parameters are reported; in the column "method", "WALd" refers to analysis of weak antilocalisation data within a diffusive model, "WALb" within a ballistic model; "SdHf" refers to Shubnikov–deHaas effect investigated through the FFT, "SdHn" through beating node position (see sections 3.3 and 3.2.1 for details). When a value is not present, it was not reported in the respective paper. The symbol "n.d." in the ΔE and α columns stands for *not detected*.

3. MAGNETOTRANSPORT IN 2DEGS

The main part of this work involves the investigation of transport in 2DEGs in presence of a magnetic field, to measure the spin-orbit interaction in these systems. In this chapter, the theory of the investigated phenomena is reported.

First, the classical magnetotransport, described by the Drude model, will be presented: this is the standard tool for the basic characterisation of a material. Then, the Shubnikov–deHaas effect will be described: this effect allows both to investigate the standard properties of a 2DEG and to determine the spin-splitting energy. Finally, the weak localisation phenomenon will be presented: it probes the interference properties of electron waves, and can be strongly affected by the spin-orbit interaction, yielding a distinctive pattern called "antilocalisation".

3.1 Classical magnetotransport

The properties of charge carriers in materials are usually investigated through the analysis of the magnetoresistance. Fundamental characteristics such as carrier density and mobility in bulk semiconductors and 2DEGs can be determined from the combined measurements of Hall effect voltage and resistivity, at fixed magnetic field or as a function of the magnetic field magnitude, in the framework of the classical Drude model for conductivity [52, chap. XV]. In particular, this kind of measurements are important for the study of systems where more than one carriers type or conductive channels are present.

We will consider a two dimensional system in the xy plane; the current can flow along x, and the electric field can be along x and y; the magnetic field will be along z. This geometry is that of the standard "Hall bar", sketched in figure 3.1. The x direction is referred as longitudinal direction, and y is the transverse direction.

When a magnetic field B is applied, the Hall effect gives rise to an electric field perpendicular to the current and to the magnetic field. Then, the resistivity (or conductivity) scalar must be replaced by a 2×2 tensor. The transverse component of the resistivity is $\rho_{xy} = R_{xy} = V_{xy}/I$.

In the following, we will consider the case of a single type of carriers, with a single a scattering time τ_1 (and thus a single mobility $\mu_1 = e\tau_1/m_1$), and a carrier density per unit area n_1; such a system is a single channel system. Then, the multiple channels system (or multicarrier system) will be considered. In all the cases, the system will be considered isotropic, so that

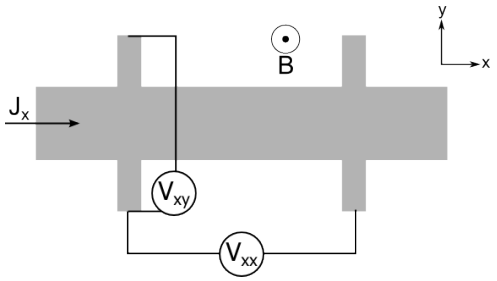

Fig. 3.1: Hall bar geometry.

effective masses are scalars. The scattering times are assumed to be constant (independent of energy) or to have a narrow distribution in energy (so that the average value can be taken); this hypothesis is well suited for 2DEGs and degenerate systems.

The Hall effect will be derived using the Drude phenomenological approach, suitable for the above hypotheses; a more rigorous treatment would require, in a semiclassical framework, the solution of the Boltzmann equation.

In the Drude approach, the electron with charge $-e$ moves classically in an electric field $\mathbf{E}$ and in a magnetic field $\mathbf{B}$, in a dissipative medium described by the scattering time τ. The equation of motion is

$$m\dot{\mathbf{v}} = -e\mathbf{E} - e\mathbf{v} \times \mathbf{B} - \frac{m}{\tau}\mathbf{v}. \tag{3.1}$$

The system is investigated in the steady state, hence $\dot{\mathbf{v}} = 0$. Arranging the above equation, and inserting the current density as $\mathbf{J} = -en\mathbf{v}$ and the mobility as $\mu = e\tau/m$, the equation can be written as

$$\begin{cases} J_x = & \dfrac{en\mu}{1+(\mu B)^2}\left(E_x - \mu B E_y\right) \\ J_y = & \dfrac{en\mu}{1+(\mu B)^2}\left(\mu B E_x + E_y\right), \end{cases} \tag{3.2}$$

and the conductivity components are

$$\sigma_{xx} = \sigma_{yy} = \frac{en\mu}{1+(\mu B)^2}, \tag{3.3a}$$

$$\sigma_{xy} = -\sigma_{yx} = -\frac{en\mu^2 B}{1+(\mu B)^2}. \tag{3.3b}$$

The resistivity is recovered inverting the conductivity tensor:

$$\rho_{xx} = \frac{\sigma_{xx}}{\sigma_{xx}^2 + \sigma_{xy}^2}, \qquad \rho_{xy} = \frac{\sigma_{xy}}{\sigma_{xx}^2 + \sigma_{xy}^2}. \tag{3.4}$$

The longitudinal resistivity is then $\rho_{xx} = 1/en\mu$, independent of B, and the transverse is a linear function of B: $\rho_{xy} = B/en$. Figure 3.2 shows an example of longitudinal and transverse

conductivity and resistivity for a channel with $n = 1 \cdot 10^{17}$ m^{-2} and $\mu = 5$ m^2/Vs.

The above two relations allow to determine n and μ with a single measurement of ρ_{xx} and ρ_{xy} at a fixed finite field.

When two or more conductive channels are present, the experimental determination of the parameters is not straightforward. Assuming that the channels feel the same electric fields (i.e., they are parallel channels), the total conductivity tensor is given by the sum of tensors whose components are analogous to those in equation (3.3). For an N-channel system they are given by

$$\sigma_{xx} = e \sum_{j=1}^{N} \frac{n_j \mu_j}{1 + (\mu_j B)^2}, \tag{3.5a}$$

$$\sigma_{xy} = eB \sum_{j=1}^{N} \frac{s_j n_j \mu_j^2}{1 + (\mu_j B)^2}. \tag{3.5b}$$

where the carrier density n_j and μ_j are the j-th carrier density and mobility, e is the (positive) electron charge, and s_j is -1 for electrons and +1 for holes; the mobility is always positive. Note that this convention is not standard; the elementary charge can be taken with a definite sign for each channel, then giving the mobility a sign (positive for holes, negative for electrons); in the following, a convention where both n_j and μ_j have sign will be applied: in this case, the symbol s_j is dropped. The resistivity is found using equations (3.4).

The presence of multiple channels affects the conductivity and the resistivity markedly; in particular, the longitudinal resistivity is not a constant as a function of the magnetic field. An example for the case of two channels is shown in figure 3.2; the two channels parameters are $n_1 = -1 \cdot 10^{17}$ m^{-2}, $\mu_1 = -5$ m^2/Vs and $n_2 = -0.8 \cdot 10^{17}$ m^{-2}, $\mu_2 = -0.8$ m^2/Vs.

Finally, it is worth noting that the parameter which distinguishes two channels is the mobility; indeed, since equations (3.5) are linear in n_j, two channels with $\mu_1 = \mu_2$ and $n_1 \neq n_2$ will contribute as a single channel with total density $n_1 + n_2$.

Although this behaviour of the resistivity components as a function of B can be a qualitative indication of a multicarrier system, when there are more than one conductive channels a quantitative extraction of the transport parameters (n_j and μ_j) from the data is difficult because of the large number of parameters. The procedure can be eased by the "reduced conductivity tensor" (RCT) formalism [61]. In this approach a normalisation of the data reduces the numbers of fit parameters by 1, assuming the zero-field longitudinal conductivity as a known parameter. This value is given by

$$\sigma_{xx}(B = 0) = \sigma_0 = e \sum_{j=1}^{N} n_j \mu_j \tag{3.6}$$

Note that the transverse conductivity is always zero at zero field.

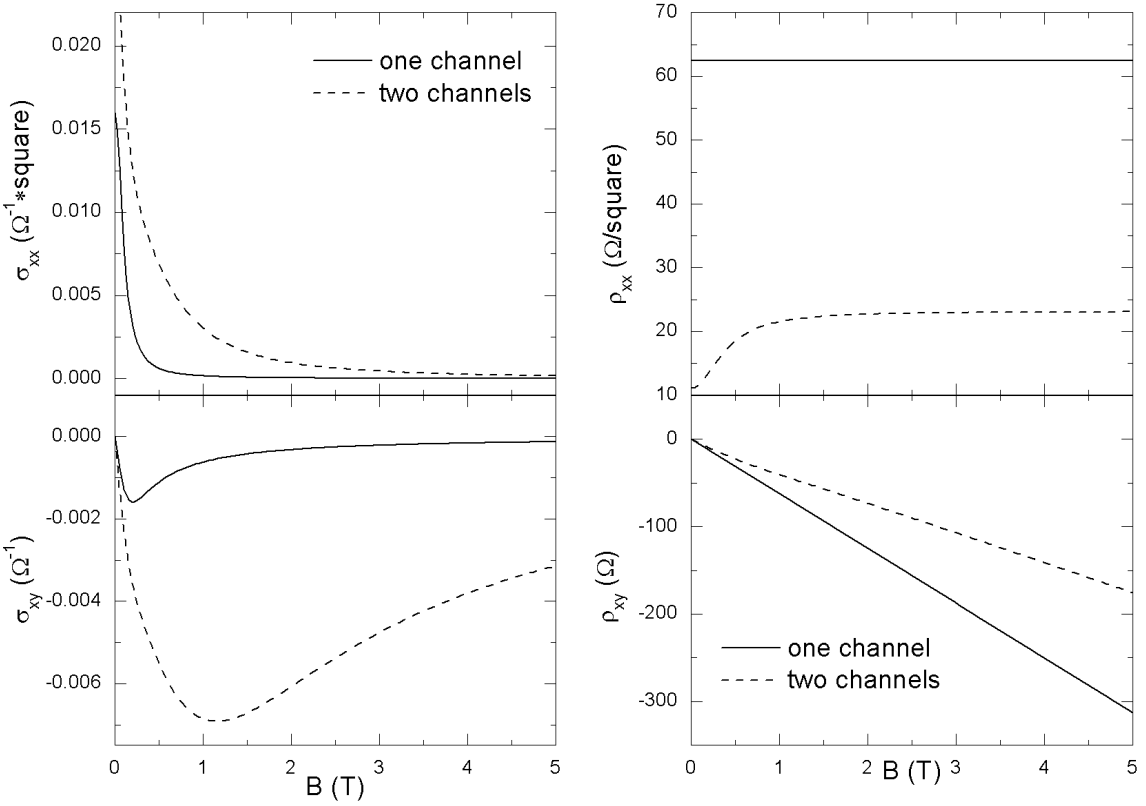

(a) (b)

Fig. 3.2: Calculated (a) conductivity and (b) resistivity for the cases of one and two channels, with $n_1 = -1 \cdot 10^{17}$ m^{-2}, $\mu_1 = -5$ m^2/Vs and $n_2 = -0.8 \cdot 10^{17}$ m^{-2}, $\mu_2 = -0.8$ m^2/Vs.

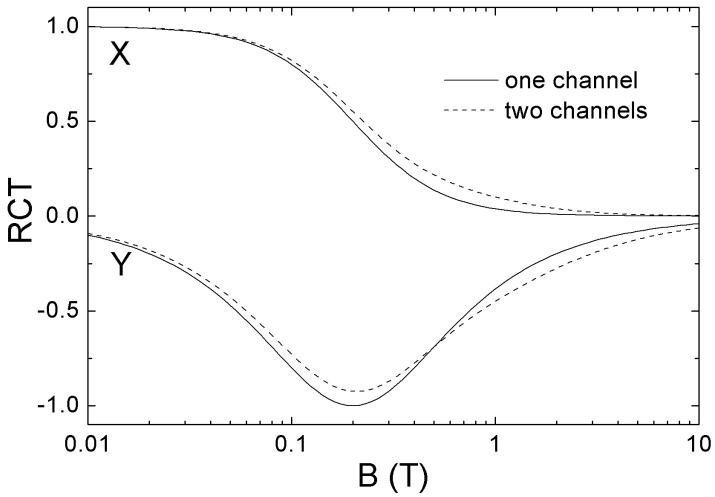

Fig. 3.3: Calculated RCT X and Y components for the cases of one and two channels, with $n_1 = -1 \cdot 10^{17}$ m^{-2}, $\mu_1 = -5$ m^2/Vs ($f_1 = 0.89$) and $n_2 = -0.8 \cdot 10^{17}$ m^{-2}, $\mu_2 = -0.8$ m^2/Vs ($f_2 = 0.11$).

This formalism was developed in the hypothesis of the van der Pauw geometry. However, a measurement in a Hall bar device allows the measurements of the two components ρ_{xx} and ρ_{xy}, from which the resistivity tensor can be reconstructed, and inverted to get the conductivity and apply the RCT formalism.

The reduced components are:

$$X = \frac{\sigma_{xx}}{\sigma_0} = \sum_{j=1}^{N} \frac{f_j}{1 + (\mu_j B)^2}, \tag{3.7a}$$

$$Y = 2\frac{\sigma_{xy}}{\sigma_0} = 2B \sum_{j=1}^{N} \frac{f_j \mu_j}{1 + (\mu_j B)^2}. \tag{3.7b}$$

The conductivity channels are defined by their mobility μ_j; the parameters f_j are the conductivity fractions due to each channel, and are given by

$$f_j = \frac{e n_j \mu_j}{\sigma_0} \tag{3.8}$$

The f_js satisfy the relations $0 \leq f_j \leq 1$ and $\sum f_j = 1$.

In figure 3.3 the RCT components are reported for the one channel and two channels systems already shown in figure 3.2.

This formulation gives a criterion to verify if only one channel is present. In this case, the Y component has a maximum value (or a minimum value, according to the sign of the carriers) of -1, and this maximum is found at $B = \mu^{-1}$. Moreover, at this field value, the X component has the value of 0.5.

The fitting procedure requires the minimisation of a χ^2 function defined as

$$\chi^2(\boldsymbol{\mu}, \mathbf{f}) = \frac{1}{2(L+1)} \sum_{n=0}^{L} \left[\Big(X(B_n; \boldsymbol{\mu}, \mathbf{f}) - X_n \Big)^2 + \Big(Y(B_n; \boldsymbol{\mu}, \mathbf{f}) - Y_n \Big)^2 \right], \tag{3.9}$$

where X_n, Y_n, B_n are the L experimental values of the RCT components and of the magnetic field, respectively.

From the fitting procedure the values of f_j and μ_j are retrieved. The carrier density n_j is found from

$$n_j = \frac{f_j}{\mu_j} \frac{\sigma_0}{e}. \tag{3.10}$$

In Ref. [61] this analysis is estimated to be reliable for channels with $f > 0.01$.

3.2 Shubnikov–deHaas effect

The Drude conductivity requires corrections to include quantum effects. In a magnetotransport experiment, two prominent effects should be considered: Shubnikov–deHaas effect and weak localisation or antilocalisation; the latter dominates at very low fields, while the former can be observed at higher fields.

Both these corrections are calculated in the linear response theory, using the Kubo formula [74, chap. 3][36]. This formula allows the calculation of the response function (the conductivity in the case of electronic transport experiments) through the calculation of a retarded two-particle correlation function of current operators; for this reason it is called current-current of four-current[1] correlation function. It can be calculated using Green functions and diagrammatic expansions techniques.

Both these effects bear signatures of the spin splitting in the conduction band. The weak antilocalisation itself is a consequence of the spin-orbit interaction; it will be discussed in section 3.3.

The Shubnikov–deHaas (SdH) effect gives oscillations in the longitudinal resistivity (or conductivity) as a function of magnetic field, both in 3D and in 2D samples. The effect involves conducting electrons (or holes) which move in a plane perpendicular to the applied field. Then, a 2DEG offers a simpler system for the study of such effect, and its experimental investigation is easier than in 3D system; indeed, the SdH effect is a standard test to verify the actual presence of a 2DEG in a heterostructure.

The distinctive pattern of the presence of spin-orbit interaction are beatings in these oscillations. However, other phenomena may lead to similar beatings, so that the SdH measurements require a careful analysis to correctly evaluate the spin splitting in the investigated system.

[1] The four-current is defined, in the four dimensional relativistic notation, as $J^\mu = (c\varrho, \mathbf{j})$, where ϱ is the charge density and $\mathbf{j}$ the current density

The main feature, i.e. the oscillatory behaviour, of SdH effect is described in this section. Other details will be discussed in connection to the experimental results in section 4.2.3.

3.2.1 Main features of the Shubnikov–deHaas effect

The SdH oscillations are periodic and damped in the inverse magnetic field. Figure 3.4 shows examples of experimental magnetoresistivity curves. In this figure different features of the SdH effect can be observed: oscillatory behaviour, damping, temperature effect, effect of spin splitting.

The oscillatory behaviour results from the emptying of the Landau levels as a function of an increasing magnetic field. The energy of the n-th Landau level is given by (see section 1.1.1)

$$E_n(B) = \hbar\omega_c\left(n+\frac{1}{2}\right) = \frac{\hbar e}{m}B\left(n+\frac{1}{2}\right), \quad n = 0, 1, \ldots, \quad \Delta E(B) = \frac{\hbar e}{m}B, \tag{3.11}$$

It is important to determine the filling condition of Landau levels, in particular, the number of filled levels, and if the last level is completely filled or not, to determine the transport properties. The filling factor ν (also called filling index, or Landau index) is given by the ratio between the number of electrons in the system and the number of states in each Landau level. The Landau levels degeneracy is a function of the magnetic field; indeed, the density of states of the 2DEG at zero field rearranges in a series of discrete levels, whose spacing increases with increasing magnetic field. Using the densities per unit area, the filling factor is $\nu = n_{2D}/n_B$, where n_{2D} is the 2D carrier density and n_B is the degeneracy of the Landau level per unit area; its value can be calculated from the DOS of the 2DEG at zero field $D_0 = g_s m/(2\pi\hbar^2)$ (where $g_s = 2$ counts the two spin states in the same Landau level):

$$n_B = D_0\Delta E(B) = g_s\frac{e}{h}B, \tag{3.12}$$

so that the filling factor is

$$\nu = \frac{n_{2D}}{n_B} = \frac{h}{e}\frac{n_{2D}}{g_s}\frac{1}{B}. \tag{3.13}$$

If the total number of electrons is fixed, the Fermi energy is pinned to the highest occupied Landau level while the magnetic field varies. In figure 3.5a the position of the Fermi energy is marked as a function of magnetic field. The Fermi energy switches from one level to the other at critical values of the field, which correspond to integer values of the filling factor.

This is explained in figure 3.5b, which sketches the density of states as a function of energy; note that in the figure the Landau levels have a finite width, to ease the understanding of the picture, while in this discussion the DOS is assumed to be a series of delta function. When the number of filled Landau levels is an integer n, the Fermi level E_F lies between the n- and $n+1$-level, and the DOS at E_F is then 0. When E_F lies inside a level, the DOS will be different

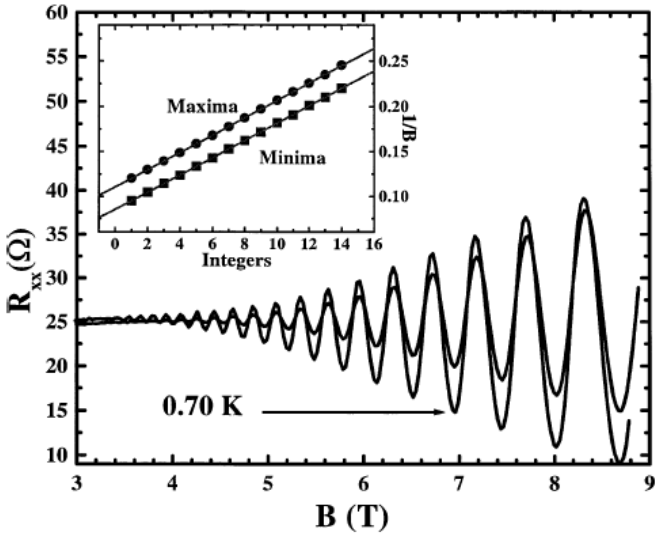

(a)

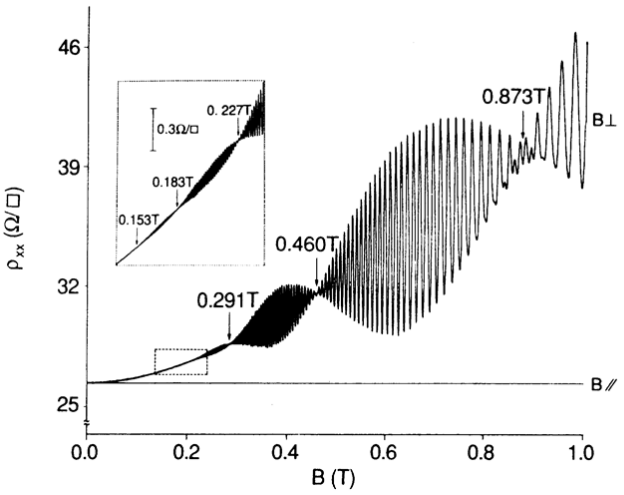

(b)

Fig. 3.4: Examples of Shubnikov–deHaas oscillations in (a) GaN 2DEG [2] and (b) InGaAs 2DEG [32]. Note the different magnetic field scale, due to the different mobility of the two samples. In (a), two measurements at different temperature (0.70 K and 5.0 K) are shown; the inset reports the position of the extrema of the oscillations. In (b), beating nodes are visible, related to a two-spin-subbands occupancy; a curve (marked with $B_{||}$) taken with the magnetic field parallel to the 2DEG is also reported: no effect is seen in this case.

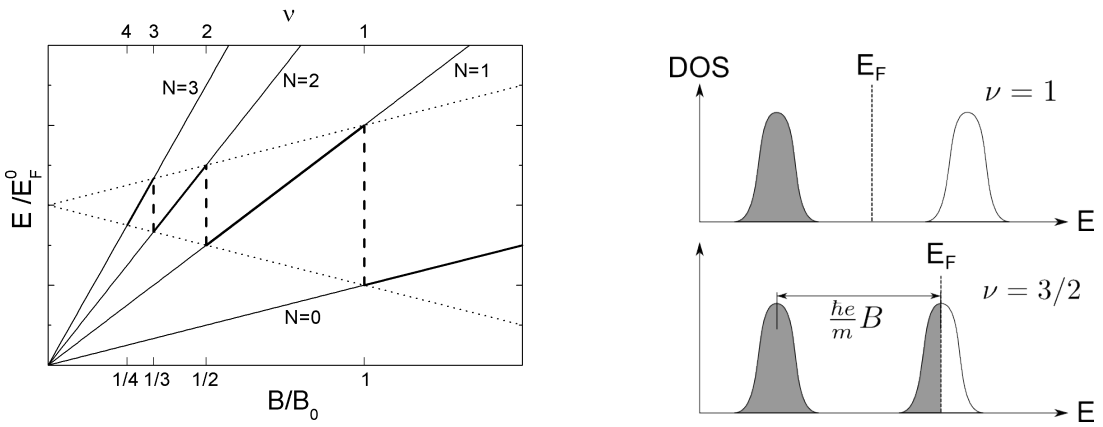

(a) (b)

Fig. 3.5: (a) Variation of the Fermi level (thick line) in a 2DEG with the magnetic field. The energy scale is the Fermi energy at zero magnetic field $E_F^0 = \hbar^2 \pi n_{2D}/m$, the magnetic field scale is $B_0 = 2e/hm$; on the upper scale the filling factor ν is reported. The thinner lines are the Landau levels dispersions, $E_n/E_F^0 = (n + 1/2)B/B_0$. (b) Sketch of the density of states as a function of energy in a magnetic field, with integer filling factor (upper panel) and half integer (lower panel). The vertical lines mark the Fermi level. The Landau levels are plotted with an arbitrary lineshape.

from 0 and have a maximum for half integer values of the filling factor.

Since the conductivity is proportional to the DOS at E_F, it will be zero[2] when E_F lies between two levels, and have a maximum when the DOS has a maximum. Actually, the minimum value of the conductivity is not 0, because, in real samples, the DOS is finite between the Landau levels.

The periodicity of the maxima (or minima) in the conductivity with the magnetic field is then given by the periodicity of the filling factor. In particular, the condition $\nu = n$ is fulfilled at

$$\frac{1}{B_n} = \frac{e}{h}\frac{g_s}{n_{2D}}n. \tag{3.14}$$

In the inset of figure 3.4a an experimental result for the position of the extrema as a function of a sequence of integers is reported, illustrating this relation. This equation shows that the minima are evenly spaced in the inverse magnetic field:

$$\frac{1}{B_{n+1}} - \frac{1}{B_n} = \frac{e}{h}\frac{g_s}{n_{2D}}. \tag{3.15}$$

The carrier density can then be calculated from the position of the extrema, or from the oscillation frequency f:

$$f = \frac{h}{g_s e}n_{2D} \quad \Leftrightarrow \quad n_{2D} = g_s\frac{e}{h}f. \tag{3.16}$$

Note that analogous arguments explain the oscillations in the magnetisation (deHaas–vanAlphen

[2] In this field range $\sigma_{xx} \propto \rho_{xx}$, so that also the resistivity is 0.

effect) and are at the basis of the theory of the integer quantum Hall effect.

When two parallel conductive channels with different carrier density are present in the sample, the sum of the two oscillations causes a modulation in the magnetoresistance (beatings).

In the case of a spin-split conduction band, interesting for this work, there are two conductive channels with very similar density (frequency) and amplitude; hence, a beatings pattern with node is expected; an example can be found in figure 3.4b.

In general, if the two conductive channels are two subbands in the quantum well, their density difference and the frequency difference are proportional

$$n_2 - n_1 = \Delta n = g_s \frac{e}{h} \Delta f, \tag{3.17}$$

g_s being the spin degeneracy.

The energy separation $\Delta E = E_2 - E_1$ between the subband minima is related to Δn by

$$n_2 - n_1 = k_B T \frac{g_s m}{2\pi\hbar^2} \ln \frac{1 + \mathrm{e}^{(E_F - E_2)/k_B T}}{1 + \mathrm{e}^{(E_F - E_1)/k_B T}}. \tag{3.18}$$

Hence, in the limit $k_B T \ll \Delta E \ll E_F$

$$\Delta n = \frac{g_s m}{2\pi\hbar^2} \Delta E \quad \Leftrightarrow \quad \Delta E = \frac{2\pi\hbar^2}{g_s m} \Delta n = \frac{e\hbar}{m} \Delta f. \tag{3.19}$$

In the last formula equation (3.17) is inserted.

The two frequencies can be extracted from the Fourier spectrum of the SdH oscillations, or from the position of the minima of the envelope of the oscillations. The latter method is well suited when the two frequencies are very close (as expected for spin-split channels), since in this case many nodes may be observed in a small magnetic field range (further formulae on nodes and beatings can be found in appendix A). Furthermore, the Fourier spectrum of the experimental data may not be able to resolve two close frequencies. The node method for extracting the spin-splitting energy is reported in the following.

According to Ref. [32], the node analysis considers two spin-split levels with equal amplitude; in this case, the amplitude modulation is given by (see also Appendix A)

$$\text{Amplitude} \propto \cos(\pi\kappa), \quad \kappa = \frac{\delta}{\hbar\omega_c} = \frac{\delta m}{\hbar e B}, \tag{3.20}$$

where δ is the total spin-splitting (spin-orbit and Zeeman); it can be written, as a function of magnetic field B, as:

$$\delta = \delta_0 + \delta_1(\hbar\omega_c) + \delta_2(\hbar\omega_c)^2 + \dots \tag{3.21}$$

The coefficient δ_0, i.e. the zero-field spin-splitting, is the spin-orbit term ($\delta_0 = \Delta E_{so}$). In

AlGaN/GaN heterostructures, because of the large effective mass (with respect to other more common materials, such as GaAs), the 0-th order term is assumed to be the most important up to large fields [96].

The node, or null point, is found for half-integer values of κ; inserting $\kappa = n/2$ in the previous equation, the corresponding magnetic field value is found:

$$B_n = \frac{2m}{\hbar e}\frac{\delta}{n} \quad \Leftrightarrow \quad \delta = \frac{\hbar e}{2m} n B_n, \;\; n \;\text{ odd}. \tag{3.22}$$

The highest-field node corresponds to $\kappa = 1/2$ ($n = 1$), and then

$$\delta = \frac{\hbar e}{2m} B_{last}. \tag{3.23}$$

The larger the splitting, the higher the B_{last} value.

Since it is impossible to define a node as the "last one" (in a measurement up to a finite field), it is useful, when a number of nodes is observed, to perform a linear fit, according to the relation

$$\frac{1}{B_n} = \frac{\hbar e}{2m\delta} n, \tag{3.24}$$

where the n are a sequence of odd integers.

If $\delta = \delta_0$ is assumed, this procedure directly yields the spin-orbit energy splitting. If the first order term in the expansion (3.21) is retained, the function to be fitted is

$$\frac{n}{2} = \frac{\delta_0 m}{\hbar e}\frac{1}{B_n} + 2\delta_1. \tag{3.25}$$

When no node is found, and the oscillations start at B_{min}, equation (3.23) can give an upper limit to δ:

$$\delta < \frac{\hbar e}{2m} B_{min}. \tag{3.26}$$

Otherwise, if nodes cannot be found in an inverse magnetic field range T, the condition can be set as

$$\delta < \frac{\hbar e}{2m\,T}. \tag{3.27}$$

3.3 Low-field quantum corrections: weak localisation and antilocalisation

In this section the weak localisation and antilocalisation effects will be discussed. The quantum corrections due to these phenomena, and their dependence on magnetic field, are the signature of the quantum interference of electrons in disordered systems.

Experimentally, weak localisation is observed as a negative magnetoresistance (defined as

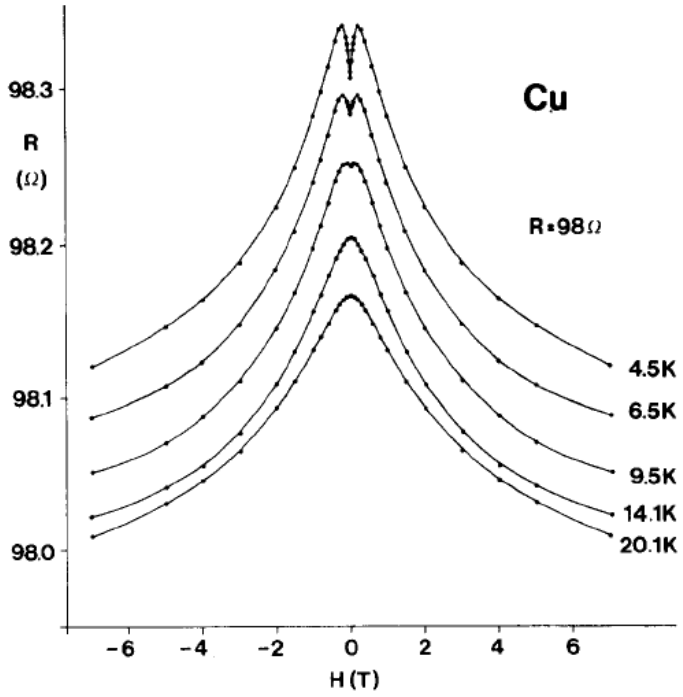

Fig. 3.6: Magnetoresistance curves in a copper thin film, at different temperatures. At the lowest temperature the weak antilocalisation dip can be seen, while at higher temperature only the weak localisation peak is observed [15].

$\rho(0) - \rho(B)$) with a peak at zero field; the weak antilocalisation, which occurs when there is a significant spin-orbit interaction, is revealed as positive magnetoresistance, with a minimum at zero field and possibly a maximum at finite field. Figure 3.6 shows one of the first experimental observation (1984) of both these phenomena in metal thin films [15].

In the real space, the interference causing the weak localisation involves an electron which undergoes multiple scattering, and finally returns to the origin (see figure 3.7a). This closed path can be followed in two time-reversed directions (clockwise and anticlockwise); the electron waves in the two paths finally interfere. In an electric measurement, this interference manifests itself as an increase of the resistance.

A dual description of the phenomenon can be given in the momentum space [15]. An electron in a state $\mathbf{k}$ is scattered at an impurity in a state $\mathbf{k_{1a}}$, and after n scattering events through a sequence of momentum states; it has a finite probability to be in a final state with momentum $-\mathbf{k}$. It can reach the final state also through another sequence starting with $\mathbf{k_{1b}}$, experiencing the same changes in momentum, but in reverse order (figure 3.7b). So, one can see the original electron wave at $\mathbf{k}$ split in two different paths in the momentum space; the two waves propagate (and may experience phase and spin changes) and finally interfere at $-\mathbf{k}$. Since the total change in the momentum they experience is the same, they will have the same phase and interfere constructively.

As long as the two waves remain coherent, the recombination is described in terms of a sum

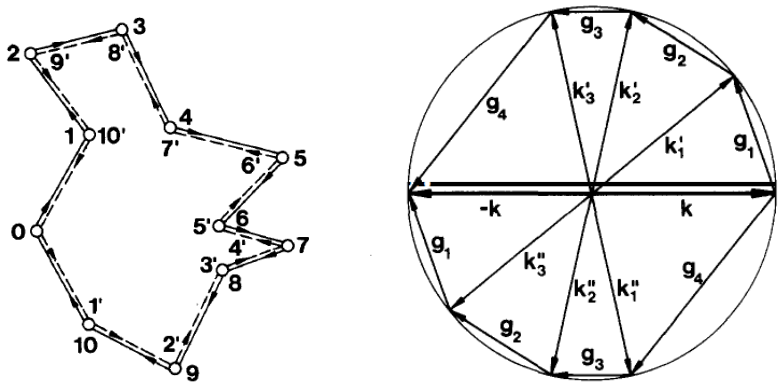

Fig. 3.7: (a) Closed scattering trajectories in the real space; the electron can follow the two time-reversed paths (marked by solid and dashed line). (b) Interfering paths in the momentum space. The momentum states have the same intensity (hence, they lie on a circumference); in the two paths (that in upper side of the circumference and that in the lower) the electrons undergo the same changes in momentum g_i, but in reverse order.

of amplitudes rather than intensities, so that the backscattering is enhanced for constructive interference and leads to the increase in the resistance[3].

When spin-orbit interaction is present in the system, the spin part of the electrons states will contribute to the amplitude of the interference. The spins in two time-reversed paths undergo the same rotation but in opposite direction. Then, at the recombination of the waves, their orientation will differ by a finite amount, so that the interference amplitude is reduced with respect to the case without spin interactions. This reduction leads to the antilocalisation.

Moreover, note that since the electrons are spin-1/2 fermions, the spin has to be rotated by 4π to be brought into itself. Then, a relative rotation of 2π would give two antiparallel spins, and make the interference of the two waves destructive, so that the enhanced backscattering responsible for weak localisation is reduced, and the magnetoresistance changes its sign. In this sense, the measure of the spin-orbit coupling through the weak antilocalisation is an experiment on the fundamental properties of spin-$1/2$ particles [14].

A signature of the weak localisation (or antilocalisation) is found in the dependence on the magnetic field. An external magnetic field breaks the time-reversal symmetry by changing the relative phase of the two opposite trajectories. This reduces the interference and, at large field, restores the resistance to its classical value.

The change in the phase $\Delta\phi$ is given by the magnetic flux through the area S enclosed by the trajectory as $2\pi BS/\Phi_0$, where $\Phi_0 = 2h/e$ is the magnetic flux quantum; since the time-reversed paths are followed in opposite directions, $\Delta\phi$ will be the same, but with different sign.

The typical magnetic field scale (the so-called transport field) in weak localisation experi-

[3] The enhanced backscattering is a common phenomenon for waves scattering in disordered systems; see also Refs. [11][33, chap. 5].

ments is given by

$$B_{tr} = \frac{\hbar}{4eD\tau} = \frac{\hbar}{2el^2}, \tag{3.28}$$

where $l = \sqrt{2D\tau} = v_F\tau$ is the mean free path, τ the transport time and D the diffusion coefficient. At this field, the magnetic flux through an area $S = l^2$ is Φ_0.

Weak localisation correction requires the scattered electrons to keep their phase coherence along the trajectories; the phase breaking rate is thus an important scale in the description of this phenomenon. In magnetoresistance studies, it is introduced through a characteristic magnetic field, the phase coherence field (or phase field) B_φ; it is defined similarly to the transport field B_{tr} as

$$B_\varphi = \frac{\hbar}{4eD\tau_\varphi}, \tag{3.29}$$

The phase relaxation rate is $1/\tau_\varphi$, and τ_φ is the phase coherence time; note that, since $\tau < \tau_\varphi$, $B_{tr} > B_\varphi$. Corresponding to this time scale, the phase coherence length is defined as $l_\varphi = \sqrt{D\tau_\varphi}$. This length sets a cut-off to the length of the paths contributing to the coherent backscattering.

The magnetic field itself can be expressed as a time scale:

$$\tau_B = \frac{\hbar}{4eDB}. \tag{3.30}$$

A magnetic field B cancels the contribution of trajectories corresponding to times larger than τ_B. For a discussion of the weak localisation in terms of time scales, see Ref. [15].

The weak localisation is found to be constant as a function of the magnetic field when $B < B_\varphi$ (see figure 3.8)[4]. Here, it is interesting to report the qualitative derivation of this feature of the weak localisation in terms of time scales. When $B < B_\varphi$, $\tau_B > \tau_\varphi$; in this case, the number of paths that contribute to the coherent backscattering is not limited by B, but by the B_φ: the conductance is thus not affected by the magnetic field. When $\tau_B < \tau_\varphi$, this number of paths begins to shrink, and the conductance varies toward the full restoration of its classical value (i.e., without the quantum correction). This value will be reached when the field is so large that no coherent scattering paths exist.

3.3.1 Theoretical models for weak localisation and antilocalisation

Several models have been developed to pass from the above qualitative considerations to quantitative evaluations.

When the magnetic field is small compared to the transport field, and $B_{tr} \gg B_\varphi$ ($\tau \ll \tau_\varphi$),

[4] This flat trend is not easily noticeable in experimental data such as those in figure 3.6, because B_φ is often very small as compared with the magnetic field range of experiments.

the problem is simplified using the diffusion approximation; that is, the length of the trajectories involved in quantum interference is assumed to be much longer than the mean free path, so that the electrons scatter many time before they interfere. The characteristic magnetic field scales defined above include the diffusion coefficient D, and are thus well defined in this regime.

In this approximation, the magnetoconductance is usually described with the theory of Hikami, Larkin and Nagaoka (HLN) [55]; the magnetoconductance is given by

$$\Delta\sigma_{wl}(B) = -\frac{e^2}{\pi h}\left[\psi\left(\frac{1}{2}+\frac{1}{b}\right) - \psi\left(\frac{1}{2}+\frac{b_\varphi}{b}\right)\right], \tag{3.31}$$

where $b = B/B_{tr}$, $b_\varphi = B_\varphi/B_{tr} = \tau/\tau_\varphi$ and $\psi(x)$ is the digamma function.

When the diffusion approximation is not valid, the system is in the so-called ballistic regime. The validity of the magnetic field scales, as defined above, may be questioned in this case; indeed, also the phase coherence length is defined differently in this regime, when the phase coherence time is close to the scattering time [33, chap. I]. However, the conductance correction depends only on the reduced variables b and b_φ, and thus only on the ratio between the transport time τ and the phase coherence time τ_φ.

Different models have been developed for the ballistic regime, when the diffusion approximation fails [59, 110, 113, 37]. A review of these models, together with a comparison to experimental data, is given by McPhail *et al.* [76]. Despite the different approaches, it is found that the ballistic models give similar magnetoconductance trends for the same values of the parameters.

The first method was developed by Kawabata [59]; this model, however, suffers because of a diverging term, which needs to be compensated by adding "by hand" a suitable term. These weaknesses led to the development of other models. Among them, I mention the model by Zduniak *et al.* [113], and the model by Dmitriev *et al.*[37]; the latter comprises diagrams usually not included in the standard diagrammatic expansion (the so-called "nonbackscattering correction"). Refer to Ref. [76] for the explicit formulae for these models; the result of Zduniak *et al.* is also reported in equation (4.41), page 82.

A comparison of curves obtained with the diffusive model (HLN) and with the ballistic model by Zduniak *et al.* is shown in figure 3.8; the value $b_\varphi = 0.01$ was chosen, since at large b_φ the diffusion approximation is not valid. The two models agree for small values of b; for $B < B_\varphi$ both models give a nearly constant correction. As expected, the models depart for large b, where the diffusion approximation does not hold.

When spin-orbit interaction is also present, the spin coherence must be addressed. If the spin rotates appreciably or dephases during the time τ, i.e. $\tau_{so} < \tau$ (τ_{so} being the spin relaxation time due to spin-orbit interaction), the spin transport is also diffusive. This approximation is often considered also in theories which treat the ballistic case of the weak localisation, as will

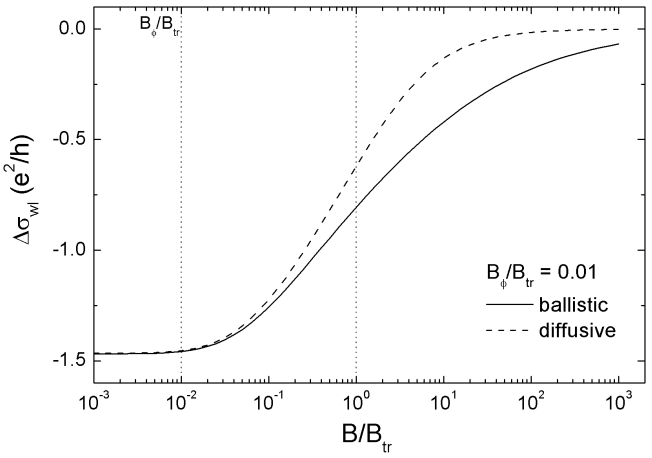

Fig. 3.8: Comparison of weak localisation in the diffusive (HLN) model and in the ballistic model by Zduniak *et al.*, with $b_\varphi = 0.01$.

be discussed in the following.

Similarly to the other characteristic fields, the spin-orbit field is defined as:

$$B_{so} = \frac{\hbar}{4eD\tau_{so}}. \tag{3.32}$$

The relative magnitude of B_φ, B_{tr} and B_{so} defines the actual magnetoresistance pattern as a function of the magnetic field. Figure 3.9 sketches the expected patterns, as a function of the reduced variable b_φ and $b_{so} = B_{so}/B_{tr}$. When the spin-orbit interaction is small (b_{so} is small compared to b_φ), only a weak localisation (WL) maximum in the magnetoresistance is found[5]. At very high spin-orbit interaction, only the antilocalisation (AL) minimum is observed (this case is sometimes referred as "antilocalisation" in contrast to "weak antilocalisation", where a maximum at finite field is observed). Between these extrema, the pattern with a change in the magnetoresistivity sign is found (WAL).

The physics behind these behaviours can be understood in terms of the time scales. When $b_{so} < b_\varphi$, $\tau_{so} > \tau_\varphi$, the spin is not much affected along the trajectories that contribute to the quantum correction, and only the "standard" weak localisation shows up. When $b_{so} > b_\varphi$, $\tau_{so} < \tau_\varphi$, the spin rotates appreciably during the trajectories. In this case the destructive interference is reduced and the antilocalisation maximum appears.

Different models have been proposed, as summarised in table 3.1. Some of them are valid in the diffusion approximation only, as defined above; some are valid only for small spin-orbit coupling. They have been developed to be applied to the study of the spin-orbit interaction in zinc-blende, which, as discussed in section 2.1, has a linear (Rashba) and cubic (Dresselhaus) term in k; the case of wurtzite is simpler since the interaction has only a linear Rashba-like term

[5] For example, in Ref. [82] is observed a weak localisation curve in a GaN 2DEG, claiming that the different spin-orbit terms exactly cancel each other (see section 2.2): indeed, from the reported phase coherence time, one can estimate the spin splitting to be smaller than 0.4 meV.

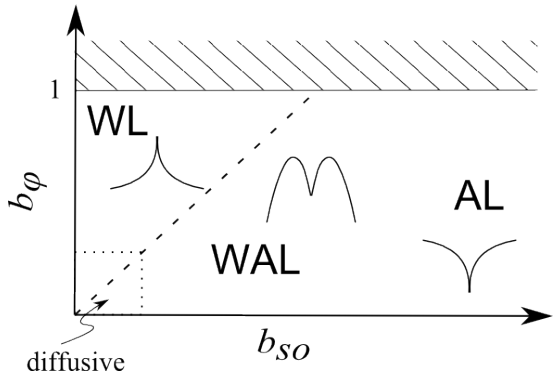

Fig. 3.9: Sketch of the magnetoresistance patterns as a function of the parameters $b_\varphi = B_\varphi/B_{tr} = \tau/\tau_\varphi$ and $b_{so} = B_{so}/B_{tr} = \tau/\tau_{so}$. b_φ has an upper bound at 1 since τ cannot exceed τ_φ. The diffusive region, when B_{tr} is much larger than the other field scale, is also marked.

(see section 2.2).

Finally, the different models consider different aspects of the spin-orbit interaction. In the first attempts, the spin-orbit coupling was treated only as a spin relaxation effect, which reduces the coherence of the interfering waves; in this sense, the spin-orbit interaction is described as a relaxation rate τ_{so}^{-1} to be added to the phase relaxation, regardless of the details of the spin-orbit mechanism. The actual Hamiltonian of the interaction is not explicitly considered. This approach was followed in the earlier work by Hikami *et al.* [55] and Kawabata [59], and later by Zduniak *et al.* [113].

Subsequently, it has been shown that the spin-orbit interaction can be described through a spin-dependent vector potential [8], which contributes as a spin-dependent Berry phase (also referred as Berry-like spin phase, or spin-dependent Aharonov–Bohm effect). In the case of Rashba interaction, the hamiltonian can be rewritten as [78, 84]:

$$H = \frac{\hbar^2\mathbf{k}^2}{2m} + \hbar\alpha\boldsymbol{\sigma}\cdot(\hat{z}\times\mathbf{k}) = \frac{\hbar^2}{2m}\left(\mathbf{k} - 2e\mathbf{A}_S\right)^2, \tag{3.33a}$$

$$\mathbf{A}_S = \frac{m\alpha}{2e\hbar^2}(-\sigma_y, \sigma_x). \tag{3.33b}$$

The inclusion of the spin-orbit coupling via the complete hamiltonian in weak antilocalisation calculation yields a correct formula. One of the first and most used model which uses explicitly the spin-orbit hamiltonian was derived by Iordanskii, Lyanda-Geller and Pikus (ILP) [56], in the diffusion approximation (both B_φ and B_{so} are much smaller than B_{tr}); it includes both linear and cubic interactions.

Their result was finally simplified, for the case of linear spin-orbit only, in a closed-form formula by Punnoose [84]. The author noted that his result can be interpreted in terms of both spin relaxation and spin Berry phase; indeed, when $B \ll B_{so}$, the equation reduces to the HLN model, and B_{so} describes spin relaxation; when $B \gg B_{so}$ the SOI acts as a gauge field.

In the ballistic regime, the effect of spin-orbit interaction can be included again as a relaxa-

Model (year)	Diffusive/ ballistic	SOI description	SOI strength	SOI type
HLN [55] (1980)	diffusive	relaxation		
Kawabata [59] (1984)	ballistic	relaxation		
ILP [56] (1994)	diffusive	full	weak	linear + cubic
Zduniak *et al.* [113] (1997)	ballistic	relaxation	weak	
Miller *et al.* [78] (2003)	ballistic	full (2 par.)	full	linear + cubic
Golub [50] (2005)	ballistic	full	full	linear
Glazov & Golub [48] (2006)	ballistic	full	full	linear + cubic
Punnoose [84] (2006)	diffusive	full	weak	linear

Tab. 3.1: Comparison of weak antilocalisation models. In the "SOI description" column the interpretation as time relaxation only or with the complete hamiltonian ("full") is marked. The range of validity for different intensity of the SOI is indicated in the column "SOI strength" as weak (small SOI only) or full range.

tion rate which sums to the phase relaxation; Kawabata [59] and Zduniak *et al.* [113] followed this procedure.

The model by Miller *et al.* [78] explicitly considers the Aharonov–Bohm-like effect. This effect comes out to be dominant in a first order approximation, and is described by a parameter B_{eff}; the spin relaxation is a higher orders correction, described by B_{so}. Referring to figure 3.9, both B_{eff} and B_{so} must be small in order to observe only the weak localisation maximum.

Finally, the model by Golub [50] extends the ILP model to the ballistic region and to arbitrary strength of the spin-orbit interaction, for linear SOI only; it was extended to the case with both linear and cubic terms by Glazov and Golub [48]. This model includes also the terms which are interpreted as "nonbackscattering" corrections. If the weak localisation is described in terms of angular dependence of an effective scattering cross section for a single impurity, the enhanced backscattering implies that the cross section has a peak at an angle $\theta = \pi$. This peak is derived, in a diagrammatic expansion, from the contribution of the so-called maximally crossed diagrams, which are usually the only ones retained. When other kinds of diagrams are taken into account, they contribute to a reduction of the cross section at $\theta \neq \pi$: these are the nonbackscattering corrections.

The theory of weak (anti)localisation is usually treated in the Green function formalism, with diagrammatic expansions, and the conductivity is then calculated using the Kubo formula [41, chap. 7.5][33, chap. 5][43, 15, 36].

To deal with the spin-orbit interaction, the problem is decomposed in the S, S_z basis, where

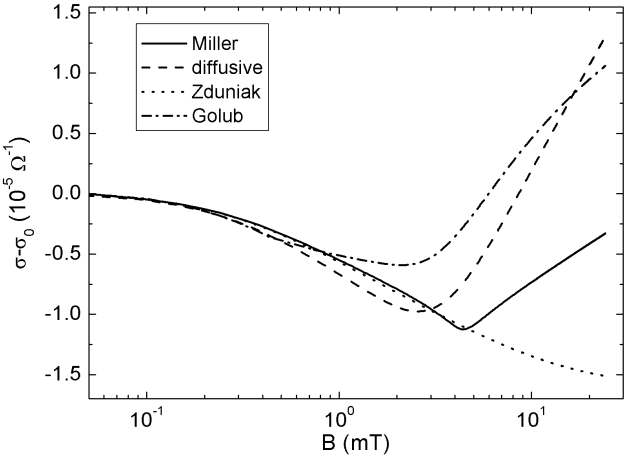

Fig. 3.10: Comparison of the diffusive, Miller, Zduniak and Golub models for weak antilocalisation, as a function of the magnetic field B. The 2DEG has density $n = 1 \cdot 10^{17}$ m^{-2} and mobility $\mu = 0.5$ m^2/Vs ($\tau = 0.63$ ps), the energy splitting is $\Delta E = 1$ meV, and the phase coherence time τ_φ is 50 ps ($b_\varphi \approx 0.01$); for the Miller model, the additional spin-orbit relaxation time is 120 ps.

S is the total spin of the two particles and S_z its z component; the singlet and triplet parts are treated separately. It is found that the singlet term has an "antilocalising" behaviour (i.e., it would give a maximum at zero field in the magnetoconductance), while the triplet part is "localising".

The spin-orbit interaction affects the triplet only. When spin-orbit is important, the singlet part can dominate, at least at the lower fields, and the antilocalisation is observed. When the spin-orbit is small, the triplet part dominates, since it has a triple multiplicity.

The formulae for the weak antilocalisation models are reported in section 4.3.3.1, to be discussed with the experimental results.

I calculated the magnetoconductivity for the different models described above for the same set of physical parameters; in particular, an energy splitting of $\Delta E = 1$ meV is chosen. Figure 3.10 shows this comparison.

Finally, in figure 3.11, conductance curves are reported for different strengths of the spin-orbit interaction (parametrised by the precession angle $\Omega\tau$), as calculated with the model of Golub. At small $\Omega\tau$ (small SOI), only the weak localisation minimum is found; moreover, it can be seen that at large field the curves are close to the $\Omega\tau = 0$ curve. For $\Omega\tau \to \infty$ only the antilocalisation peak is found. For $B \to \infty$ the correction is given by a universal curve (which depends only on B/B_{tr}), marked by σ_{hf}.

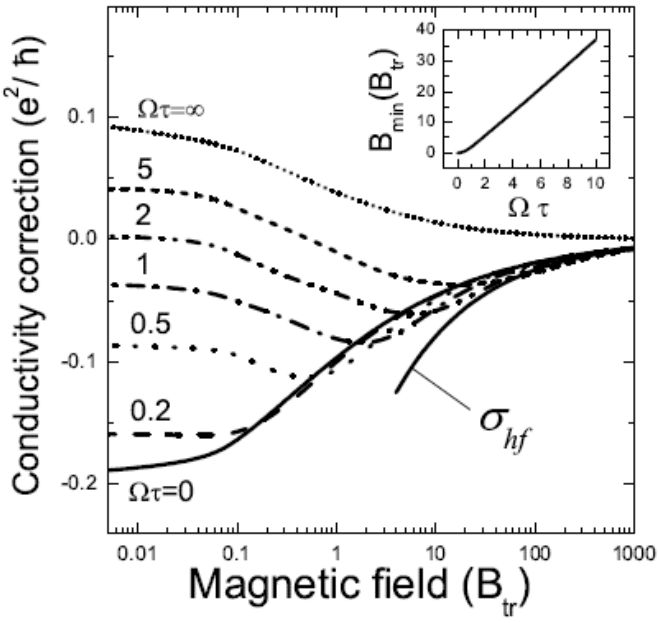

Fig. 3.11: Conductivity correction calculated with the Golub model for different strengths of spin-orbit interaction, for fixed $\tau/\tau_\varphi = 0.01$. The curve σ_{hf} is the high field approximation. From Ref. [50].

4. EXPERIMENTAL RESULTS AND DATA ANALYSIS

In this chapter, the results of magnetotransport experiments will be presented and discussed. The three effects — classical magnetoresistance, Shubnikov–deHaas, weak antilocalisation —, described in the previous chapter, have been investigated. Classical magnetoresistance provided a characterisation of the samples, while the others are aimed at the study of spin-orbit interaction.

4.1 Experimental details

Two different samples of GaN-based 2DEG have been investigated during this work (figure 4.1).

Sample A is a heterostructure with exclusion layer (see section 1.2.2); it has a carrier density close to $1 \cdot 10^{17}$ m^{-2} and a mobility of about 2 m^2/Vs at 0.25 K.

Sample B does not have an exclusion layer. The carrier density is again close to $1 \cdot 10^{17}$ m^{-2}, but the mobility is about 0.5 m^2/Vs at 0.25 K.

The properties of the 2DEG were studied in devices with the Hall bar layout (as shown in figure 4.2), with two ohmic contacts for injection and extraction of the current and four ohmic voltage probe contacts. These devices were defined by optical lithography. Ohmic contacts were obtained through Ti/Al/Ni/Au deposition followed by rapid thermal annealing at 850 °C.

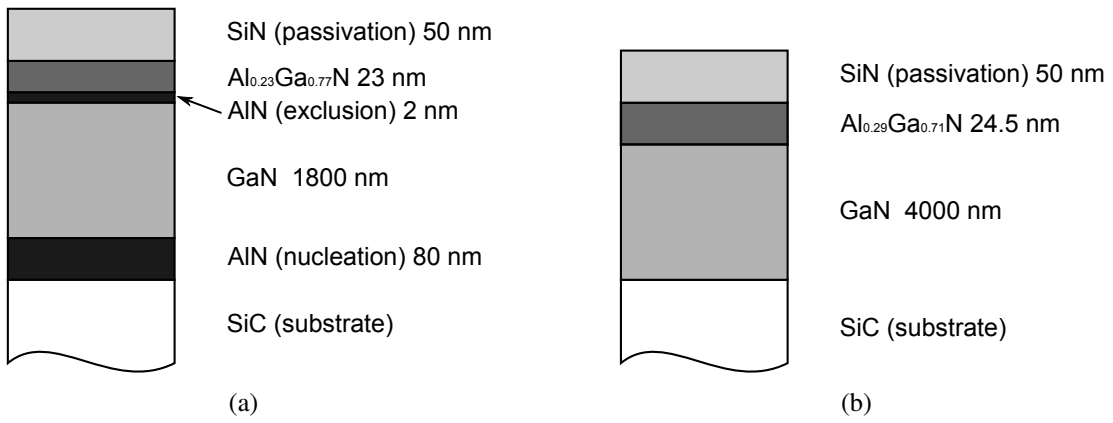

Fig. 4.1: Layers sequence for Sample A and B.

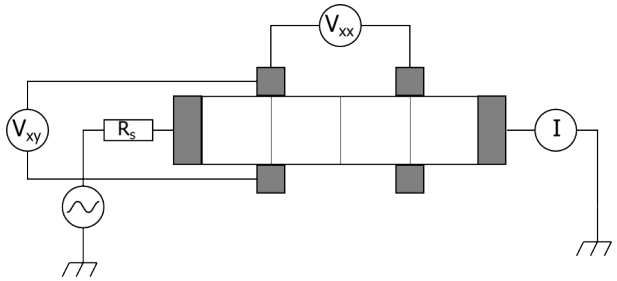

Fig. 4.2: Diagram of the four wire measurements configuration.

Electrical isolation was achieved via ion implantation.

Magnetotransport properties were measured either by a low frequency lock-in technique or by DC technique, in presence of a perpendicular magnetic field. Two cryogenic apparatus have been employed. A helium compression cryostat, available in the Laboratorio di Fisica e Tecnologia dei Semiconduttori (Laboratory of Physics and Technology of Semiconductors) at Università Roma Tre, measures from room temperature to 15 K. An external magnet allows magnetotransport experiments up to 0.7 T. An ^{3}He condensation cryostat (the *Heliox* from Oxford Instruments), capable of a lower temperature of 0.25 K, was employed for the lowest temperature. The cryostat is dipped in liquid helium, in a dewar vessel equipped with a superconducting magnet whose maximum field is 12 T. This apparatus could be used thanks to the collaboration with the NEST laboratory of the Scuola Normale Superiore in Pisa.

The lock-in technique uses an AC excitation and detects it through lock-in amplifiers. The frequency is chosen to be small enough to avoid any low-pass effect from the device, and to be far enough from the power line noise at 50 Hz and its integral multiples; since the lock-in amplifiers used during this work have notch filters for these frequencies, whose band-stop width is about 10 Hz, a frequency smaller than 40 Hz is chosen; in particular, a value of 17 Hz was employed.

The measurements were performed using a four wire, current bias configuration (figure 4.2). The current bias is obtained with a voltage source and a series resistor R_s. This resistance value is much larger than the resistance of the device, so that the current is nearly constant during device characterisation.

4.2 Sample A

The $Al_xGa_{1-x}N$/AlN/GaN heterostructure was grown by metal-organic chemical vapour deposition (CVD) on a SiC substrate. The layer sequence consists of an 80 nm-thick AlN nucleation layer followed by a 1.8 µm-thick GaN buffer, a 2 nm-thick AlN exclusion layer and 23 nm-thick $Al_{0.23}Ga_{0.77}N$ layer. Finally, the heterostructure was passivated by depositing a 50 nm-thick SiN layer using plasma enhanced CVD. The 2DEG forms in the GaN layer thanks to the

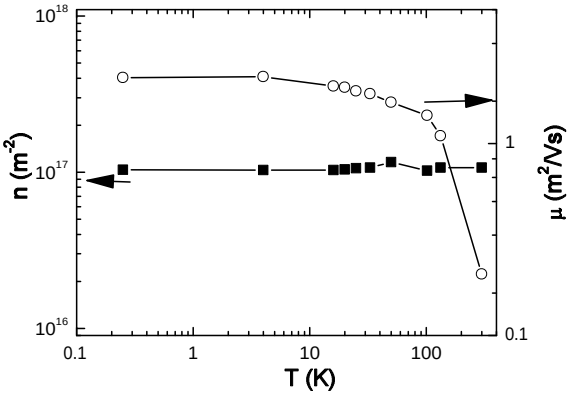

Fig. 4.3: 2DEG carrier density (open symbols) and mobility (full symbols) as a function of temperature, as obtained from classical Hall effect measurement in Sample A. Lines are guides for eyes.

large spontaneous and piezoelectric polarisation present in the heterostructure, as described in section 1.2.1.

Four Hall bars, different in size and in the geometry, were investigated on this sample. Of them, device 1 is a standard 100×200 μm^2 Hall bar; device 2 is a 10×20 μm^2 Hall bar partially covered by split-gate electrodes (less than 5% on the surface), whose geometry was designed for the study of transport in quantum point contact; devices 3 is a 100×200 μm^2 Hall bar completely covered by a gate electrode; device 4 is a 100×200 μm^2 Hall bar with a 1 μm wide transverse gate.

Classical Hall effect measurements at low fixed magnetic field allowed a characterisation of the main features of the 2DEG. The four devices showed similar results. In figure 4.3 typical carrier density and mobility as a function of temperature are reported. The carrier density is constant at about $1.04 \cdot 10^{17}$ m^{-2}, as expected and reported [92] in the case of a 2DEG due to polarisation effects, without intentional doping. The mobility at room temperature is about 0.2 m^2/Vs and rises to 2.2 m^2/Vs at the lowest temperature.

The high mobility and high carrier density of the sample imply a long mean free path (1.2 μm) and thus allows the investigation of transport in the ballistic regime [12], i.e. in devices whose length is smaller than the mean free path[1]. The experiments on these devices confirm the quality of the material, and are described in appendix E.

4.2.1 Classical magnetotransport characterisation

In this section, prior to the discussion of Shubnikov–deHaas effect, an analysis of the classical Drude magnetoresistance, investigated in the reduced conductivity tensor formalism (see section 3.1), is presented.

[1] Note that also in the discussion of the weak localisation a "ballistic regime" is defined (section 3.3); although the two concepts are similar in principle (both refer to the reduced effect of scattering), they have a slightly different meaning in the two contests.

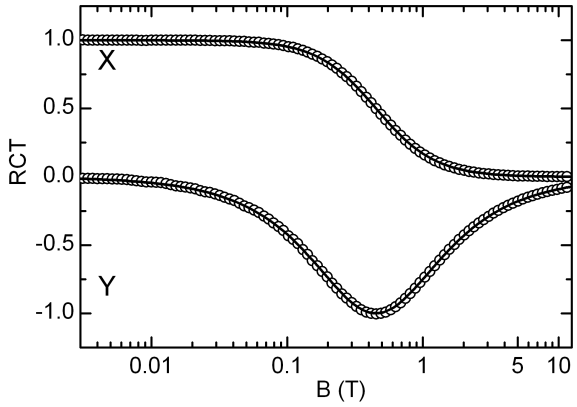

Fig. 4.4: Components X and Y (circles) of the reduced conductivity tensor as a function of magnetic field for device 1, measured at T=0.25 K and least-square fits of data (continuous lines) obtained in the hypothesis of only one conducting channel in the sample. The number of experimental points shown in the graph is reduced (for representation purpose only) with respect to the acquired points, with a ratio of 1:40.

The two experimental RCT components are reported in figure 4.4. Note that, although the magnetic field reaches 12 T, SdH oscillations are barely visible on this scale.

A model with only one channel has been fitted to the data; it is shown in the figure as continuous lines. It can be seen to reproduce very well the experimental data; the obtained value for the mobility is 2.2 m^2/Vs is in excellent agreement with the fixed field measurements. Attempts to fit a model with two channels result in theoretical curves similar to those reported in the figure, provided that the channels have similar conductivity and mobilities differing less than 10%.

Therefore, these data are compatible with the presence of two parallel channels, but put severe constraints on their carrier density and mobility values.

4.2.2 Shubnikov–deHaas effect

At the lowest temperatures Shubnikov–deHaas effect can be observed in the longitudinal magnetoresistance of all the devices. In figure 4.5 two curves are reported, taken at 0.25 K, on device 1 and 2; devices 3 and 4 show results similar to that of device 1 and are not shown.

In all devices the oscillations are clearly seen at field higher than 3 T. In device 2 a beating node (marked by an arrow in the figure) can be observed at about 5 T, while in devices 1, 3 and 4 this feature is not visible by inspection. The SdH oscillations are superimposed to a slowly varying background; the procedure for its subtraction and its physical origin is further discussed in appendix C.

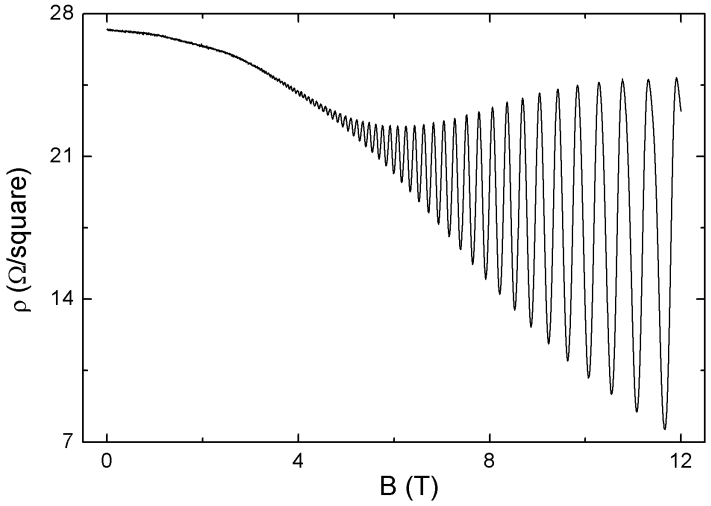

(a)

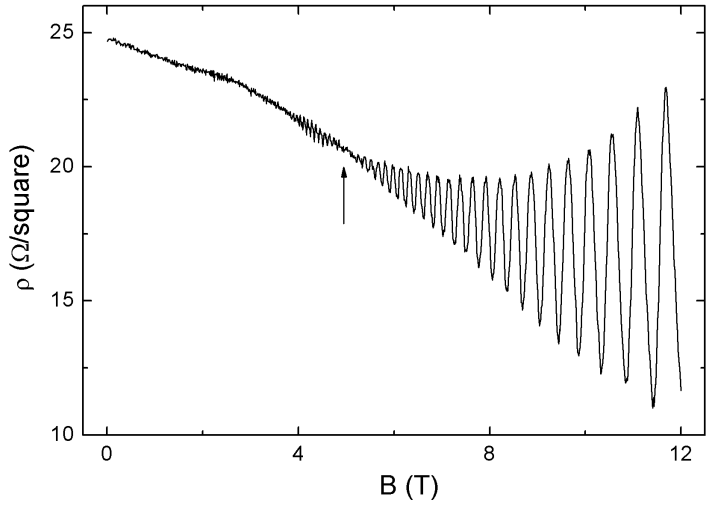

(b)

Fig. 4.5: Longitudinal resistivity as a function of magnetic field for device 1 (a) and device 2 (b).

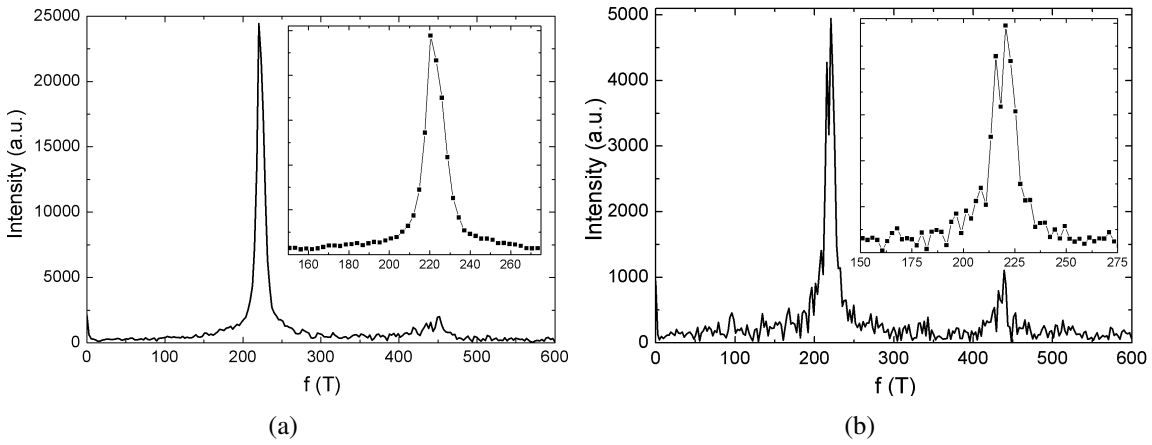

Fig. 4.6: Fast Fourier Transform spectra of the magnetoresistivity of devices 1 (a) and 2 (b). Insets are details of the main peak.

4.2.2.1 Frequency domain analysis

The investigation of the oscillations in the frequency domain was performed through a standard Fast Fourier Transform (FFT) operation on the data, taken as a function of the inverse magnetic field. Since the data were acquired in equal spacing in B, an interpolation of the data was performed prior to the transformation. The number of points in the interpolation was chosen to be close to the number of actual experimental points. Moreover, the background was subtracted from the curve before the transformation. The window function for the FFT was the rectangular function, since this window function is expected to give the maximum resolution, as discussed in the following. The FFT for devices 1 and 2 are shown in figure 4.6; devices 3 and 4 gave results similar to those of device 1.

In device 1 spectrum, a single, slightly asymmetric peak at frequency $f = 221.8$ T is found. The corresponding carrier density, assuming spin degeneracy, is $n = 1.07 \cdot 10^{17}$ m^{-2}, in excellent agreement with the value determined by the Hall measurement.

As for device 2, a split peak is seen, corresponding to the beating visible in the data. The two peak frequencies are 215.8 T and 220.6 T.

The small peak found for both devices at higher frequency (close to 440 T) is related to the second harmonic component of SdH oscillations.

The data have been investigated in the time-frequency domain also, through a spectrogram (figure 4.7). It can be seen that the frequency peak position is constant in the magnetic field range where the oscillations can be observed. In device 2 the position of the null point is clearly visible at about 0.2 T^{-1}. Note that the frequency resolution of spectrograms is worse than the resolution of standard FFT, because the data are split in a number of shorter segments, that are then Fourier transformed.

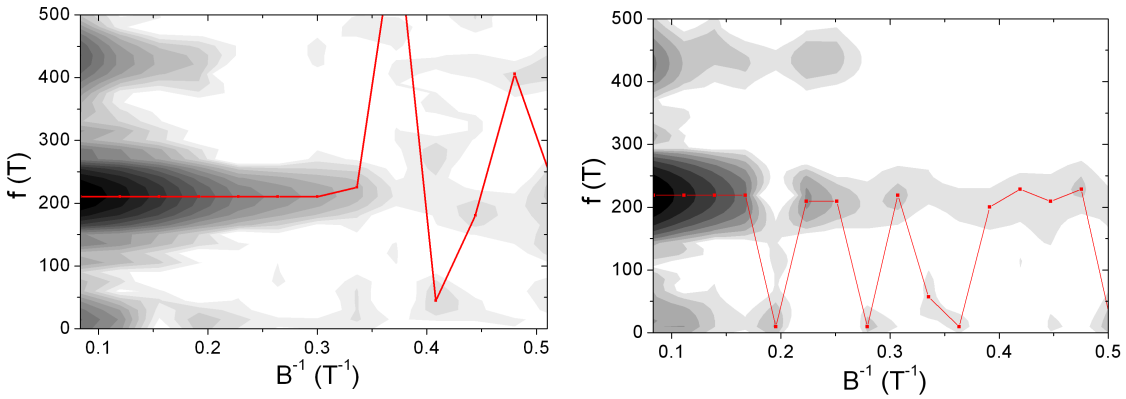

Fig. 4.7: Spectrogram of the SdH data for (a) device 1 and (b) device 2. The line marks the position of the maximum in the FFT as a function of the inverse magnetic field. Darker regions have the highest spectrum amplitude.

To explain the different behaviour of devices 1, 3 and 4 and device 2, we can consider that the main difference between device 2 and the other devices is in the Hall bar area, the former being almost two orders of magnitude smaller than the latter. It is reasonable to argue, therefore, that the oscillation frequency of the larger devices had a broader distribution due to the average on a larger area, resulting in wider FFT components that could not be resolved.

The upper bound to resolution and ability of the FFT technique to detect two channels comes from the finiteness and discreteness of the signal to be transformed. For a generic signal extended in the time domain between t_{min} and t_{max}, the frequency step is given by

$$\text{step}(f) = \frac{1}{t_{max} - t_{min}}. \tag{4.1}$$

In the SdH case the formula is:

$$\text{step}(f) = \frac{1}{(1/B)_{max} - (1/B)_{min}} = \left[\frac{1}{B_{min}} - \frac{1}{B_{max}}\right]^{-1}. \tag{4.2}$$

The maximum field is limited by the experimental set-up and by the onset of the quantum Hall effect regime, while the minimum field is related to the damping of the oscillations, i.e. to mobility and temperature.

In the present case, B_{max} is 12 T, and B_{min} is 3 T. The resulting frequency step is 4.5 T; the splitting found in device 2 is very close to the limit posed by the measuring frequency step. Furthermore, these arguments set a limit to the energy resolution, according to the relation $\text{step}(E) = e\hbar\ \text{step}(f)/m = 2.1$ meV.

Moreover, the width of the peak, given by the convolution of the natural lineshape with the Fourier spectrum of the window function applied in the transformation, further reduces the resolution.

The so-called "zero-padding" (i.e., the extension of the signal to an arbitrary length by appending zeroes to it) can be applied to have a better sensitivity, but cannot result in a better resolution, i.e. in the ability to discriminate between closer frequencies, because of the limitation due to the window function. Indeed, if one assumes to measure a finite part of a signal on a infinite time range, the resulting spectrum with the zero-padding is a better numerical approximation of the convolution of the spectra of the window function and the infinitely long signal, not of the infinitely long signal itself.

Thus, in order to resolve two close frequencies, the zero-padding is not required, while a window function whose spectrum has a narrow main lobe is needed. The better window function for this purpose is the rectangular function, or rect.

In summary, the analyses of magnetotransport data we have reported thus far —using classical magnetoresistance and frequency analysis of the SdH effect— are compatible with the existence of two parallel channels with similar conducting characteristics but do not prove unambiguously their presence. Therefore, a more subtle scrutiny is required based on the amplitude and phase of the SdH oscillations, which is very sensitive to the presence of multiple conducting channels.

4.2.3 Amplitude and phase modulation of SdH effect

The SdH oscillations contain more information than that given by a frequency domain analysis only. Their damping depends on the density of states of the 2DEG in a magnetic field, and, as will be shown in the following, can give a deeper knowledge of the investigated system. Besides the amplitude, the phase modulation provides further evidences on these details. This kind of analysis can be applied to the search of the two spin-split channels.

In particular, the analysis should be applied to devices 1, 3 and 4, which do not exhibit clear signatures of the two channels in the standard analysis.

Before starting the analysis of the experimental data, I will recall some details on lineshape of Landau levels and damping of the SdH oscillations.

4.2.3.1 Landau level lineshape and amplitude damping

The lineshape of a Landau levels is not a delta function, as assumed in section 3.2. It has a finite width due to temperature and lifetime, i.e., an electron has a finite probability to be scattered out of a Landau level[2].

[2] At higher field, in the quantum Hall regime, this probability is heavily affected by the topological nature of the states of a 2DEG in these conditions (for a general introduction, see [41, chap. 4]). This problem will not be treated in this work, and the formulae given in this section are not valid in that regime.

The associated lifetime, referred to as single particle lifetime, or total scattering time, or "quantum lifetime" τ_q, is given by the inverse of the integral of the scattering probability $W(\theta)$:

$$\frac{1}{\tau_q} = \int_0^\pi W(\theta)\mathrm{d}\theta. \tag{4.3}$$

It is different from the "transport lifetime" τ_t, which is considered in the Drude theory and is related to the transport mobility:

$$\frac{1}{\tau_t} = \int_0^\pi W(\theta)(1-\cos\theta)\mathrm{d}\theta. \tag{4.4}$$

The transport lifetime defines the relaxation of the momentum of the electron through scattering.

The quantum lifetime defines also the "quantum mobility" $\mu_q = e\tau_q/m$, analogous to the transport mobility $\mu_t = e\tau_t/m$.

Qualitatively, SdH oscillations are visible when the Landau levels are sufficiently distinct, i.e. when their separation is larger than their broadening; this limiting condition is commonly taken as $\omega_c\tau_q = \mu_q B > 1$.

The functional form of the Landau level lineshape has been the subject of a large debate. In the study of the SdH effect, a lorentzian lineshape with field-independent broadening is usually considered. This lineshape is obtained from theoretical calculation using the self-consistent Born approximation and assuming the broadening to be larger than the level spacing. This lineshape has also been experimentally verified [57, 31, 83, 30, 38] (see also Ref. [83] for a discussion of proposed functional forms for the lineshape and its experimental investigation). Elliptic or gaussian lineshape have also been considered [7].

The density of states of the Landau levels is usually written as [38]

$$D(E) = \frac{2e}{h}B\sum_{n=0}^{\infty} P(E-E_n). \tag{4.5}$$

$P(E)$ is the lineshape and E_n is the energy of the n-th Landau level. The lorentzian lineshape is

$$P_L(E) = \frac{\Gamma_L}{\pi}\frac{1}{E^2+\Gamma_L^2}, \quad \Gamma_L = \frac{e\hbar}{2m\mu_q}. \tag{4.6}$$

This DOS can be written as a sum of a constant and an oscillating part, using the Poisson

summation formula[3][85, 38]. The oscillating resistivity is found using the relation [31]

$$\frac{\delta\rho}{\rho_0} = D_T \frac{\delta D(E_F)}{D_0}, \tag{4.7}$$

where the $\delta\rho$ and $\delta D(E_F)$ are the oscillating parts of resistivity and DOS at the Fermi energy, respectively, and ρ_0 and D_0 are the non-oscillating part; D_T account for the thermal damping. For the series in equation (4.5) the Poisson formula yields a cosine series, and the lorentzian function is mapped onto an exponential damping for each cosine term.

From the above formulae, the complete expression for the Shubnikov–deHaas oscillations has been derived through diagrammatic techniques in the self-consistent Born approximation for short range scattering and at finite temperature [7, 57]; it is given by [31]

$$\frac{\delta\rho_{xx}}{4\rho_0} = \sum_{s=1}^{\infty} D_T(sx) \exp\left(-\frac{s\pi}{\omega_c\tau_q}\right) \cos\left(\frac{2\pi s E_F}{\hbar\omega_c} + s\pi\right), \tag{4.8}$$

where ρ_0 is the zero-field value. $D_T(sx)$ is the thermal damping factor:

$$D_T(sx) = \frac{sx}{\sinh sx}, \quad x = \frac{2\pi^2 k_B T}{\hbar\omega_c}. \tag{4.9}$$

From this summation, only the first harmonic is usually retained, so that the oscillating part of the resistivity is given by

$$\frac{\delta\rho_{xx}}{4\rho_0} = D_T(x) \exp\left(-\frac{\pi}{\mu_q B}\right) \cos\left(\frac{2\pi f}{B} + \pi\right). \tag{4.10}$$

In order to investigate the amplitude damping, having removed the temperature dependence, the quantity

$$\ln\left(\frac{\Delta\rho_{xx}}{4\rho_0 D_T(x)}\right) = -\frac{\pi}{\mu_q B} \tag{4.11}$$

is considered, where $\Delta\rho_{xx}$ is the amplitude of the oscillations.

Upon extracting the values in the left-hand side of this equation from the experimental data, the so-called "Dingle Plot", this linear relation allows the extraction of μ_q (and then τ_q).

As will be shown, deviations from linear behaviour in the Dingle plot can be due to non-lorentzian lineshape, carrier density disomogeneity, or parallel channels [29]. Suitable models can be developed to take into account these effects and extract the respective parameters.

[3] The formula

$$\sum_{n=-\infty}^{\infty} g(n) = \sum_{k=-\infty}^{\infty} \hat{g}(k)$$

relates the series of functions g to the series of its Fourier transforms $\hat{g}$.

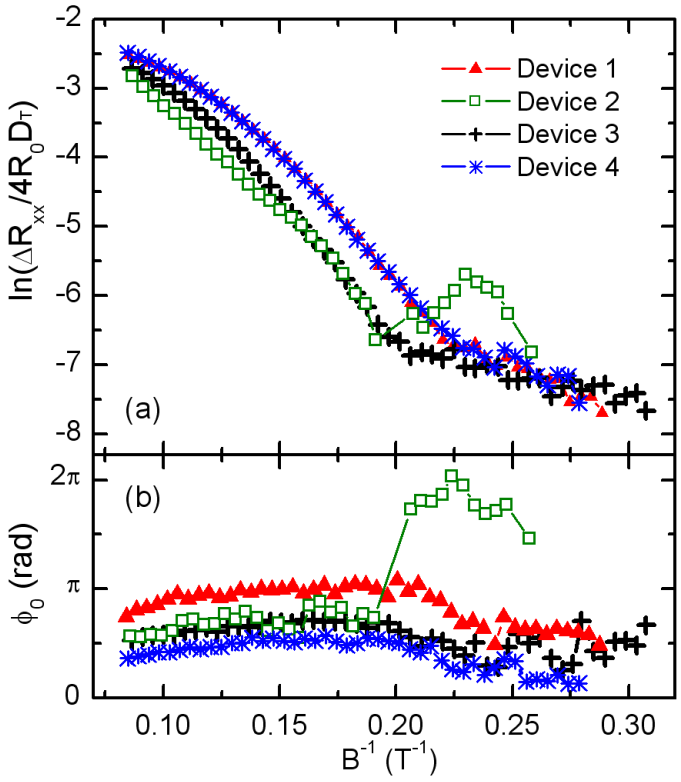

Fig. 4.8: (a) Dingle plots and (b) residual phases as a function of the inverse of magnetic field of the four investigated devices.

Figure 4.8a reports the Dingle plots for the investigated devices. All the curves exhibit a non-linear dependence on B^{-1} and a slope variation between 0.2 T^{-1} and 0.25 T^{-1}, which becomes a pronounced dip in the case of device 2. The different lineshape of device 2 reflects the presence of the beating node in the SdH curve. The behaviour observed in figure 4.8a is not consistent with the presence of a single conducting channel.

To gain further information we have also analysed in details the phase of the SdH oscillations. The residual phase ϕ_0 can be extracted from the oscillations, as described in appendix A.2, using the formula

$$2\pi f_0/B_m + \phi_0 = 2\pi m, \quad m = 0, 1, 2 \ldots, \tag{4.12}$$

where $1/B_m$ are the positions of the maxima and f_0 a trial frequency. The residual phase is reported in figure 4.8b. The trial frequency is determined from a least-square fit, and is very close to the FFT peak frequency.

The main features of the measured phase behaviour as a function of B^{-1} are the jumps concomitant with the variation of slope in the Dingle plots. Similarly to the dip in the Dingle plot, device 2 exhibits a sharper feature than the other devices in the phase behaviour. The variation of the residual phase requires the presence of two frequency components in the SdH

oscillations pattern: indeed, in case of a single conducting channel (thus a single frequency component) the phase should be constant and equal to π rad.

The non-linear behaviour of the Dingle plots and the phase variation bear conclusive evidence that these SdH oscillations cannot be described in terms of a simple one-channel model that leads to equation (4.11).

4.2.3.2 Extension of the Dingle plot analysis

A second conducting channel in the Shubnikov–deHaas effect can be introduced by considering a sum of terms of the same kind of equation (4.10) [91].

Assuming the standard lorentzian lineshape, the sum is

$$\begin{aligned}\frac{\delta\rho_{xx}}{D_T} \propto & \sigma_1 \exp\left(-\frac{\pi}{\mu_1^{(q)}B}\right)\cos\left(\frac{2\pi f_1}{B}+\pi\right)+ \\ & +\sigma_2 \exp\left(-\frac{\pi}{\mu_2^{(q)}B}\right)\cos\left(\frac{2\pi f_2}{B}+\pi\right)+\end{aligned} \tag{4.13}$$

and the resulting Dingle plot is

$$\begin{aligned}\ln\frac{\Delta\rho_{xx}}{D_T} = & const - \frac{\pi}{\mu_1^{(q)}B} + \frac{1}{2}\ln\left[1+\left(\frac{1-\Delta f/2f_0}{1+\Delta f/2f_0}\frac{\mu_2^{(t)}}{\mu_1^{(t)}}\right)^2 \exp\left(-\frac{2\pi}{\mu_2^{(q)}B}+\frac{2\pi}{\mu_1^{(q)}B}\right)+\right. \\ & \left.+2\left(\frac{1-\Delta f/2f_0}{1+\Delta f/2f_0}\frac{\mu_2^{(t)}}{\mu_1^{(t)}}\right)\exp\left(-\frac{\pi}{\mu_2^{(q)}B}+\frac{\pi}{\mu_1^{(q)}B}\right)\cos\left(\frac{2\pi\Delta f}{B}\right)\right],\end{aligned} \tag{4.14}$$

where $f_0 = (f_1 + f_2)/2$ and $\Delta f_0 = f_1 - f_2$. Details of the derivation of the formulae can be found in Appendix A.

This equation can be simplified if the ratio between the transport mobility $\mu_{1,2}^{(t)}$ and the quantum mobility $\mu_{1,2}^{(q)}$ is assumed to be the same for the two channels.

The important feature of a SdH pattern with two components with different amplitudes is that the resulting oscillations may have an envelope which does not show clearly the null point expected in a beating pattern, because of the natural amplitude damping. In figure 4.9 simulated Dingle plots and phase plots are presented for the case of two components, with different average quantum mobility and $\mu_1/\mu_2 = 0.9$; panels (a) and (c) report the case of the lorentzian lineshape. For comparison the simulation is also shown for the case of two channels with $\mu_1/\mu_2 = 0.99$ and μ_1 =0.5 m^2/Vs. Panels (b) and (d) are discussed in the following.

It can be seen that a large mobility is required to observe a clear minimum in the amplitude. In the phase plots, we can observe that at high mobility a sharper step is found, although it is not as sharp as the case of equal mobility.

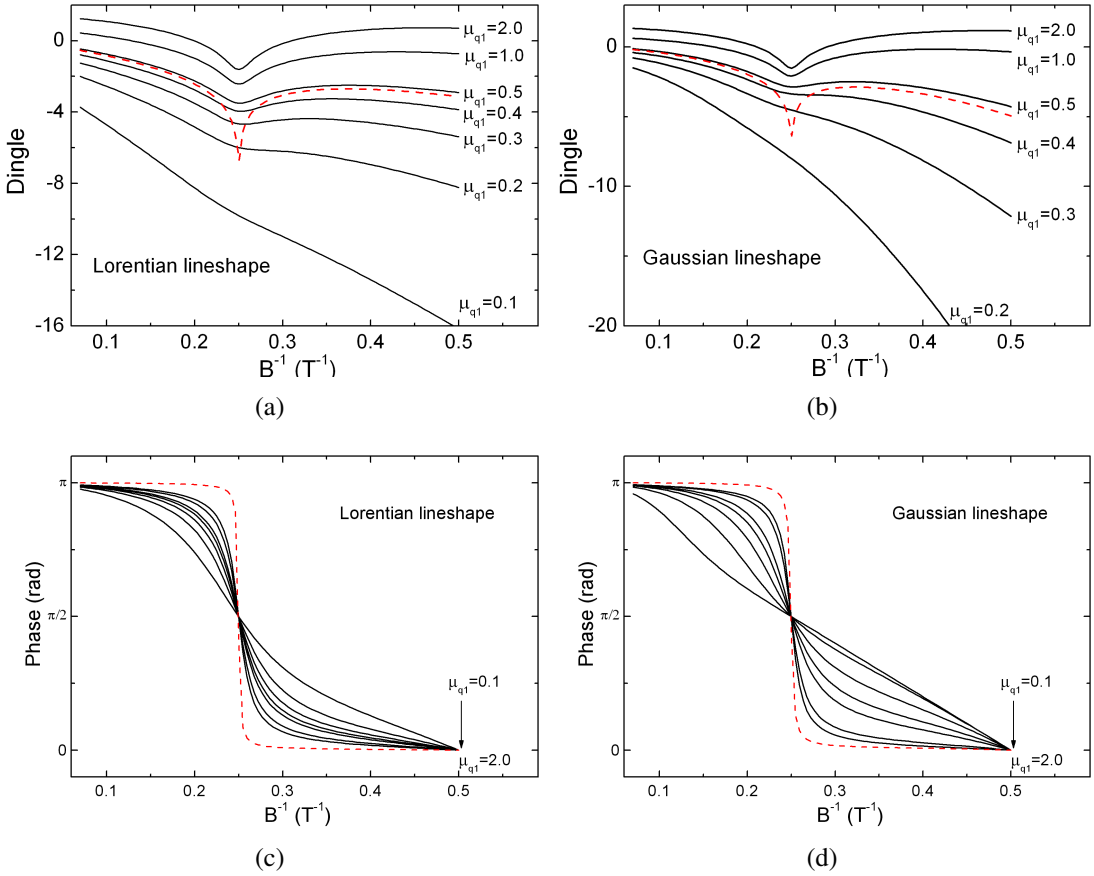

Fig. 4.9: Comparison of different Dingle plots and phase plots in the case of two channels for different quantum mobilities, for lorentzian and gaussian lineshape. Black, solid lines are calculated for two channels with $\mu_1/\mu_2 = 0.9$, and $f_1 = f_0 + \Delta f/2$, $f_2 = f_0 - \Delta f/2$, with f_0=200 T, Δf=2 T. The red, dashed lines are calculated for $\mu_1/\mu_2 = 0.99$ and μ_1 =0.5 m^2/Vs.

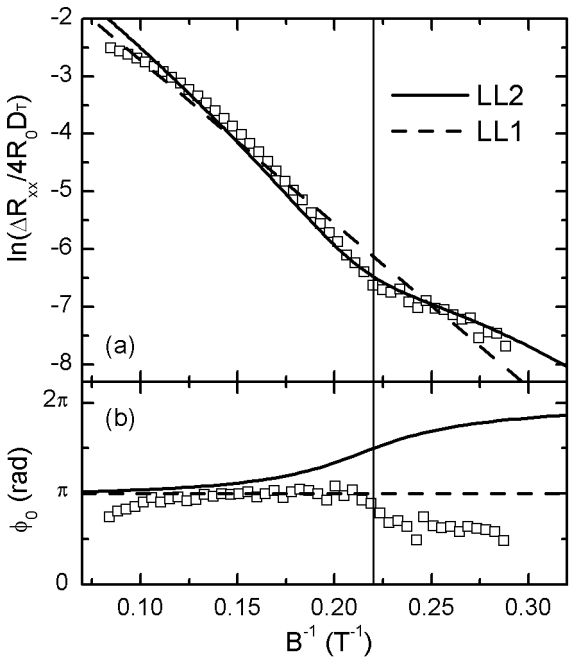

Fig. 4.10: (a) Dingle plot (squares) and data fits (lines) for device 1 obtained using models with lorentzian lineshape with one (LL1) and two channels (LL2). (b) Residual phase of the SdH oscillations (squares). The vertical line marks the change in the slope of the Dingle plot and in the phase.

In figure 4.10 is reported the result of the fitting procedure for the two-channels model in equation (4.14) to the Dingle plot for device 1 and the calculated residual phase. The fitting parameters are quantum mobilities $\mu_{1,2}^{(q)}$, the frequency difference Δf, the constant *const*. As a comparison, a fit with a single channel model is also shown.

The introduction of two conducting channels (LL2 model) leads to a curve which correctly reproduces the change of slope, but departs slightly from the data at small B^{-1}. Note that this discrepancy cannot be attributed to the condition $\mu_1^{(t)}/\mu_1^{(q)} = \mu_2^{(t)}/\mu_2^{(q)}$ which was imposed in the model. Attempts to fit the data without this constraint did not change the fits significantly. Fits of similar quality were obtained for the other devices.

The two-channels model also brings about the residual phase variation; however, it gives a phase increase, while the experimental phase decreases.

Gaussian lineshape The quality of the fits was substantially improved by introducing a gaussian lineshape (GL model), instead of the lorentzian one, for the density of states of the Landau levels.

The gaussian lineshape, to be inserted in equation (4.5), is given by [30, 38]

$$P_G(E) = \frac{1}{\sqrt{2\pi}\Gamma_G} \exp\left(-\frac{E^2}{2\Gamma_G^2}\right). \tag{4.15}$$

The procedure to obtain the resistivity is the same as reported before. For the single channel case, the oscillations amplitude modulation is

$$\Delta\rho = 4\rho_0 \exp\left(\frac{-2\pi^2\Gamma_G^2}{\hbar^2\omega_c^2}\right). \tag{4.16}$$

Depending on the scattering mechanism, the width Γ_G can or cannot be a function of the magnetic field. According to Coleridge [30], three length scales should be compared to choose the correct description. The first is the correlation length of the scattering potential Λ; the second is the cyclotron radius $R_{cycl} = \sqrt{2\pi\hbar^2 n_{2D}}/eB$; the third is the de Broglie length for electrons in a circular orbit in a magnetic field $\lambda_{dB} = 2\pi R_{cycl}/\nu$, where ν is the filling factor.

In the hypothesis $\Lambda \gg \lambda_{dB}$, the following cases are found:

- $R_{cycl} \gg \Lambda$: $\Gamma_G = \left(\hbar^2\omega_c/2\pi\tau_q\right)^{1/2} \propto B^{1/2}$; the Dingle plot is $\ln(\Delta\rho_{xx})/(4\rho_0 D_T(x)) = -(\pi/\mu_q)(1/B)$, thus it is linear (and identical to the lorentzian case)

- $R_{cycl} \ll \Lambda$: Γ_G is independent of B; the Dingle plot is

$$\ln\left(\frac{\Delta\rho_{xx}}{4\rho_0 D_T(x)}\right) = -\frac{\pi^2}{2\mu_q^2 B^2}, \tag{4.17}$$

  thus it is quadratic.

If $\Lambda \ll \lambda_{dB}$, the Dingle plot is again quadratic as in eq. (4.17).

In the regime $\Lambda \gg \lambda_{dB}$ the scattering potential can be considered, in the real space, to give a fluctuation, which sums to the conduction band; this can be treated semiclassically, neglecting the quantum confinement effects of these fluctuations. In the opposite condition, the quantum confinement is not negligible; the DOS has the same gaussian shape, but the width is independent of the magnetic field. In this regime, the transport can be described as occurring through a "network of channels", whose width is $\approx \Lambda$.

When a particular scattering model is chosen, the analysis of the transport properties allows an estimation of disorder parameters such as the correlation length. An example, applied to roughness scattering, is described in Appendix B.

A second gaussian-lineshape channel can be included in the Dingle plot using the same procedure which led to equation (4.14); the starting point is

$$\begin{aligned}\frac{\delta\rho_{xx}}{D_T} \propto & \sigma_1 \exp\left(-\frac{\pi^2}{2\mu_1^{(q)^2} B^2}\right)\cos\left(\frac{2\pi f_1}{B} + \pi\right) + \\ & + \sigma_2 \exp\left(-\frac{\pi^2}{2\mu_2^{(q)^2} B^2}\right)\cos\left(\frac{2\pi f_2}{B} + \pi\right),\end{aligned} \tag{4.18}$$

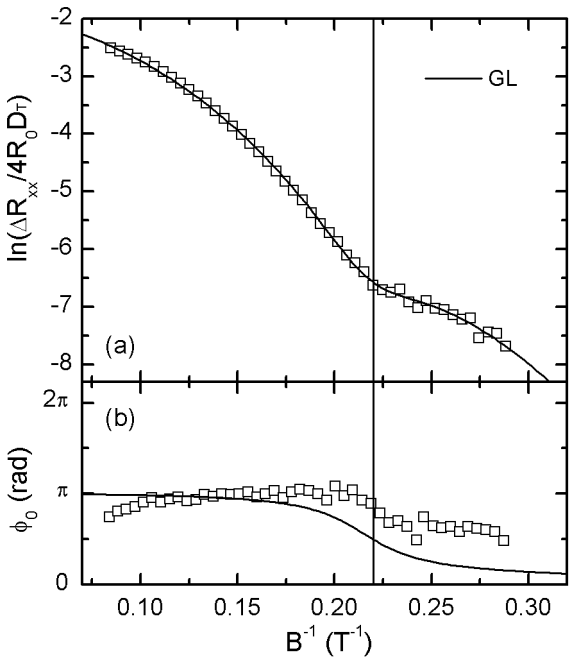

Fig. 4.11: (a) Dingle plot (squares) and data fit (line) for device 1 obtained using the model with gaussian lineshape with two channels (GL). (b) Residual phase of the SdH oscillations (squares) and calculated phase. The vertical line marks the change in the slope of the Dingle plot and in the phase.

which leads to

$$\ln\frac{\Delta\rho_{xx}}{D_T} = const - \frac{\pi^2}{2\mu_1^{(q)^2}B^2} + \frac{1}{2}\ln\left[1+ \right.$$
$$+\left(\frac{1-\Delta f/2f_0}{1+\Delta f/2f_0}\frac{\mu_2^{(t)}}{\mu_1^{(t)}}\right)^2\exp\left(-\frac{\pi^2}{\mu_2^{(q)^2}B^2}+\frac{\pi^2}{\mu_1^{(q)^2}B^2}\right)+ \tag{4.19}$$
$$\left.+2\left(\frac{1-\Delta f/2f_0}{1+\Delta f/2f_0}\frac{\mu_2^{(t)}}{\mu_1^{(t)}}\right)\exp\left(-\frac{\pi^2}{2\mu_2^{(q)^2}B^2}+\frac{\pi^2}{2\mu_1^{(q)^2}B^2}\right)\cos\left(\frac{2\pi\Delta f}{B}\right)\right].$$

Simulations of the Dingle plots calculated using this formula are shown in panels (b) and (d) of figure 4.9. Again, the minimum is suppressed for small mobility; in the gaussian lineshape case, this suppression occurs at higher mobility than the corresponding lorentzian case.

Figure 4.11 shows that the fit obtained using this equation (labelled GL) reproduces very well the data. Also, the calculated phase behaves as the experimental data.

This different behaviour of the phase is due to a quantitative difference in the parameters extracted from the fits with the lorentzian and the gaussian model. Indeed, in the GL model the channel with the higher carrier density is found to have the smaller mobility, while in the LL model the opposite occurs.

Density distribution The visible effect of the gaussian lineshape on the Dingle plot is the bending due to the quadratic dependence on B^{-1}. Another 2DEG feature possibly leading to this pattern is related to fluctuations of carrier density. In Refs. [63, 94] it is reported that such inhomogeneous density can heavily damp the SdH oscillations, alter the Dingle plot, and hinder a correct extraction of the quantum lifetime.

The simplest model for an inhomogeneous density is a gaussian distribution around an average value n_0 and standard deviation δn. In the analysis of the experimental data, the problem of calculating the Dingle plot for this case must be handled. The formulation can be generalised to every distribution; this general formula will be derived in the following, and then applied to the gaussian distribution.

The basic idea is to consider the "total oscillation" $SdH_t(B^{-1}, f_0)$ (i.e., the oscillation which is actually measured) as a sum of "partial oscillation" $SdH_p(B^{-1}, f)$, given by

$$SdH_p(B^{-1}, f) = -4D_T(x)\exp\left(-\frac{\pi}{\mu_q B}\right)\cos\left(\frac{2\pi f}{B} + \pi\right), \tag{4.20}$$

where a lorentzian lineshape is chosen for the Landau level.

The sum of the $SdH_p(B^{-1}, f)$ is weighted by a distribution function $g(f - f_0)$; here, f_0 is the average frequency. Since the distribution is possibly continuous, the sum is actually an integral:

$$SdH_t(B^{-1}, f_0) = \int_{-\infty}^{+\infty} df\, g(f - f_0) SdH_p(B^{-1}, f) = \left[g * SdH_p(B^{-1})\right](f_0), \tag{4.21}$$

where $*$ is the symbol for convolution.

It can be noted that, since the $SdH_p(B^{-1}, f)$ depends on f only through the cosine, a relation can be found with the Fourier transform of the distribution, i.e. its characteristic function. The expression for $SdH_t(B^{-1}, f_0)$ is then proportional the real part of the characteristic function $\tilde{g}$ of $g(f)$, multiplied by the thermal and lifetime damping factors (the mobility is assumed constant):

$$SdH_t(B^{-1}, f_0) = -4D_T(x)\exp\left(-\frac{\pi}{\mu_q B}\right)\mathrm{Real}\left[\tilde{g}(B, 2\pi f_0)\right], \tag{4.22}$$

where the minus sign comes from the π phase; the 2π factor depends on the definition of the characteristic function as Fourier transform. Note that this is still an application of the Poisson summation formula to the broadened density of states of the 2DEG in a magnetic field; again, only the first harmonic is retained.

In the case of a unit area gaussian distribution, with variance δf^2

$$g(f) = \frac{1}{\sqrt{2\pi}\delta f}\exp\left(\frac{-f^2}{2\delta f^2}\right) \tag{4.23}$$

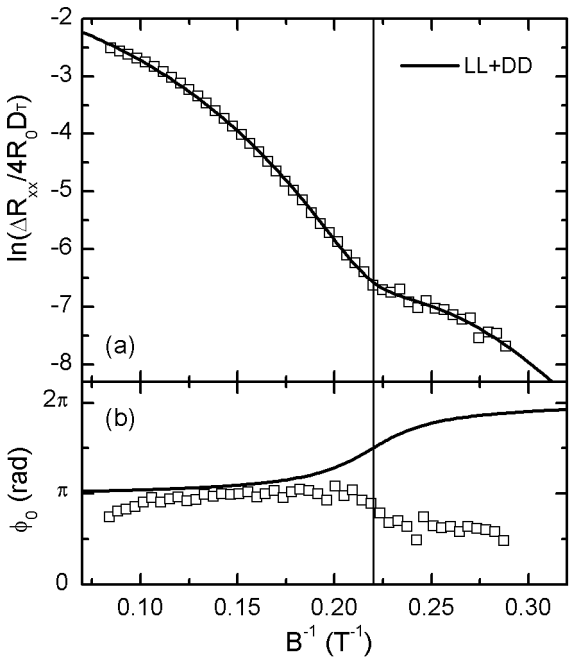

Fig. 4.12: (a) Dingle plot (squares) and data fit (line) for device 1 obtained using the model with lorentzian lineshape and gaussian density distribution with two channels (LL+DD). (b) Residual phase of the SdH oscillations (squares) and calculated phase. The vertical line marks the change in the slope of the Dingle plot and in the phase.

the total oscillation is

$$SdH_t(B^{-1}, f_0) = -4D_T(x)\exp\left(-\frac{\pi}{\mu_q B}\right)\exp\left(\frac{-2\pi^2\delta f^2}{B^2}\right)\cos\left(\frac{2\pi f}{B}+\pi\right), \tag{4.24}$$

and the Dingle plot acquires the quadratic term[4] $-2\pi^2\delta f^2/B^2$. The result can be extended to the two-channels case, assuming the same δf for both channels.

As shown in figure 4.12, a fit for the Dingle plot resulting from this model, with two channels with lorentzian lineshape for the Landau level and gaussian density distribution, can reproduce very well the data; indeed, the calculated curve would completely overlaps that of the GL model in figure 4.11a. However, the extracted values of the mobilities are similar to those from the LL2 model, and the phase behaviour is similar to that in figure 4.10b, i.e. it increases with increasing B^{-1}.

Magnetointersubband scattering Finally, another effect which gives an amplitude modulation was investigated: magnetointersubband scattering (MIS).

[4] It is worth noting that, if δf is small or if the investigated magnetic field range is narrow, a linear Dingle plot can occur also when a distribution is present. In this case, a 1st-order expansion in a neighbourhood of the central magnetic field $1/B_0$ gives $DinglePlot \simeq -2\pi^2\delta f^2/B_0^2 - (4\pi^2\delta f^2/B_0 + \pi/\mu_q)/B$. It can be seen, from this formula, that the density spreading can lead to an erroneous evaluation of μ_q. Of course, it is not simple to discriminate these situations from the SdH experimental data only.

When two subbands are occupied in a 2DEG, MIS gives two other oscillating terms that add to the magnetoresistance. The frequency of the first is given by the difference of those of the two subbands. Therefore, if the two subbands have similar carrier density, the MIS frequency is very small. If the second subband has a small carrier density, the MIS frequency is close to that of the first subband, and thus can give beatings similar to those expected for a spin-split configuration [28, 65, 85, 88]. The second frequency is the sum of those of the two subbands.

The MIS effect is an increased elastic intersubband scattering, which occurs when the two Landau levels ladders are alined. This condition is satisfied at magnetic fields given by [88]:

$$B_{l_1,l_2} = \frac{(E_1 - E_2)m}{\hbar e(l_1 - l_2)}, \tag{4.25}$$

$l_{1,2}$ being the Landau level indices for the two subbands. The expression for the resistivity becomes (assuming a lorentzian lineshape for the Landau levels):

$$\begin{aligned}\frac{\delta\rho_{xx}}{\rho_0} =& 2A_1 D_T(x)\exp\left(-\frac{\pi}{\mu_1 B}\right)\cos\left(\frac{2\pi f_1}{B}+\pi\right)+\\ &+2A_2 D_T(x)\exp\left(-\frac{\pi}{\mu_2 B}\right)\cos\left(\frac{2\pi f_2}{B}+\pi\right)+\\ &+2B_{12}\exp\left(-\frac{\pi}{\mu_1 B}-\frac{\pi}{\mu_2 B}\right)\cos\left(\frac{2\pi(f_1-f_2)}{B}\right)+\\ &+2B_{12}D_T(2x)\exp\left(-\frac{\pi}{\mu_1 B}-\frac{\pi}{\mu_2 B}\right)\cos\left[\frac{2\pi(f_1+f_2)}{B}\right].\end{aligned} \tag{4.26}$$

The coefficients A_1, A_2, B_{12} are related to intra- and inter- subband scattering probability. The first two terms are the standard SdH oscillations for the two subbands. The fourth term, proportional to $D_T(2x)$ is heavily damped with temperature, while the third, is not damped. At low temperature and high field, the approximation $D_T(x) \approx 1$ can be made, and the all the four terms should be retained. In figure 4.13 are shown the damping factors, at 0.25 K and 4.2 K. In the limit $B^{-1} \to 0$ the damping factor is 1, and, at the lowest temperature, both $D_T(x)$ and $D_T(2x)$ are very close to this limit (panel (b)); also at 4.2 K, the factors are always larger than 0.9 down to 1 T^{-1}.

The case $n_2 \ll n_1$ ($f_2 \ll f_1$) is interesting because can give a beatings pattern similar to that expected for two spin-split subbands. In this case, the oscillation with frequency f_2 yields a slowly varying background. If the thermal damping factor are neglected, a pseudo Dingle plot can be constructed for the oscillations including MIS:

$$\ln\left(\frac{\Delta\rho_{xx}}{\rho_0}\right) = const - \frac{\pi}{\mu_1 B} + \ln\left[1 - \frac{B_{12}}{A_1}\left(-\frac{\pi}{\mu_2 B}\right)\cos\left(\frac{2\pi f_2}{B}\right)\right]. \tag{4.27}$$

This formula is valid in the case of lorentzian lineshape for the Landau levels. The gaussian

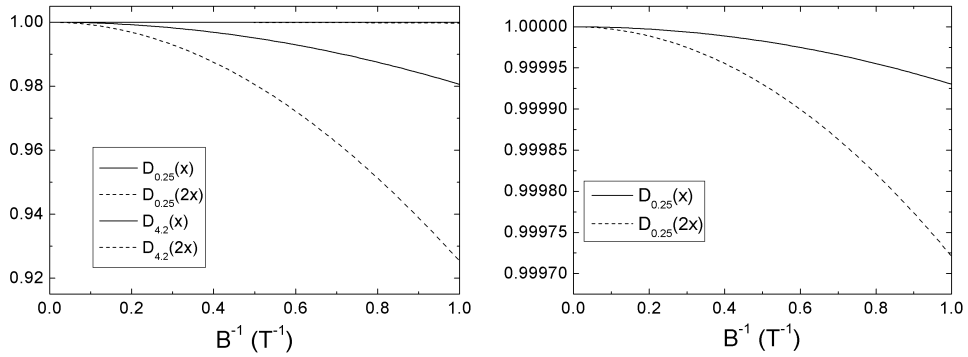

Fig. 4.13: (a) Comparison of damping factors $D_T(x)$ and $D_T(2x)$ at T=0.25 K and 4.2 K.(b) Detail of the T=0.25 K case.

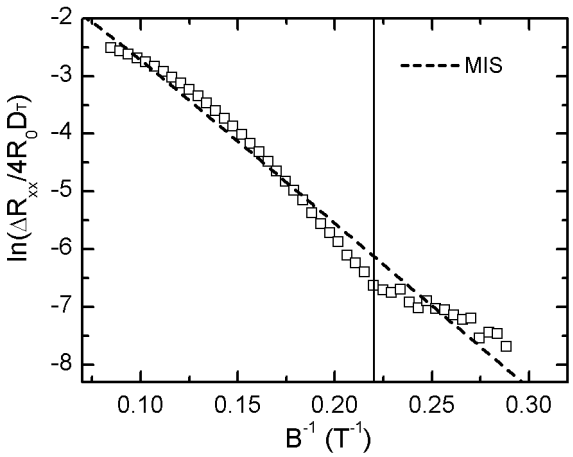

Fig. 4.14: Dingle plot (squares) and data fit (line) for device 1 obtained using the MIS model.

lineshape can be taken into account by suitably substituting the damping factors proportional to B with those proportional to B^2, as in equation (4.17). The density distribution effect can be added as described above.

An attempt to fit with the magnetointersubband scattering model is shown in figure 4.14, including a lorentzian lineshape; the second subband would have a density of $5.4{\cdot}10^{14}$ m^{-2}, 200 times smaller than the first.

The results are not as good as for the other models, and introduction of a density distribution or gaussian lineshape does not give a better result. The MIS hypothesis is thus discarded.

In summary, a model with two channels and a gaussian lineshape for the Landau levels well reproduces the experimental data for device 1; the same results are found for device 3 and 4. The result of the fits of this model are reported in table 4.2 and discussed in section 4.2.4. Other possible mechanisms which could explain the experimental amplitude and phase modulation, namely a bending and a change of slope in the Dingle plot and a variation in the residual phase,

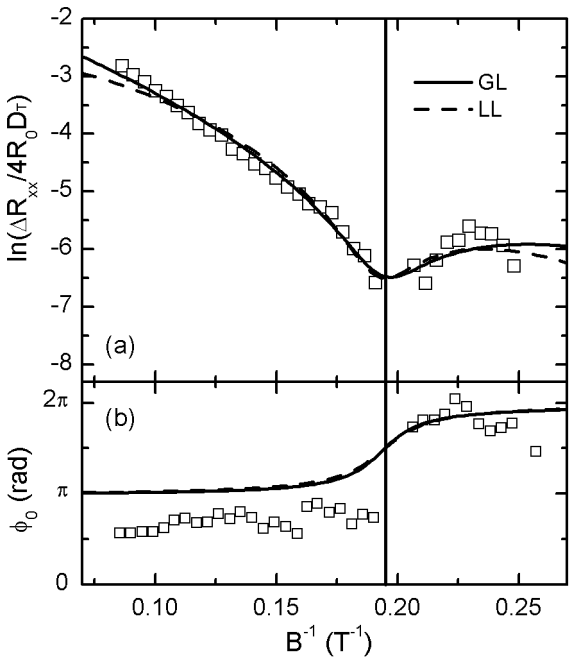

Fig. 4.15: (a) Dingle plot (squares) and data fits (lines) for device 2 obtained using the models discussed in the text. (b) Residual phase of the SdH oscillations (squares); lines are the phase calculated with the LL (dash-dot) and GL (continuous) models. The vertical line marks the position of the node in the slope of the Dingle plot and in the phase.

are excluded because they cannot reproduce these features.

Dingle plot for device 2 In figure 4.15 the Dingle plot and the residual phase are reported for device 2. This device exhibits a different behaviour with respect to the other three investigated devices. First, it shows in the SdH curve a clear beating, which suggests the presence of a two channels. Second, the residual phase has a variation at a position corresponding to the node of the beatings, but this variation is an increase of the phase, while the other devices have a decrease (see figure 4.8b).

The fit with two channels and gaussian and lorentzian lineshape for the Landau levels are also shown in figure 4.15a. The Dingle plot fit well reproduces the data; the residual phase is reproduced qualitatively, as in device 1.

In conclusion, the analysis of the Shubnikov–deHaas data with two-channels models can satisfactorily explain the data.

4.2.3.3 Measurements at 4.2 K

The magnetotransport properties have been also measured at liquid helium temperature, i.e. 4.2 K, for devices 1 and 3. SdH oscillations can still be observed at this temperature, and are reported in figure 4.16.

Well developed SdH oscillations are observed to start at a higher field than in the lowest tem-

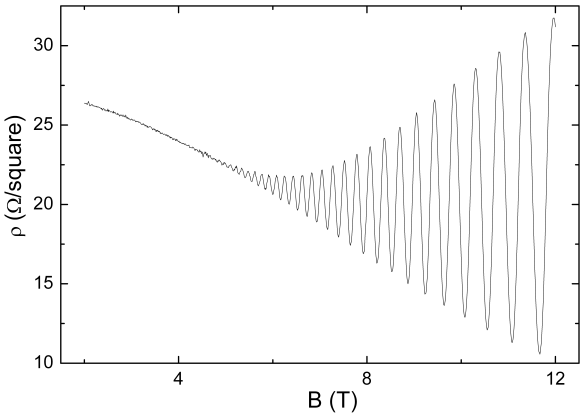

Fig. 4.16: Longitudinal resistivity as a function of magnetic field for device 1 at 4.2 K.

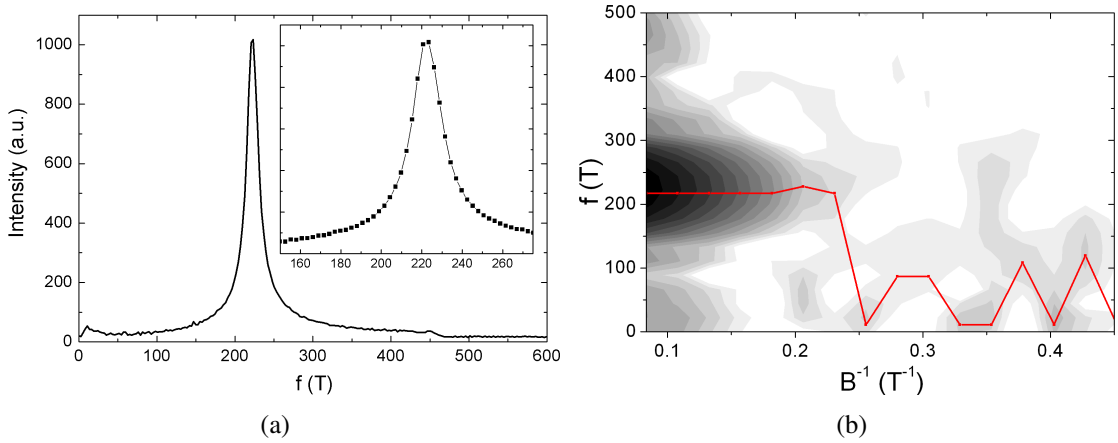

(a) (b)

Fig. 4.17: (a) FFT and (b) spectrogram of the SdH data for device 1 at 4.2 K. The line marks the position of the maximum in the FFT as a function of the inverse magnetic field. Darker regions have the highest spectrum amplitude.

perature acquisitions, because of thermal damping. This can be clearly seen in the spectrogram (figure 4.17b): the oscillation ends at about 0.22 T^{-1}.

The Hall effect and the FFT analysis of the SdH oscillations show that the carrier density and the mobility have the same values (within 1%) as the 0.25 K values.

The reduced magnetic field range where the oscillations are visible impedes the observation of a change of slope in the Dingle plot or a phase variation as at 0.25 K.

Figure 4.18 reports the Dingle plot and the residual phase for device 1, a vertical line marks the expected position for the node, if this position is assumed to be the same as at 0.25 K (i.e., the frequency difference is assumed to be independent of temperature); note that this position is beyond the limit of the experimental data. In this range, we can see that the Dingle plot has a bending, but not the change of slope. The residual phase is also nearly constant.

To give an estimate of the quantum mobility at this temperature, we can assume that the gaussian lineshape is still suitable for the data. In figure 4.18 the result of this procedure is shown for device 1, together with the experimental data. Table 4.1 reports the numerical values

	Ch.	f T	$\mu^{(q)}$ m^2/Vs	$\mu^{(t)}$ m^2/Vs	τ_q ps	τ_t ps	$\mu^{(t)}/\mu^{(q)}$
Device 1	1	223.2	0.23	2.11	0.29	2.63	9.1
	2	220.9	0.25	2.29	0.33	2.86	
Device 3	1	218.2	0.24	1.97	0.31	2.46	8.1
	2	215.8	0.26	2.12	0.33	2.65	

Tab. 4.1: Extracted parameters for two-channels, gaussian lineshape model of SdH amplitude modulation at 4.2 K; channels labelled as "1" have the largest carrier density.

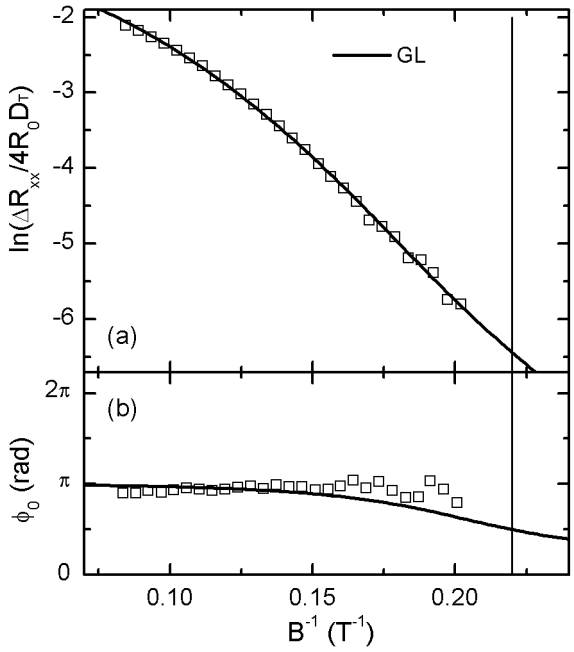

Fig. 4.18: (a) Dingle plot (squares) and data fits (lines) for device 1 at 4.2 K, obtained using the GL model. (b) Residual phase of the SdH oscillations (squares); the line is the phase calculated with the GL models. The vertical line marks the position expected for a node.

of the parameters extracted from the two devices. The model can again reproduce the data very well.

4.2.4 Discussion

Finally, I will discuss in details the results from the measurements at 0.25 K.

In table 4.2 the resulting parameters for the four devices are reported. In this table, the transport mobilities are evaluated from the quantum mobilities and the ratio $S = \mu^{(t)}/\mu^{(q)}$. This ratio was calculated by comparison of the Hall mobility μ_H and the quantum mobility. The effective Hall mobility in the case of two channels, when $\mu_{1,2}B \ll 1$, or, as in our case, when

	Ch.	Δf T	f T	$\mu^{(q)}$ m^2/Vs	$\mu^{(t)}$ m^2/Vs	τ_q ps	τ_t ps	$\mu^{(t)}/\mu^{(q)}$
Dev. 1	1	2.2	222.9	0.27	2.15	0.34	2.69	7.9
	2		220.7	0.29	2.27	0.36	2.83	
Dev. 2	1	2.6	219.5	0.34	2.41	0.43	3.01	7.0
	2		216.9	0.33	2.30	0.41	2.88	
Dev. 3	1	2.5	217.2	0.29	2.04	0.36	2.55	7.1
	2		214.7	0.30	2.12	0.37	2.65	
Dev. 4	1	2.2	223.7	0.27	2.11	0.34	2.63	7.7
	2		221.5	0.29	2.23	0.36	2.79	
Ave.	1	2.4 ± 0.2		0.29 ±0.03	2.17 ±0.16	0.36 ±0.04	2.72 ±0.20	7.4 ±0.4
	2			0.30 ±0.02	2.23 ±0.08	0.38 ±0.02	2.79 ±0.10	

Tab. 4.2: Extracted parameters for two-channels, gaussian lineshape model of SdH amplitude modulation at 0.25 K; channels labelled as "1" have the largest carrier density.

$\mu_1 \approx \mu_2$, is given by

$$\mu_H = \frac{n_1\mu_1^2 + n_2\mu_2^2}{n_1\mu_1 + n_2\mu_2} = \frac{f_1\mu_1^2 + f_2\mu_2^2}{f_1\mu_1 + f_2\mu_2} \tag{4.28}$$

The linear dependence of both numerator and denominator on the densities $n_{1,2}$ allows the substitution of them with the frequencies $f_{1,2}$, without inserting the spin degeneracy factor; hence, this relation is independent of the spin degeneracy. In this formula $\mu_{1,2}$ are the transport mobilities. The ratio S is thus found simply inserting $\mu_{1,2} = S\mu_{1,2}^{(q)}$.

From the investigation of amplitude and phase modulation, it is possible to assert the presence of the two components in the SdH oscillations. In principle, they can originate from spin splitting, but also from the occupation of two subbands in the 2DEG, from parallel parasitic channels or from carrier density inhomogeneities. We discuss in the following these possible different origins.

The presence of two conducting channels with almost equal oscillation frequency, i.e. with almost equal charge density ($n_1 \approx n_2$), such as those found by the previous analysis, strongly support the lifting of the spin degeneracy, since $n_1 + n_2 \approx 2n_1$ must be equal to the total carrier density n_H obtained from the classical Hall effect. Indeed, assuming spin degeneracy the total carrier density would be twice the experimental n_H.

Moreover, the intersubband energy separation extracted from the measurement would be of the order of 1 meV; simulations of the coupled Schrödinger–Poisson equations [95] yield, for this separation, a value in the range from 150 to 200 meV, thus much larger; also, experimental separations reported for GaN-based 2DEG are much larger than 1 meV (for example, in Ref. [114] is reported a value of 77 meV).

We can, therefore, rule out the hypotheses of the occupation of two subbands and the presence of a parasitic channel parallel to the 2DEG [93].

Another possibility is that fluctuations of geometrical parameters (e.g. well thickness) give rise to the presence of two macroscopic regions having different carrier density, and thus to beatings [16]. We believe that this effect is highly unlikely in our case. First of all, the fluctuations should be such as to produce identical regions in four devices differing in size, gate presence and geometry. Furthermore, we notice that a diffuse inhomogeneity in the heterostructure may give rise to a carrier density distribution; in this case, a bending in the Dingle plot is expected, without beatings.

We conclude that the two conducting channels in the heterostructure can be identified as spin-split subbands. The formula $\Delta E = e\hbar\Delta f/m$ allows the evaluation of the spin-splitting energy and of the Rashba coefficient $\alpha = \Delta E/2k_F$. Taking the average values from table 4.2, the extracted values are $\Delta E = 1.2 \pm 0.1$ meV and $\alpha = 0.76 \pm 0.06 \cdot 10^{-12}$ eVm.

As for the small difference of mobility found for the two channels, an asymmetry in the spin-flip relaxation [45] can explain it.

Finally, we discuss the gaussian lineshape model, which well describes the Dingle plot of the investigated devices. Gaussian lineshape describes the density of states of Landau levels when the correlation length of the disorder scattering potential is smaller than the de Broglie length. To check this condition, the correlation length was calculated assuming that the dominant scattering mechanism is due to roughness scattering, as in Ref. [23]; the model is described in Appendix B. With this model, a correlation length of 5.4 nm is estimated, while the de Broglie length is 15 nm: the condition for the validity of the gaussian lineshape is fulfilled.

Referring to the 4.2 K data, we note that the assumption that was made in the previous section, that the frequency difference is independent on temperature, is reasonable when the two channels are attributed to spin-splitting. The comparison with the results obtained at 4.2 K (reported in table 4.1) shows that the quantum mobility is slightly reduced in comparison with the 0.25 K value, while the transport mobility is closer.

Concluding this section, I remind that, besides Shubnikov–deHaas effect, also the weak antilocalisation effect is directly affected by the spin-orbit interaction.

This effect was investigated, but the quality of the experimental data is not sufficient to draw firm conclusions. This result will be discussed in section 4.3.4, after the discussion of the results from sample B, which instead exhibited a clear weak antilocalisation signal.

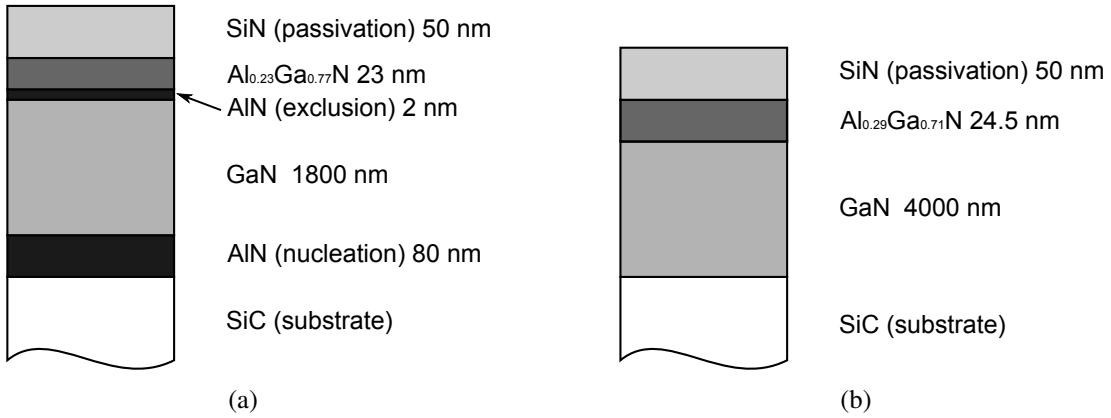

Fig. 4.19: Layers sequence for Sample A and B.

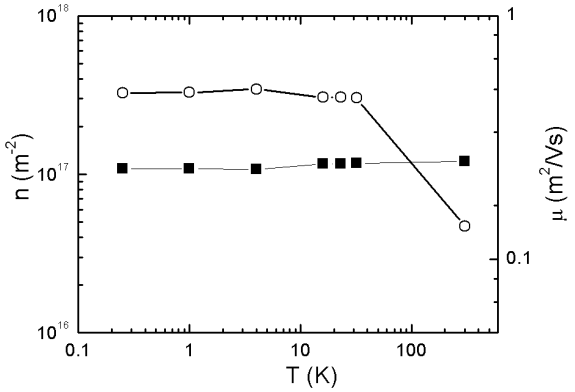

Fig. 4.20: 2DEG carrier density (open symbols) and mobility (full symbols) as a function of temperature as obtained from classical Hall effect measurement in Sample B. Lines are guides for eyes.

4.3 Sample B

Sample B is an $Al_xGa_{1-x}N$/GaN heterostructure, grown on a SiC substrate (see figure 4.19b). The Gan layer has a thickness of 4 μm, and the barrier of $Al_{0.29}Ga_{0.71}N$ is 24.5 nm thick. The heterostructure was passivated with a 50 nm-thick SiN layer grown by plasma enhanced CVD.

The properties of the 2DEG were investigated in 100×200 μm^2 Hall bar devices.

4.3.1 Classical magnetotransport characterisation

Classical Hall effect measurements at low fixed magnetic field show (figure 4.20) that the carrier density is constant at the lowest temperature at $1.08 \cdot 10^{17}$ m^{-2}, and has a small increase at high temperature to about $1.10 \cdot 10^{17}$ m^{-2}; the mobility at room temperature is 0.13 m^2/Vs and rises to 0.48 m^2/Vs at the lowest temperature.

Following the same procedure as in the Sample A, the Drude magnetoresistance has been investigated at 0.25 K to check if the transport occurs through a single channel; the two experimental RCT components are reported in figure 4.21. A single channel model well reproduces the data, with an evaluated mobility of 0.48 m^2/Vs, in agreement with fixed field measurements.

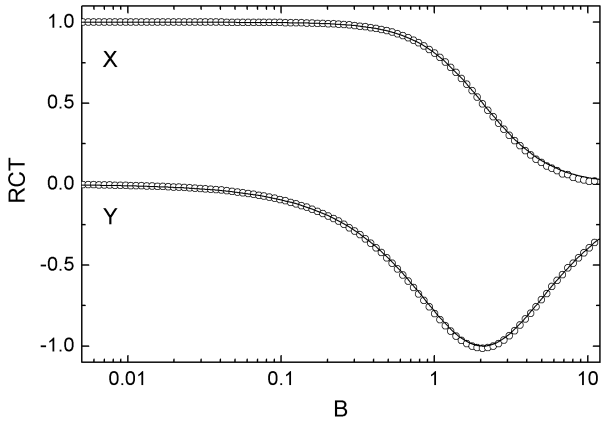

Fig. 4.21: Components X and Y (circles) of the reduced conductivity tensor as a function of magnetic field for Sample B, measured at T=0.25 K and least-square fits of data (continuous lines) obtained in the hypothesis of only one conducting channel in the sample. The number of experimental points shown in the graph is reduced (for representation purpose only) with respect to the acquired points, with a ratio of 1:40.

Again, the data are also compatible with a two-channels model, provided that the channels have similar conductivity and the mobilities differ less than 10%.

The value of n was verified also with the slope of the transverse resistivity using the relation $\rho_{xy} = B/en$, valid for the single channel system. These two measurements allow the determination of μ and n independently of the zero-field value, which can be affected by low field quantum correction.

At the lowest temperature Shubnikov–deHaas effect and, at very low field, weak antilocalisation can be observed in this sample. These features are investigated in the following sections.

4.3.2 Shubnikov–deHaas effect

In the discussion of the results of sample A the Shubnikov–deHaas effect has proved to be an effective method for the determination of spin-splitting in 2DEGs. Therefore, sample B was first of all investigated with this method.

Figure 4.22 reports the magnetoresistivity curve up to 12 T taken at 0.25 K. The oscillations are observable for fields higher than 4 T. Clear signatures of a beating pattern are not visible in this experimental curve.

The frequency of the oscillation was investigated through standard FFT of the data taken as a function of the inverse magnetic field, using a rectangular window. The data were acquired in equal spacing in B, and were interpolated (before the transformation) to have equal spacing in B^{-1}; the points in the interpolation are close to the actual experimental points. The background was subtracted from the curve. The FFT is shown in figure 4.23a.

A single peak at frequency $f = 225.5$ T is found. The corresponding carrier density, assuming spin degeneracy, is $n = 1.09 \cdot 10^{17}$ m^{-2}, in excellent agreement with the determination of

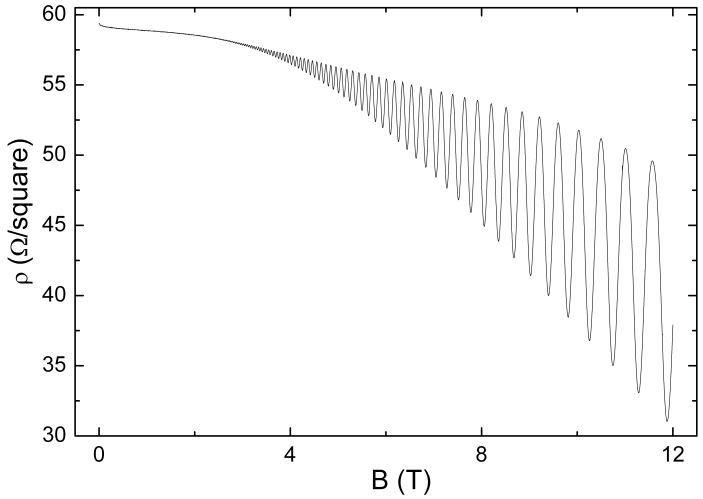

Fig. 4.22: Longitudinal resistivity as a function of magnetic field in Sample B.

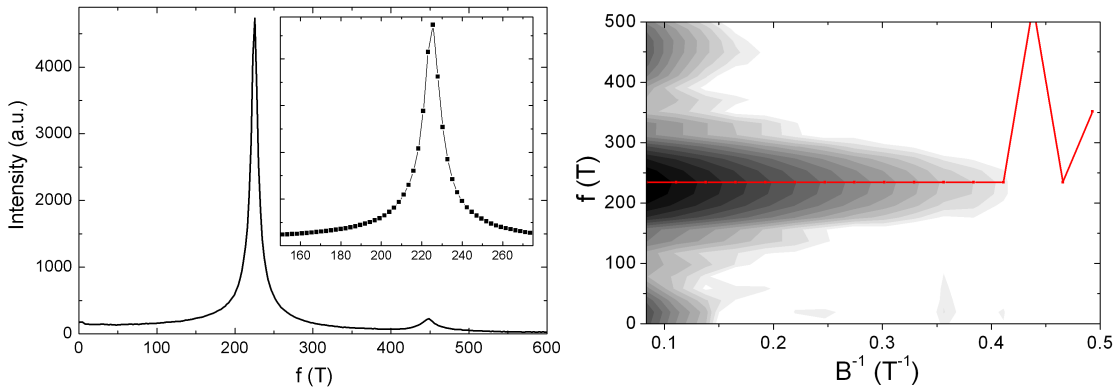

(a) (b)

Fig. 4.23: (a) Fast Fourier Transform spectrum of the magnetoresistivity of sample B. Inset is a detail of the main peak. (b) Spectrogram of the SdH data for sample B. The line marks the position of the maximum in the FFT as a function of the inverse magnetic field.

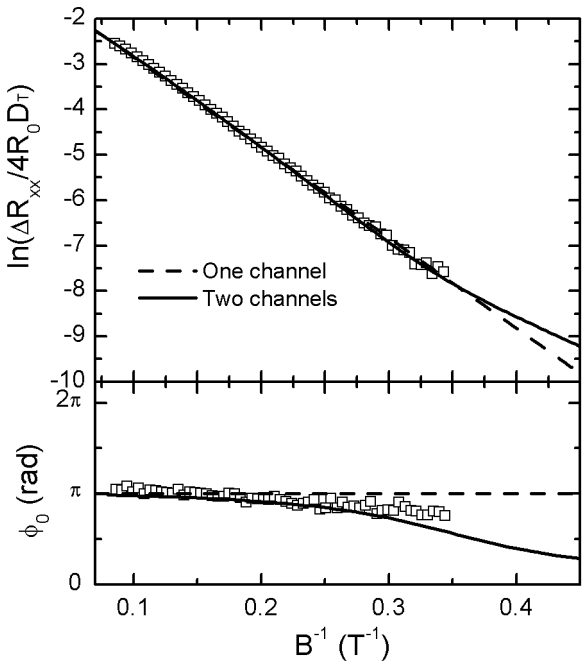

Fig. 4.24: Dingle plot (upper panel) and residual phase (lower panel) as a function of the inverse of magnetic field for Sample B. The dashed line is a fit with a one-channel model, the continuous line is a two-channels model fit with the assumption of ΔE =0.77 meV.

the classical Hall effect. The spectrogram of these data (figure 4.23b) reveals that oscillations with this frequency can be found down to a field of 2.5 T. It also verifies that the peak frequency remains constant.

No evidence of spin-split channels is present in the data and in the FFT analysis, although we have verified that both raw data and FFT analysis could be compatible with the presence of two conducting channels, provided that their energy splitting is smaller than 0.8 meV. However, as will be discussed in detail in section 4.3.3, in this sample a clear antilocalisation peak, relating to the spin-orbit effect, was detected. Furthermore, by considering the layer characteristics of the sample and of the resulting 2DEG, it was expected that a spin-orbit effect similar in magnitude to that of sample A should be present. To shed light into this apparent contradiction we have proceeded to the analysis of the SdH data with the more refined scrutiny of amplitude and phase modulation in the Dingle plot.

The amplitude modulation is reported in figure 4.24a; phase modulation is in figure 4.24b.

It is apparent that the amplitude is linear in the whole range, while the phase deviates slightly from the π rad value at higher B^{-1} values.

In the figures, along with a fit with the single channel model, the result of a fit with a two-channels model with lorentzian lineshape are also reported, assuming a spin-splitting energy of 0.77 meV, which would correspond to a node at the end of the observed oscillations. Both models satisfactorily reproduce the data.

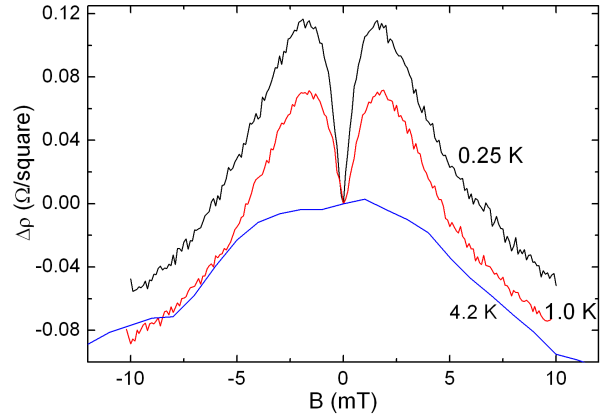

(a)

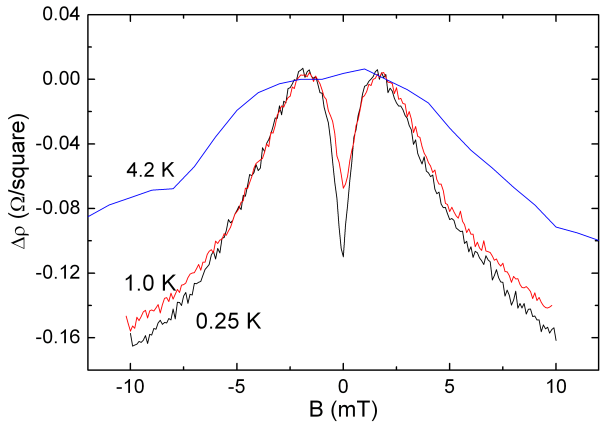

(b)

Fig. 4.25: Experimental magnetoresistivity of Sample B at very low fields, at 0.25 K, 1 K and 4.2 K. (a) $\Delta\rho = \rho_{xx}(B) - \rho_{xx}(0)$, (b) $\Delta\rho = \rho_{xx}(B) - \rho_{xx}(1.8\ \mathrm{mT})$.

In conclusion, all the analyses of the SdH oscillations are compatible with the presence of two conductive channels, whose energy separation can not exceed 0.77 meV, although they do not provide any definite evidence for it.

4.3.3 Weak antilocalisation

In this sample magnetotransport measurements at very low magnetic fields have shown a clear signature of the weak antilocalisation effect at low temperature (0.25 K and 1 K). Figure 4.25 shows the measured magnetoresistivity as a function of magnetic field in the range from −10 to 10 mT at 0.25 K, 1 K and 4.2 K. We can see in the 0.25 K and 1 K curves a local minimum at zero field and two symmetric maxima at about +2 and −2 mT. The height of the maxima is smaller at 1 K; the field value corresponding to the maxima is independent of the temperature. At higher fields the two curves are parallel. At liquid helium temperature (4.2 K) only the weak localisation is visible.

To acquire these curves a lock-in technique at constant current was employed. To reduce

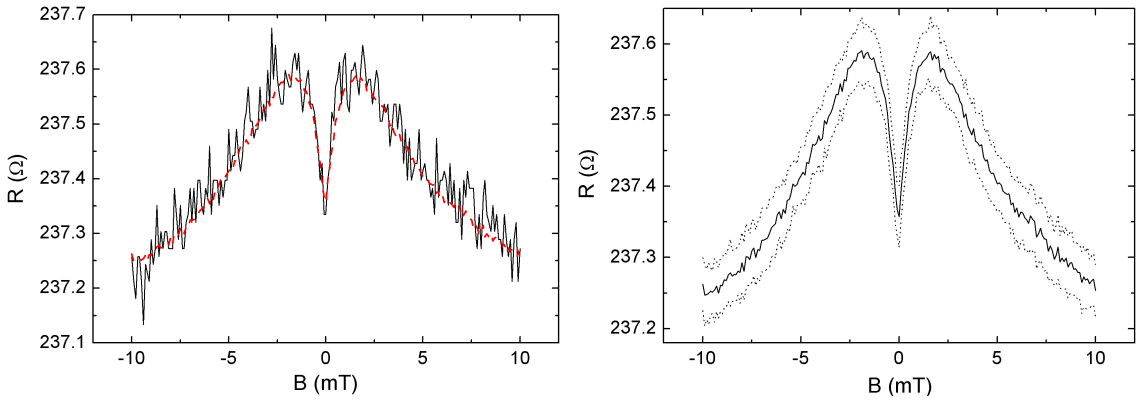

Fig. 4.26: (a) Comparison of a single magnetoresistivity trace (red, dashed line) and the average of 80 traces (solid line). (b) Average curve (solid line) with the 1-standard deviation band (marked by dotted lines).

the noise in the measurements, several curves were acquired as a function of magnetic field and then averaged. Figure 4.26a compares the average curve and a single experimental curve for the 0.25 K measurement; figure 4.26b shows the average and the standard deviation band at 0.25 K; the 1 K case is similar. The standard deviation obtained from this procedure was taken into account as weighting factor in the least-square fitting of the data.

The average resistivity curve was converted to conductivity as $\sigma_{xx} = \rho_{xx}/(\rho_{xx}^2 + \rho_{xy}^2)$; since the transverse component ρ_{xy} was simultaneously acquired, this procedure does not need any further assumptions. Then, an offset in the magnetic field (about 5.0 mT) was corrected; this correction is justified since the longitudinal resistivity must be an even function of magnetic field. Then, the classical Drude contribution to the conductivity is subtracted from the data; in this low field range the magnetoconductance is very small, and the subtracted Drude conductivity amounts to a constant.

The output of this procedure can be directly compared with the models described in section 3.3.1. However, in the fitting procedure an additive constant is left as a free parameter to account for experimental errors and other effects which can contribute as a conductivity constant, such as electron-electron interaction. Indeed, this constant, as extracted from the fit, is of the order of 0.1% of the zero-field conductivity, and is of the same order of the electron-electron interaction correction, calculated according to Ref. [23] (this interaction is further discussed in appendix C.1); note, however, that a systematic error in the measured current of less than 1% can give the same correction. Finally, the data are symmetrised, i.e. they are transformed as

$$\sigma_{symm}(B) = \frac{\sigma(-B) + \sigma(+B)}{2}. \tag{4.29}$$

This procedure removes residual asymmetries in the four wire measurements [105]. As seen in the previous figures, the experimental data are already symmetric, so that the symmetrisation

has a little effect.

4.3.3.1 Models used for the analysis of the weak antilocalisation signal

To extract the physical parameters from the data, a suitable theoretical formula is required.

A number of models have been developed to describe quantitatively the weak antilocalisation. As summarised in section 3.3.1, some of them are valid only within the diffusion approximation, i.e, in small magnetic field and for small spin-orbit; furthermore, they assume a different picture of the spin-orbit effect. In this section, four of these models will be described and compared through least-square fit to the experimental data; indeed, among the models described, only two are usually considered in the literature to fit the experimental data, the "diffusive" model and the "Golub" model. Thus, it is interesting to compare them and discuss their validity.

I recall that the weak antilocalisation correction arises from interference of time-reversed trajectories, when the interference is strongly affected by the spin part of the wavefunction because of spin-orbit interaction. The amplitude of the interference is called Cooperon, and is calculated using the Green function technique and diagrammatic expansions.

I recall also that, since in the wurtzite lattice the spin-orbit interaction has the Rashba form (section 2.2), only this kind of interaction will be considered; the Rashba coefficient α will be actually an effective coefficient, given by $\alpha = \alpha_{BR} + \alpha_{WSIA} - (\gamma_{wz} + \gamma_{bands})\left(b\langle k_z^2\rangle - k_{||}^2\right)$.

Diffusive model When the magnetic length $l_B = \sqrt{\hbar/2eB}$ is longer than the mean free path $l = v_F\tau$, the trajectories contributing to the quantum correction involve many collisions. In this limit the diffusion approximation is valid. In the magnetic field scale, the condition corresponds to $B < B_{tr}$, $B_{tr} = \hbar/2el^2$ being the so-called transport field.

In Sample B, $B_{tr} = 4.8$ mT, and the investigated magnetic field range reaches 10 mT. Thus, a diffusive model could not fit the data in the whole range. However, the main feature of these data is the minimum at about 2 mT, which is below the transport field; then, a diffusive model could reproduce it, or at least give an estimation of the parameters. Hence, a first tentative fit can be done in this approximation.

In particular, Punnoose [84] provided a closed-form formula for the weak antilocalisation. This allows a simple use of it, while the other models, described in the following, require a careful numerical evaluation.

This model is based on the theory of Iordanskii, Lyanda-Geller and Pikus (ILP) [56], in the particular case of a spin-orbit interaction given in the form of a Rashba interaction (see equation (2.5)), i.e. $H = \alpha\boldsymbol{\sigma} \times \mathbf{k}$. It is then suitable for the case of GaN.

The Hamiltonian of the system can be rewritten as $H \propto (\mathbf{k} - 2e\mathbf{A}_S)^2$ (see also equation (3.33), page 43), so that the spin-orbit effect can be interpreted as a spin-dependent Aharonov–Bohm (AB) effect.

The Cooperon in this case is proportional to the Green function of the operator

$$\mathcal{H} = D\left(-i\boldsymbol{\nabla} - \frac{2e}{\hbar}\mathbf{A} - \frac{2m\alpha}{\hbar}\boldsymbol{\Sigma}\right)^2 + \frac{1}{\tau_\varphi}. \tag{4.30}$$

Here, D is the diffusion coefficient, $\boldsymbol{\Sigma}$ contains the total spin of the interfering waves as $\boldsymbol{\Sigma} = \frac{1}{2}\hat{z} \times (\boldsymbol{\sigma}_1 + \boldsymbol{\sigma}_2)$, and the term $1/\tau_\varphi$ describes the phase relaxation.

From this starting point, the conductance correction, as a function of the magnetic field, is

$$\begin{aligned}\Delta\sigma(B) =& \frac{e^2}{2\pi h}\left\{\left[\sum_{s=0,\pm1} u_s \psi\left(\frac{1}{2} + \beta_\varphi - v_s\right)\right] - \right. \\ & \left. -\psi\left(\frac{1}{2} + \beta_\varphi\right) + \frac{1}{(b_{so} + \beta_\varphi)^2 - 1/4} - 2\ln\beta_\varphi\right\},\end{aligned} \tag{4.31}$$

where

$$v_s = 2\delta\cos\left[\theta - \frac{2\pi}{3}(1-s)\right], \tag{4.32a}$$

$$u_s = \frac{3v_s^2 + 4\beta_{so}v_s + (5\beta_{so}^2 + 4\beta_{so}\beta_\varphi - 1)}{\prod_{s'\neq s}(v_s - v_{s'})}, \tag{4.32b}$$

$$\delta = \sqrt{\frac{1 - 4\beta_{so}\beta_\varphi - \beta_{so}^2}{3}}, \tag{4.32c}$$

$$\theta = \frac{1}{3}\arccos\left[-\left(\frac{\beta_{so}}{\delta}\right)^3\left(1 + \frac{2\beta_\varphi}{\beta_{so}}\right)\right], \tag{4.32d}$$

where $\beta_{so} = B_{so}/B$, $\beta_\varphi = B_\varphi/B$ and $\psi(x)$ is the digamma function.

The field B_{so} is related to the parameter α by

$$B_{so} = \frac{m^2}{e\hbar^3}\alpha^2, \tag{4.33}$$

and the energy splitting is $\Delta E = 2\alpha k_F$.

The phase field is defined as

$$B_\varphi = \frac{\hbar}{4eD\tau_\varphi}. \tag{4.34}$$

The model was fitted to the data using only the magnetic field range with $B < B_{tr}$. The result is shown in figure 4.27 for 0.25 K and 1 K; the extracted values are reported in table 4.3. We can see that the model can well reproduce the data in this range. Attempts to fit in the full range (not shown) did not give any better results. The model reproduces the data in its range of validity, but fails, as expected, outside it.

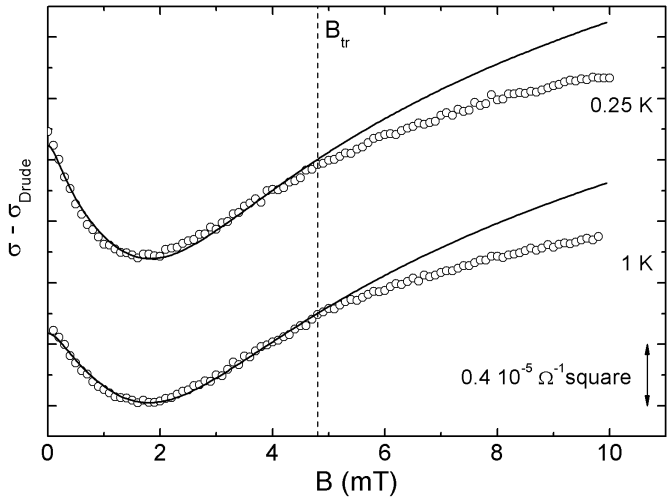

Fig. 4.27: Experimental symmetrised magnetoconductivity (symbols) and fit (lines) with the diffusive model for 0.25 and 1 K. The vertical line marks the transport field B_{tr}.

Zduniak model To verify if the ballistic models can improve the fits, or can give significantly different values of the parameters, I tried first to fit the data with the model by Zduniak *et al.* [113].

This model includes spin-orbit interaction as a spin relaxation effect, i.e. as an additive coherence relaxation rate. Previously, the same procedure was followed by Hikami *et al.* [55] and Kawabata [59]. The Hikami model is valid only in the diffusive regime, and indeed the Zduniak model reduced to it in this limit. As for the Kawabata model, the Zduniak model is a reformulation of it.

To calculate the Cooperon, the authors consider the probability of an electron to return in the origin after n scattering events; then, all these contributions are summed. Terms with $n = 1, 2$ are not summed, since the effect of the magnetic field depends on the flux through the area enclosed by the path, and these paths have zero area. The return probability is calculated following Kawabata [59].

The Cooperon $C(x, z)$ is given by

$$C(b,z) = x \sum_{N=0}^{\infty} \frac{P_N^3(b,z)}{1 - P_N(b,z)}, \tag{4.35a}$$

$$P_N(b,z) = \sqrt{\frac{2}{|b|}} \int_0^{\infty} \exp\left(-\sqrt{\frac{2}{|b|}}(1+z)t - \frac{t^2}{2}\right) L_N\left(t^2\right) \mathrm{d}t, \tag{4.35b}$$

where $L_N(x)$ are the Laguerre polynomials; the correction to the conductance is given by

$$\Delta\sigma(B) = -\frac{e^2}{4\pi^2\hbar} \left[2C(b, z_{1\pm1}) + C(b, z_{10}) - C(b, z_{00})\right], \tag{4.36}$$

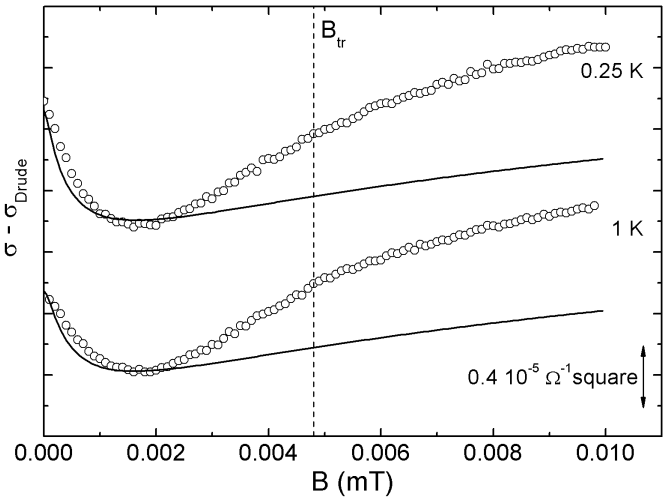

Fig. 4.28: Experimental symmetrised magnetoconductivity (symbols) and fit (lines) with the Zduniak model for 0.25 and 1 K. The vertical line marks the transport field B_{tr}.

where $b = B/B_{tr}$; the factors z_{SS_z} are

$$z_{00} = \frac{B_\varphi}{B_{tr}}, \qquad z_{10} = \frac{B_\varphi + 2B_{so}}{B_{tr}}, \qquad z_{1\pm1} = \frac{B_\varphi + B_{so}}{B_{tr}}. \tag{4.37}$$

The first two terms in equation (4.36) represent the triplet part: $C(b, z_{1\pm1})$ is the contribution of the spin projections with $S_z = +1$ or -1 and $C(b, z_{10})$ represents the $S_z = 0$ states; the last term is the singlet part. It does not depend on the spin-orbit interaction, and contributes with an opposite sign with respect to the triplet (i.e., the singlet is "antilocalising").

Because of the integrals and the series involved in this model, a numerical calculation is needed to evaluate it. The approach for this calculation used in this work, based on Ref. [76], is described in Appendix D.1.

The energy splitting and the Rashba parameter are defined as in the previous diffusive model.

The model depends on the reduced variables $b_{so} = B_{so}/B_{tr}$, $b_\varphi = B_\varphi/B_{tr}$; hence, in the fitting procedure, these variables were considered, keeping B_{tr} fixed.

Attempts to fit the data with this model did not succeed. It reproduces the data in the different magnetic field ranges with very different sets of parameters. In table 4.3 is reported one of these possible sets, and in figure 4.28 the corresponding curve is drawn: it reproduces only the zero field maximum.

According to the interpretation of Punnoose [84], the explanation for the poor fit could be that when $B < B_{so}$ the weak antilocalisation can be described in terms of spin relaxation, as in the Zduniak model, but when $B > B_{so}$ the Aharonov–Bohm analogy, not included in this model, gives a better description of the effect.

Miller model The model by Miller *et al.* [78] describes the weak antilocalisation in the ballistic regime, and considers explicitly the spin-orbit interaction as a spin-dependent vector potential (and thus as an Aharonov–Bohm-like effect).

The Cooperon term is the same as in the Zduniak model, but, to account for the effective vector potential, the variable b is substituted by $x_{S_z} = (B - S_z B_{eff})/B_{tr}$. The parameter B_{eff} is an effective spin-orbit field, which defines the spin-orbit energy splitting; in this formulation, the variable x effectively describes the Aharonov–Bohm-like effect. This field is given by

$$B_{eff} = 2\frac{m^2}{e\hbar^3}\alpha^2 \tag{4.38}$$

for a spin-orbit interaction of the Rashba form with strength α; the energy splitting is then calculated as $\Delta E = 2\alpha k_F$.

The conductivity correction is given by:

$$\Delta\sigma(B) = -\frac{e^2}{4\pi^2\hbar}\left[C(x_1, z_{1\pm1}) + C(x_{-1}, z_{1\pm1}) + C(x_0, z_{10}) - C(x_0, z_{00})\right]. \tag{4.39}$$

The field B_{so}, used in the definition of z_{SS_z}, is related to the spin relaxation through spin-flip, and is given by:

$$B_{so} = \frac{\hbar}{4eD\tau_{so}}. \tag{4.40}$$

This model is valid for $B > B_{eff}$, but, as was shown in figure 3.10, at lower fields its curve is close to those of the other models.

The numerical evaluation requires the same procedure as the evaluation of the Zduniak model.

Note also that, for negligible spin-orbit interaction or for $B \gg B_{so}$ (i.e., when the weak localisation dominates) the Miller and Zduniak model reduce to the same formula:

$$\Delta\sigma(B) = -\frac{e^2}{2\pi^2\hbar}C(x_0, z_{00}). \tag{4.41}$$

In this case, the zero field correction is

$$\Delta\sigma(0) = -\frac{e^2}{2\pi^2\hbar}\ln\left(1 + \frac{1}{z_{00}}\right). \tag{4.42}$$

The model was fitted to the data via the three parameters B_{so}/B_{tr}, B_φ/B_{tr} and B_{eff}/B_{tr}. As shown in figure 4.29, it can reproduce the data and gives a good approximation to the experimental conductance in the whole magnetic field range, although the cusp at the conductivity minimum is quite different from the experimental result.

Although this model is valid when $B > B_{eff}$, attempts to fit the data in this range only (assuming the B_{eff} to be defined by the conductance minimum) or in the complete magnetic

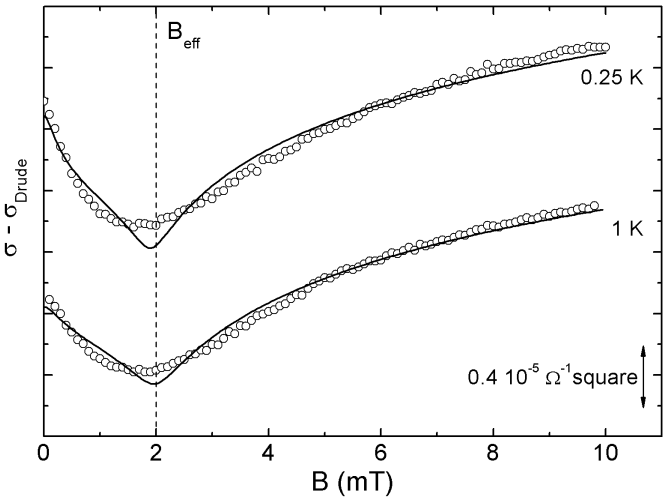

Fig. 4.29: Experimental symmetrised magnetoconductivity (symbols) and fit (lines) with the Miller model for 0.25 and 1 K. The vertical line marks the field B_{eff}.

field range give the same results.

Golub model The models described above do not include the nonbackscattering correction to conductivity. This correction gives another term which sums to the backscattering term. A theory, which includes this terms in the ballistic regime, for arbitrary values of B/B_{tr} and B_{so}/B_{tr}, was developed by Golub in Ref. [50] for the case of Rashba interaction only. The Cooperon is calculated using an expansion in the basis of the Landau levels states.

The conductivity correction is calculated as the sum of a backscattering correction σ_a and a nonbackscattering correction σ_b. The former accounts for the so-called "maximally crossed" terms in a diagrammatic expansion; the latter, which is neglected in other derivations, accounts for other terms. The two terms are given by

$$\sigma_a = -\frac{e^2}{2\pi^2\hbar}\frac{b}{2}\sum_{N=0}^{\infty}\left\{\mathrm{Tr}\left[A_N^3(1-A_N)^{-1}\right] - \frac{P_N^3}{1-P_N}\right\}, \tag{4.43a}$$

$$\begin{aligned}\sigma_b = &-\frac{e^2}{4\pi^2\hbar}\frac{b}{2}\sum_{N=0}^{\infty}\left\{\mathrm{Tr}\left[K_N K_N^T A_N(1-A_N)^{-}1\right] + \mathrm{Tr}\left[K_N^T K_N A_{N+1}(1-A_{N+1})^{-1}\right] - \right.\\ &\left. -Q_N^2\left(\frac{P_N}{1-P_N} + \frac{P_{N+1}}{1-P_{N+1}}\right)\right\}.\end{aligned} \tag{4.43b}$$

The matrices A_N and K_N are defined as [50, 49]

$$A_N = \begin{pmatrix} P_{N-2} - S_{N-2}^{(0)} & R_{N-2}^{(1)} & S_{N-2}^{(2)} \\ R_{N-2}^{(1)} & P_{N-1} - 2S_{N-1}^{(0)} & R_{N-1}^{(1)} \\ S_{N-2}^{(2)} & R_{N-1}^{(1)} & P_N - S_N^{(0)}, \end{pmatrix}, \tag{4.44a}$$

$$K_N = \begin{pmatrix} Q_{N-2} - S^{(1)}_{N-2} & R^{(2)}_{N-2} & S^{(3)}_{N-2} \\ -R^{(0)}_{N-1} & Q_{N-1} - 2S^{(1)}_{N-1} & R^{(2)}_{N-1} \\ -S^{(1)}_{N-1} & -R^{(0)}_{N} & Q_N - S^{(1)}_N \end{pmatrix}. \tag{4.44b}$$

The symbols P_N, Q_N, $R^{(m)}_N$ and $S^{(m)}_N$ are the integrals:

$$P_N = \sqrt{\frac{2}{|b|}} \int_0^\infty \exp\left(-\sqrt{\frac{2}{|b|}}(1+z)t - \frac{t^2}{2}\right) L_N\left(t^2\right) \mathrm{d}t, \tag{4.45a}$$

$$Q_N = \frac{1}{\sqrt{N+1}} \sqrt{\frac{2}{|b|}} \int_0^\infty \exp\left(-\sqrt{\frac{2}{|b|}}t - \frac{t^2}{2}\right) t L^{(1)}_N\left(t^2\right) \mathrm{d}t, \tag{4.45b}$$

$$\begin{aligned} R^{(m)}_N = &\sqrt{\frac{N!}{(N+m)!}} \times \\ &\times \sqrt{\frac{1}{|b|}} \int_0^\infty \exp\left(-\sqrt{\frac{2}{|b|}}t - \frac{t^2}{2}\right) t^m L^{(m)}_N\left(t^2\right) \sin\left(2\Omega\tau\sqrt{\frac{2}{|b|}}t\right) \mathrm{d}t, \end{aligned} \tag{4.45c}$$

$$\begin{aligned} S^{(m)}_N = &\sqrt{\frac{N!}{(N+m)!}} \times \\ &\times \sqrt{\frac{2}{|b|}} \int_0^\infty \exp\left(-\sqrt{\frac{2}{|b|}}t - \frac{t^2}{2}\right) t^m L^{(m)}_N\left(t^2\right) \sin^2\left(\Omega\tau\sqrt{\frac{2}{|b|}}t\right) \mathrm{d}t, \end{aligned} \tag{4.45d}$$

where $L^{(m)}_N(x)$ is the generalised Laguerre polynomial, and $z = B_\varphi/B_{tr}$.

The parameter Ω is the spin-orbit frequency. The product $\Omega\tau$ plays, in this model, the role of B_{so}/B_{tr} in the other models, and weights the intensity of the spin-orbit with the scattering rate. The energy splitting is given by $\Delta E = 2\hbar\Omega$, and the Rashba parameter is $\alpha = \Delta E/2k_F$.

The methods for numerical evaluation of this model were developed during this thesis work; they are described in Appendix D.2.

As can be seen in figure 4.30, this model reproduced very well the data in the whole magnetic field range; the parameters $\Omega\tau$ and z are found through the fit, and are reported in table 4.3.

The 4.2 K data were fitted only with the Miller and the Golub models, assuming for the α parameter the same value at 1 K, since the WAL minimum is not observable at this temperature. The results are reported in table 4.3 and in figure 4.31. In this case, a larger magnetic field range was swept; for the Miller model, only the points with $B > B_{eff}$ were fitted.

A comparison of the four different models is reported in figures 4.32 and 4.33 for 0.25 K and 1 K, respectively. Table 4.3 reports all the extracted parameters.

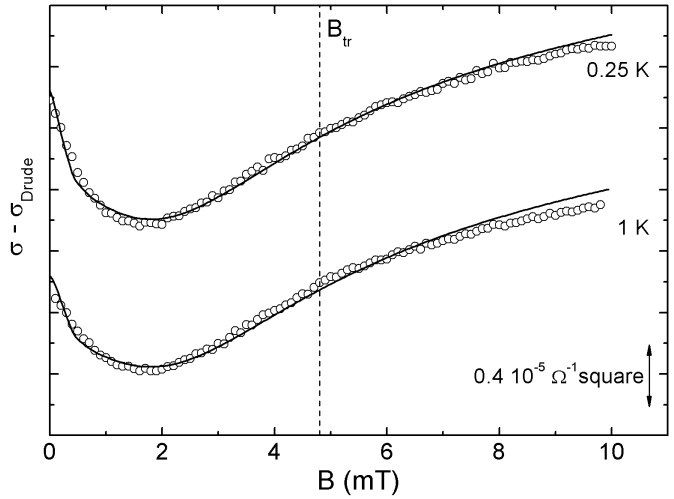

Fig. 4.30: Experimental symmetrised magnetoconductivity (symbols) and fit (lines) with the Golub model for 0.25 and 1 K. The vertical line marks the field B_{tr}.

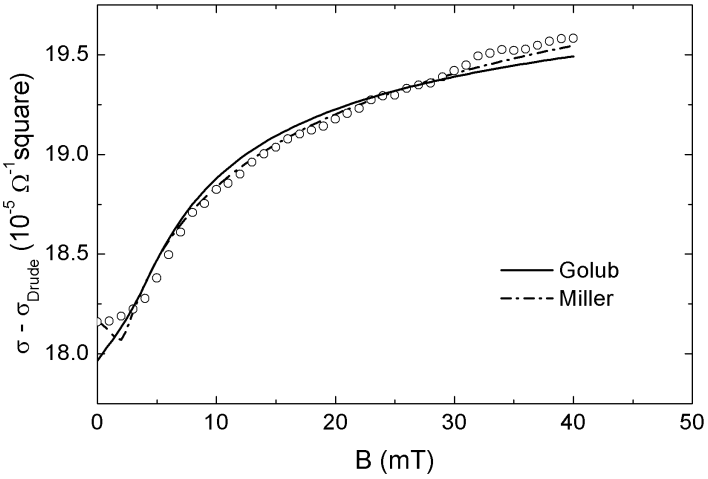

Fig. 4.31: Experimental symmetrized magnetoconductivity at 4.2 K (symbols) and fits with the Golub (continuous line) and Miller (dashed line) models.

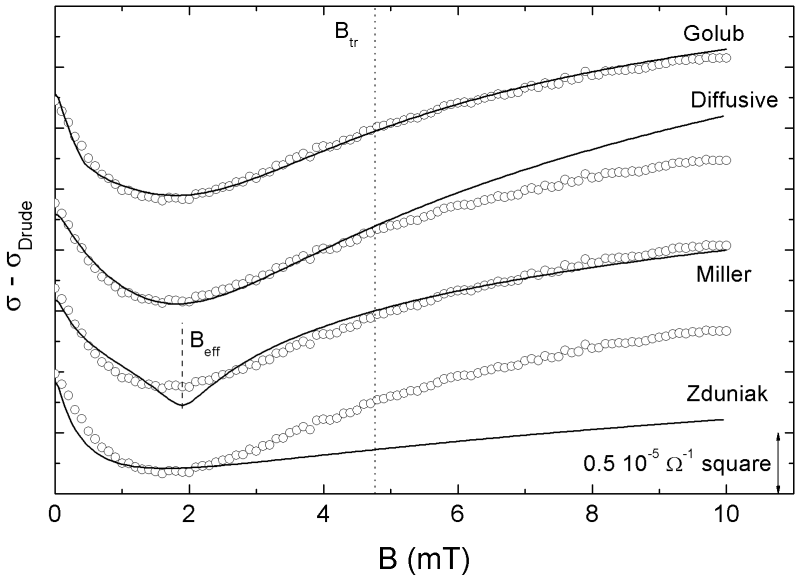

Fig. 4.32: Experimental symmetrised magnetoconductivity and fitted models for 0.25 K. The vertical lines mark the transport field B_{tr} and, for the Miller model, the effective field B_{eff}.

We can see that the diffusive, Miller and Golub models give similar parameter values, while they are different for the Zduniak model.

The diffusive model reproduces the data only in its range of validity, i.e. at low magnetic fields. The failure of the Zduniak model can be attributed to the fact that it treats the spin-orbit interaction only in terms of spin relaxation. On the contrary, the Miller model adds explicitly a spin dependent Aharonov–Bohm-like term to the weak antilocalisation formula, and gives a better approximation to the data.

The best fit is obtained with the Golub model; in addition to incorporate the spin-orbit effect completely, this model also includes the nonbackscattering contributions.

To quantify the relevance of the nonbackscattering correction for the case of our sample, we have compared the fit to the data with and without the nonbackscattering correction, i.e., using $\sigma_a + \sigma_b$ or σ_a only (see equation (4.43)). The quality of the fit, as seen in figure 4.34, is comparable. The parameters extracted from the two procedures are very similar: the Rashba parameter is the same, while the phase coherence time is smaller for the case with σ_a only (it is 69 ps, about 10% smaller than in the $\sigma_a + \sigma_b$ case). Thus, we can conclude that the procedure followed to derive the Golub model leads to a good fit, and the addition of the nonbackscattering correction only affects the extracted value of the phase coherence time, without distorting very much the overall trend of the curve and the extracted SOI strength.

These considerations are valid for both 0.25 K and 1.0 K data. Comparing the extracted values at the two temperatures, we note that the resulting spin-splitting energy is the same; this is expected, since the spin-orbit interaction should be weakly dependent on temperature. The phase relaxation time is decreasing with temperature, as expected. In the Miller model, where two different parameters describe the interference effect (related to the actual spin-splitting

	Diffusive	Zduniak	Miller	Golub
0.25 K				
B_{so} (mT)	1.6	0.25	0.058	2.1
B_{so}/B_{tr}	0.32	0.053	0.012	0.45
B_{eff} (mT)			1.9	
B_{eff}/B_{tr}			0.40	
ΔE_{so} (meV)	0.88	0.35	0.69	0.97
α (10^{-12} eV m)	0.53	0.21	0.41	0.59
B_{φ} (mT)	0.068	0.030	0.048	0.036
B_{φ}/B_{tr}	0.014	0.0062	0.010	0.0076
τ_{φ} (ps)	43	96	60	79
1 K				
B_{so} (mT)	1.5	0.25	0.046	2.1
B_{so}/B_{tr}	0.32	0.053	0.0095	0.45
B_{eff} (mT)			2.0	
B_{eff}/B_{tr}			0.41	
ΔE_{so} (meV)	0.88	0.35	0.70	0.98
α (10^{-12} eV m)	0.53	0.21	0.42	0.60
B_{φ} (mT)	0.12	0.045	0.093	0.59
B_{φ}/B_{tr}	0.026	0.0094	0.019	0.012
τ_{φ} (ps)	23	64	31	49
4.2 K				
B_{so} (mT)			0.019	2.1
B_{so}/B_{tr}			0.044	0.47
B_{eff} (mT)			(2.0)	
B_{eff}/B_{tr}			(0.41)	
ΔE_{so} (meV)			0.70	0.98
α (10^{-12} eV m)			(0.42)	(0.60)
B_{φ} (mT)			0.27	0.83
B_{φ}/B_{tr}			0.049	0.18
τ_{φ} (ps)			10	3.4

Tab. 4.3: Parameters extracted from the different models for WAL and WL at 0.25 K, 1 K and 4.2 K. The fitting parameters were B_{so}/B_{tr}, B_{φ}/B_{tr}, and B_{eff}/B_{tr} for the Miller model only; for the Golub model, $B_{so}/B_{tr} \equiv \Omega\tau$. At 4.2 K the α value was fixed. The other parameters are extracted as described in the text.

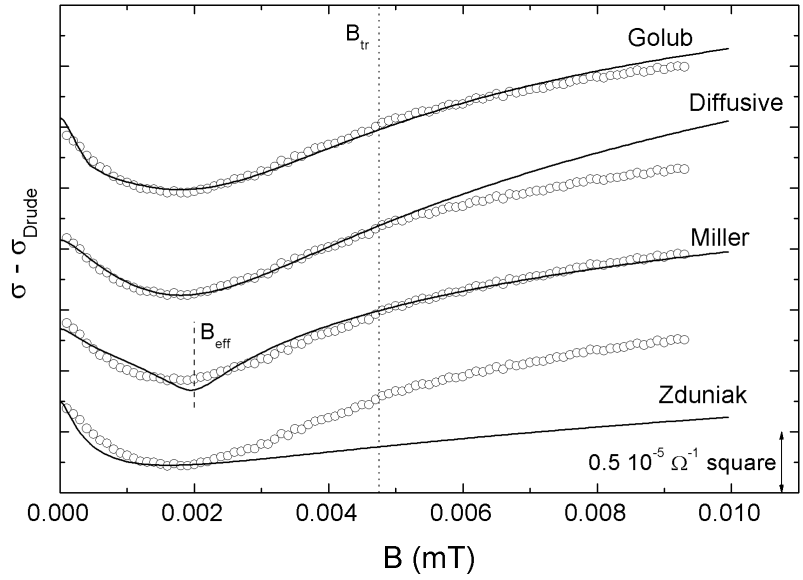

Fig. 4.33: Experimental symmetrised magnetoconductivity and fitted models for 1 K. The vertical lines mark the transport field B_{tr} and, for the Miller model, the effective field B_{eff}.

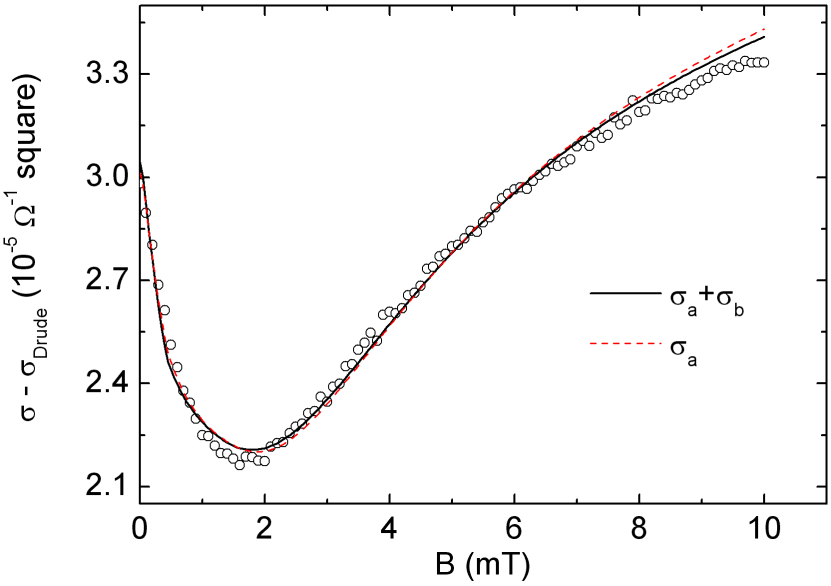

Fig. 4.34: Comparison of conductance fit for the complete Golub model with nonbackscattering correction ($\sigma_a + \sigma_b$, continuous line) and for the case without nonbackscattering correction (σ_a, dashed line).

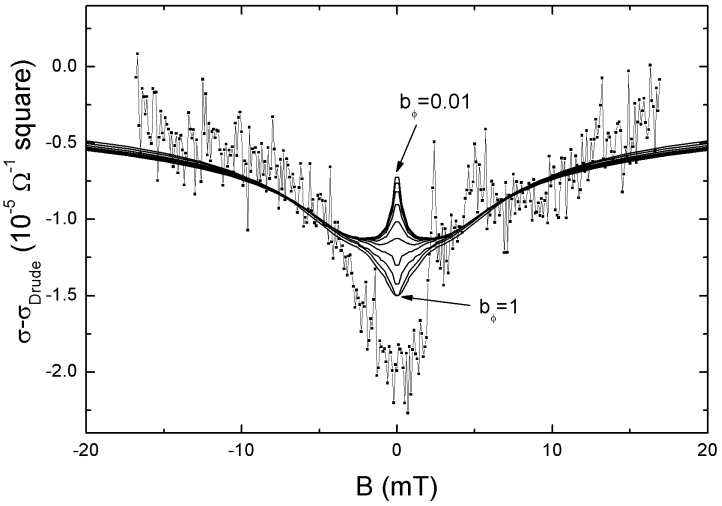

Fig. 4.35: Experimental magnetoconductance at low field for sample A, at 0.25 K (symbols). Lines are the calculated mangetoconductance with the Golub model, with energy splitting $\Delta E = 1.2$ meV, for different values of $b_\varphi = B_\varphi/B_{tr}$ (in the range from 0.01 to 1, with logarithmic spacing).

energy) and spin relaxation, we note that this second effect is actually more efficient at the lowest temperature (i.e., B_{so} is larger, and the spin relaxation time is smaller).

The energy splitting, as calculated from the models (excluding the Zduniak model) is thus between 0.7 and 1.0 meV.

4.3.4 Weak antilocalisation in sample A

The measurement of weak localisation, which has been very useful for the study of spin-orbit interaction in sample B, was attempted also in sample A. The results are shown in figure 4.35.

The reported data are the average of 100 curves, elaborated with the same procedure described for sample B.

We can see that the curve shows a dip around zero Tesla; however, the data are much noisier than in the case of sample B.

In the figure some magnetoconductance curve calculated with the Golub model[5] are also reported, assuming the energy splitting as extracted from the Shubnikov–deHaas measurements ($\Delta E = 1.2$ meV). The parameter $b_\varphi = B_\varphi/B_{tr}$ was varied from 0.01 to 1. The curves show, at small b_φ, the antilocalisation pattern with minima at finite field, while at larger b_φ only the weak localisation minimum at zero is present.

This latter configuration is qualitatively similar to the experimental results; indeed, large values of b_φ are expected in high mobility samples [76]. However, the simulated curves do not reproduce completely the data. Attempts to use other models, or to change the value of the spin splitting, does not give any better approximation to the data.

[5] The transport field in sample A is 0.24 mT, so the data can only be interpreted with a ballistic model.

In conclusion, the quality of the low field data of sample A is not sufficiently good to be analysed in the same manner as sample B, then we rely on the SdH measurements for the measured value of the spin-splitting in sample A.

4.4 Discussion

The features of the two samples investigated in this work and the parameters extracted from the magnetotransport measurements are reported in table 4.4.

The two samples have similar carrier density, but the mobility of sample A is about four times larger than that of sample B. This difference can be attributed to the presence of the AlN exclusion layer in Sample A, which enhances the mobility at large density reducing the alloy scattering, as explained in section 1.2.2.

The high mobility sample A revealed the spin splitting through Shubnikov– deHaas effect; this measurement was not conclusive in sample B. Conversely, weak antilocalisation measurements were conclusive for sample B, but could not give a clear result for sample A.

The extracted spin-splitting energy is of the order of 1 meV for both samples.

These results should be compared with those collected from the literature survey in table 2.2, page 25.

We can see that the samples investigated in this work are among those with the largest carrier density. As for the mobility, sample A is among the sample with large mobility, while sample B has a small mobility.

Samples A and B are among the samples with small spin-splitting energy. For samples with carrier density similar to them, both very large values (close to 13 meV) and non detectable values are found.

To directly compare these data, I report in figure 4.36 the spin-splitting energy as a function of the Fermi wavevector $k_F = \sqrt{2\pi n}$. In the figure, the measurements using the Shubnikov–deHaas effect and the weak antilocalisation are marked as full and empty symbols, respectively. It can be observed that SdH measurements systematically give larger splittings, while WAL yields smaller values. Indeed, as discussed in the previous sections, there are many possible mechanisms which may give beatings patterns similar to the spin splitting; in particular, magnetointersubband scattering and spatial inhomogeneities can be mistaken for the spin splitting signal. The data reported in the literature are not always discussed taking into account these alternatives.

In fact, we note that Thillosen *et al.* [98], for samples with $k_F = 4.7 \cdot 10^8$ m^{-1} and $5.1 \cdot 10^8$ m^{-1}, discarded the SdH measurements, since the beatings pattern is interpreted as an effect of inhomogeneity in the samples. The only work which reports similar values from Shubnikov–deHaas and antilocalisation measurements (by Zhou *et al.*[115]) was made in a sample with $k_F = 5.9 \cdot 10^8$ m^{-1}.

		Sample A	Sample B
Heterostructure	d_{AlGaN} (nm)	23	24.5
	x (Al content)	0.23	0.29
	d_{AlN} (nm)	2	0
	Doping Si (cm^{-3})	0	0
2DEG	n ($10^{16} m^{-2}$)	10.4	10.8
	μ ($m^2V^{-1}s^{-1}$)	2.2	0.48
SdH	μ/μ_q	7.4	3
	ΔE (meV)	1.2	<0.8
	α (10^{-12}eV m)	0.76	<0.5
WAL	τ_φ (ps)		79
	ΔE (meV)		0.97
	α (10^{-12}eV m)		0.60

Tab. 4.4: Sample parameters and measurements results for Sample A and B at 0.25 K.

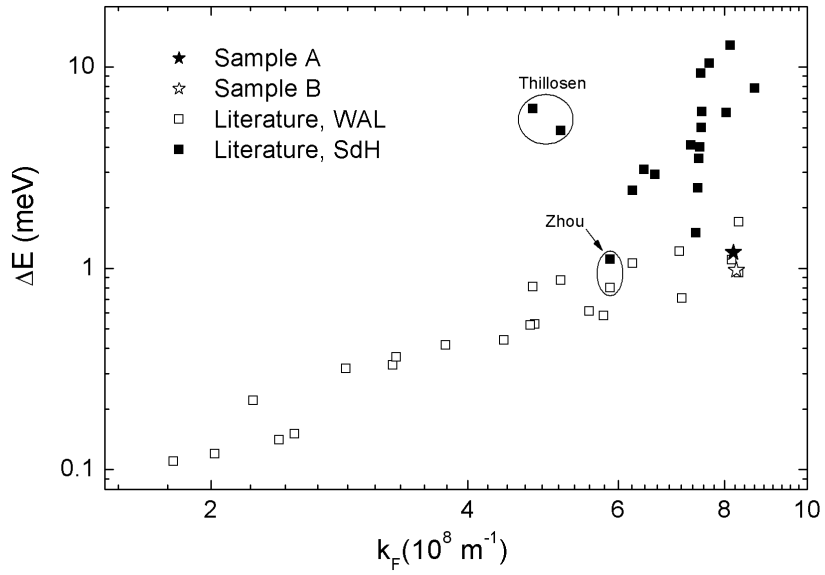

Fig. 4.36: Energy splitting as a function of the Fermi wavevector for samples A and B and for data from literature. Data from Thillosen *et al.* [98] and Zhou *et al.* [115], discussed in the text, are marked.

g	$0.57 \cdot 10^{-30}/2\pi$ eV m^3
γ_{wz}	$0.32 \cdot 10^{-30}$ eV m^3
α_{WSIA}	$0.9 \cdot 10^{-12}$ eV m
b	4
p	$6.1 \cdot 10^5$ m$^{-2/3}$

Tab. 4.5: Parameters used in the estimation of the spin splitting energy as a function of k_F.

Among the reported Shubnikov–deHaas determinations, only the one in this thesis gives a value in agreement with those of weak antilocalisation at large k_F.

We have tried to compare the theories for spin-orbit interaction in GaN 2DEGs (reported in section 2.2) to the experimental data. As discussed in that section, the interplay between the different mechanisms which contribute to the spin-orbit interaction in GaN 2DEGs can make difficult this kind of comparison, and each sample should be treated individually.

We have taken the estimations of the different terms of the spin-orbit energy to calculate the total energy splitting and check how the theory compares with the experimental data (those obtained in this work and those reported in the literature).

The total energy splitting at the Fermi wavevector is given by the formula (see also equation (2.11))

$$\Delta E = 2\left[\alpha_{BR}(k_F) + \alpha_{WSIA} - (\gamma_{wz} + \gamma_{bands})\left(b\langle k_z^2\rangle - k_F^2\right)\right]k_F. \tag{4.46}$$

$\alpha_{BR}(k_F) = gk_F^2$ accounts for the spin-orbit interaction arising from the structural inversion asymmetry of the quantum well (Rashba effect); the coefficient $g = 0.57 \cdot 10^{30}/2\pi$ eVm is estimated in Ref. [68].

The coefficients α_{WSIA}, γ_{wz} and b are related to the band structure (wurtzite structural inversion asymmetry and Dresselhaus effect) of the GaN; the estimations reported in section 2.2 (also recalled in table 4.5) will be used.

The parameter γ_{band}, which describes the energy splitting due to the coupling between the conduction bands $\Delta_{C1} - \Delta_{C3}$, is more problematic, since its value has not been estimated. Moreover, since the energy splitting expected from this mechanism is found to have a discontinuity as a function of k (see figure 2.5a, page 18), the value for the parameter may depend critically on the details of the heterostructure.

As a consequence, we have chosen to evaluate equation (4.46) for different values of γ_{band} ($\gamma_{band} = 0, \gamma_{wz}, 5\gamma_{wz}, 10\gamma_{wz}$), and to explore its effect parametrically.

As for the estimation of $\langle k_z^2\rangle$, we can use the same considerations used in Ref. [73]. For the first subband of a one-dimensional square quantum well $k_z = \pi/d$, d being the width of the well; if $\langle z\rangle$ is the average distance from the barrier, $d = 2\langle z\rangle$; hence $k_z = \pi/2\langle z\rangle$. In the case of a heterojunction, d is not constant because of the band bending, and depends on the Fermi level. The quantity $\langle k_z^2\rangle$ is estimated as $\langle k_z^2\rangle = (\pi/2\langle z\rangle)^2$.

Then, the value of $\langle z \rangle$ must be estimated. The simplest approximation for this value can be found using a variational approach with a Fang-Howard test wavefunction [35, chap. 9], which describes a triangular quantum well. The wavefunction is defined to be 0 in the barrier layer (i.e., no barrier penetration). In this approximation, $\langle z \rangle$ depends only on the carrier density as

$$\langle z \rangle = 3\left(\frac{33me^2}{8\hbar^2\varepsilon_0\varepsilon_r}n\right)^{-1/3}, \tag{4.47}$$

so that $\langle k_z^2 \rangle$, using $n = k_F^2/2\pi$, is

$$\langle k_z^2 \rangle = \left(\frac{\pi}{6}\right)^2\left(\frac{33}{16\pi}\frac{me^2}{\hbar^2\varepsilon_0\varepsilon_r}k_F^2\right)^{2/3} = \left(\frac{\pi}{6}\right)^2\left(\frac{33}{4}\frac{1}{a_B^*}k_F^2\right)^{2/3} \equiv p\,k_F^{4/3}. \tag{4.48}$$

The parameter p is, in this approximation, a constant, and depends only on the material parameters m (effective mass) and ε_r (relative permittivity); a_B^* is the effective Bohr radius. The value of p is reported in table 4.5.

With these relations, equation (4.46) becomes

$$\Delta E = c_3k_F^3 + c_2k_F^{7/3} + c_1k_F, \tag{4.49}$$

with

$$c_3 = 2(g + \gamma_{wz} + \gamma_{bands}), \tag{4.50a}$$

$$c_2 = -2(\gamma_{wz} + \gamma_{bands})b\,p, \tag{4.50b}$$

$$c_1 = 2\alpha_{WSIA}. \tag{4.50c}$$

The results of this calculation are shown in figure 4.37. For small or large γ_{band}, when the linear or the cubic term dominates, we see that the behaviour is monotone. In the case of small γ_{band}, the maximum energy splitting is of the order of 1 meV, while for large γ_{band} can exceed 10 meV. For intermediate values of γ_{band}, the spin splitting has a zero at finite k_F, as discussed in section 2.2.1.

It is worth noting that the contribution of the Rashba effect is indeed very small compared to the WSIA contribution. With the parameters value reported in the table 4.5, the ratio between the energy splitting due to the WSIA only and that due to Rashba only is $\Delta E_{WSIA}/\Delta E_R = \alpha_{WSIA}/(2\pi g n) \approx 1.6 \cdot 10^{18}\mathrm{m}^{-2}/n$; the largest carrier density are of the order of $1 \cdot 10^{17}$ m^{-2}, so the WSIA can be more than ten times larger than Rashba term.

Furthermore, by inspecting table 4.5, we can see that the parameters g and γ_{wz} are similar, so that the contributions of Rashba and Dresselhaus effect are similar.

This consideration may explain why in Refs. [64, 98] the spin splitting was found to be described by a linear dependence on k_F, with a constant α.

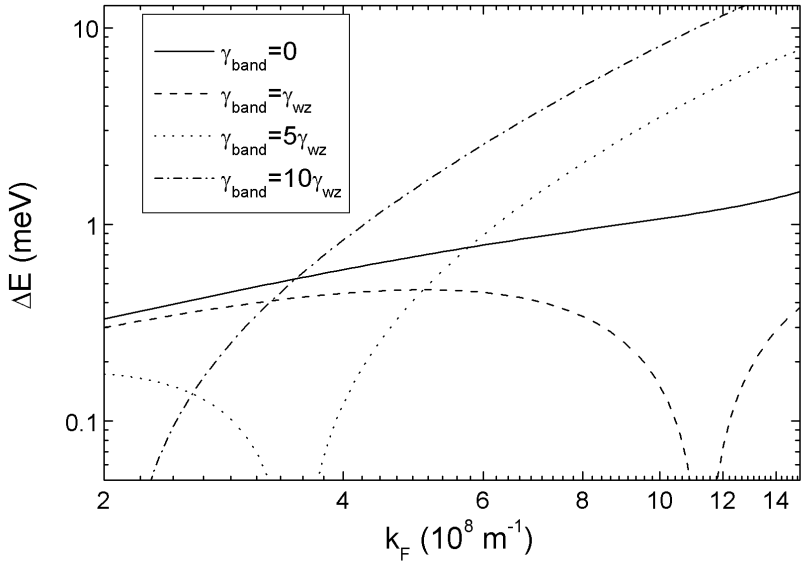

Fig. 4.37: Estimations of the spin splitting energy in a AlGaN/GaN heterostructure, as a function of the Fermi wavevector, calculated using equation (4.46). The values of the parameters are reported in table 4.5. The wavevector range covers carrier density from $0.64 \cdot 10^{16}$ m^{-2} to $36 \cdot 10^{16}$ m^{-2}.

In figure 4.38 some of the simulated curves are reported, together with the data collected from the literature and in this work.

As expected, the effect of the $\Delta_{C1} - \Delta_{C3}$ coupling (through γ_{band}) is necessary to explain the larger splitting energies, but the smallest splittings reported can be understood assuming a small γ_{band}.

A more thorough analysis of the band structure of gallium nitride and its dependence on the heterostructure parameters should help understand if such a large spread in the parameter γ_{band} is justified.

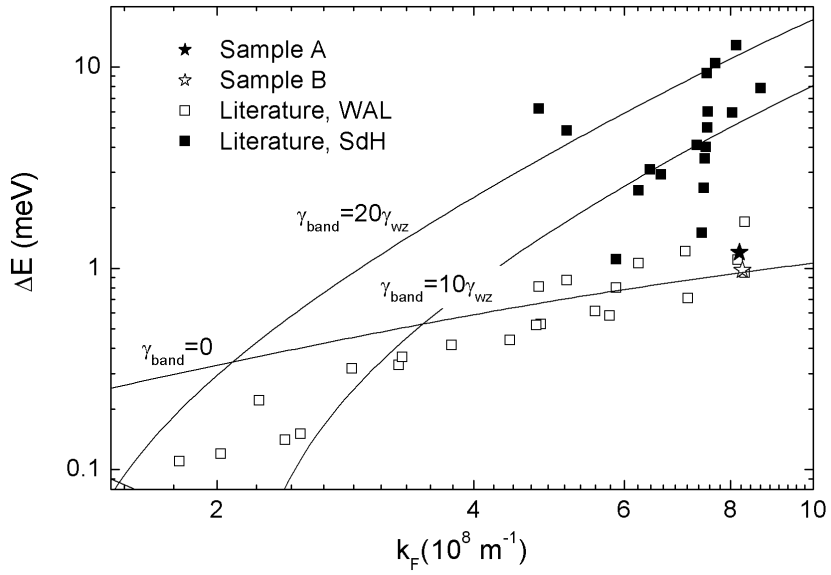

Fig. 4.38: Energy splitting as a function of the Fermi wavevector for samples A and B and for data from literature (symbols) and calculated energy splitting for different values of γ_{band} (lines).

5. CONCLUSIONS

In this thesis, two-dimensional electron gases in gallium nitride based heterostructures have been investigated with magnetotransport measurements. The aim of the study has been the determination of the spin-splitting energy in the conduction band. Two effects have been exploited: Shubnikov– deHaas effect and weak antilocalisation. The motivation has been the interest in testing this system as a suitable material for spintronics, since prior results were not conclusive.

Two samples have been investigated. Both have a large carrier density; one of the two has also high mobility. Their electric properties were measured at a cryogenic temperature, down to 0.25 K; the maximum magnetic field was 12 T.

In the high magnetic field range Shubnikov–deHaas oscillations could be observed. In this effect, the spin-splitting manifests itself as a beatings pattern in resistivity oscillations. At very low magnetic field, another effect of the spin splitting, the weak antilocalisation, could be observed.

To study in details the Shubnikov–deHaas data, not only the frequency domain analysis has been considered, but also the amplitude and phase modulation.

Models suitable to account for different lineshapes for the density of states, inhomogeneity in the samples, and intersubband scattering were developed.

The comparison of these models to the data allowed a quantification of the transport parameters, and gave indication on the scattering mechanism operative in the sample.

The splitting energy was determined; other possible mechanisms which may give rise to the beatings patterns were excluded by comparison with classical Hall effect measurements or thanks to the developed models.

For the interpretation of the weak antilocalisation measurements theoretical models reported in the literature, based on different assumptions or approximations, were considered.

Their numerical evaluation was performed with tailored algorithms.

The validity of these models is discussed in comparison with the experimental data.

These analyses established a spin-splitting energy of the order of 1 meV in both samples.

A survey of literature reveals that the values of this energy in gallium nitride are reported to be of this order of magnitude when determined with weak antilocalisation, while the analysis

of the Shubnikov–deHaas oscillation give larger values.

One result of this work is that the Shubnikov–deHaas data should be analysed with great care, to exclude that effects other than spin splitting are responsible for the observed features, while the weak antilocalisation measurements are more reliable.

In the comparison with theoretical models, the effect of the parameter γ_{band} was found to be crucial for the estimation of the spin-splitting energy.

APPENDICES

A. BEATINGS

Beatings patterns arise when two (or more) harmonic components are present in a signal. In this appendix the two cases of two components of equal and different amplitude will be considered.

When the two amplitudes are the same, the signal can be analysed with the help of trigonometric relations:

$$\begin{aligned} x(t) &= \cos\left(\omega_1 t + \phi_1\right) + \cos\left(\omega_2 t + \phi_2\right) = \\ &= 2\cos\left(\frac{\omega_1 - \omega_2}{2}t + \frac{\phi_1 - \phi_2}{2}\right) \cdot \cos\left(\frac{\omega_1 + \omega_2}{2}t + \frac{\phi_1 + \phi_2}{2}\right), \end{aligned} \tag{A.1}$$

where $\omega = 2\pi f$ is the angular frequency.

In formula (A.1), the first, low-frequency, factor is an envelope determining the null points (nodes) and the maximum amplitude points, while the second determines the actual maxima and minima. The nodes are found when the argument of the envelope is equal to an odd multiple of $\pi/2$:

$$\frac{\omega_1 - \omega_2}{2}t + \frac{\phi_1 - \phi_2}{2} = \frac{2n+1}{2}\pi, \qquad n = 0, 1 \ldots \tag{A.2}$$

The position of the n-th node is thus:

$$t_n = \frac{2n+1}{\omega_1 - \omega_2}\pi - \frac{\phi_1 - \phi_2}{\omega_1 - \omega_2}, \tag{A.3}$$

and the distance between two consecutive nodes is

$$t_{n+1} - t_n = \frac{2\pi}{\omega_1 - \omega_2} = \frac{1}{f_1 - f_2}. \tag{A.4}$$

The frequency difference can be extracted from the nodes positions:

$$f_1 - f_2 = \frac{2n+1}{2t_n} - \frac{\phi_1 - \phi_2}{2\pi t_n}. \tag{A.5}$$

The actual maxima and minima are found when

$$\frac{\omega_1 + \omega_2}{2}t + \frac{\phi_1 + \phi_2}{2} = m\pi, \qquad m = 0, 1 \ldots \tag{A.6}$$

Their positions are given by

$$t_m = \frac{2\pi m}{\omega_1 + \omega_2} - \frac{\phi_1 + \phi_2}{\pi(\omega_1 + \omega_2)}. \tag{A.7}$$

If the signal has two components with different amplitude, for example

$$x(t) = A_1 \cos\Big(\omega_1 x + \phi_1\Big) + A_2 \cos\Big(\omega_2 x + \phi_2\Big) = |x(t)| \cos\varphi(t), \tag{A.8}$$

it is easier to use the complex numbers to calculate the amplitude and the phase of this signal.

The amplitude modulation is given by

$$|x(t)| = \sqrt{A_1^2 + A_2^2 + 2A_1A_2 \cos\Big((\omega_1 - \omega_2)t + (\phi_1 - \phi_2)\Big)}. \tag{A.9}$$

The "nodes" (i.e., the point where the minimum amplitude is found) are at the same positions as in the case of equal amplitude (equation (A.3)). At this minimum the amplitude is $|A_1 - A_2|$, while at the maximum is $A_1 + A_2$.

The phase is given by

$$\begin{aligned}\varphi(t) &= \arctan\left[\frac{A_1 \sin\Big(\omega_1 t + \phi_1\Big) + A_2 \sin\Big(\omega_2 t + \phi_2\Big)}{A_1 \cos\Big(\omega_1 t + \phi_1\Big) + A_2 \cos\Big(\omega_2 t + \phi_2\Big)}\right] = \\ &= \frac{(\omega_1 + \omega_2)t + \phi_1 + \phi_2}{2} \\ &+ \arctan\left[\frac{A_1 - A_2}{A_1 + A_2} \tan\frac{(\omega_1 - \omega_2)t + (\phi_1 - \phi_2)}{2}\right].\end{aligned} \tag{A.10}$$

A.1 Analytical representation formalism

The same results can be found through the analytical representation of the signal. This formalism is also more rigorous for more complicated signals.

The analytical representation of a signal $x(t)$ is [3, chap. 9.6]

$$x_A(t) = x(t) + i\hat{x}(t), \tag{A.11}$$

where $\hat{x}(t)$ is the Hilbert transform of the signal. The envelope is calculated from the amplitude of this representation as

$$|x_A(t)| = \sqrt{x(t)^2 + \hat{x}(t)^2}, \tag{A.12}$$

and the instantaneous phase as

$$\varphi_x(t) = \arctan\frac{\hat{x}(t)}{x(t)}. \tag{A.13}$$

The Hilbert transform is defined as

$$\hat{x}(t) = \frac{1}{\pi}\text{p.v.}\int_{-\infty}^{\infty}\frac{x(\tau)}{t-\tau}\,\mathrm{d}\tau. \tag{A.14}$$

This integral is easily calculated for functions like $A(t)\cos(\omega t + \pi)$ by residue integration. If the damping function $A(t)$ is limited in a neighbourhood of t, then the integral is

$$\begin{aligned}\hat{x}(t) = &-\frac{1}{\pi}\text{p.v.}\int_{-\infty}^{\infty}\frac{A(\tau)}{t-\tau}\cos(\omega\tau)\,\mathrm{d}\tau = \\ =&\text{Imag}\left[\text{Res}_{\tau=t}\,\frac{A(\tau)}{(t-\tau)}\exp(i\omega\tau)\right] = A(t)\sin(\omega t).\end{aligned} \tag{A.15}$$

Because of the linearity of the Hilbert transform, this formalism can be directly extended to the sum of two functions, and hence the same formulae of the previous section are recovered.

The numerical, discrete Hilbert transform can be applied to the extraction of the envelope and the phase of experimental data.

The derivation of the formulae for the Dingle plot in section 4.2.3 makes use of the formulae reported in this appendix.

The functions involved in the study of the Shubnikov–deHaas effect are of the kind $SdH(t) = A(t)\cos(\omega t + \pi)$, with

$$A(t) = \sigma D_T(t)h(t), \quad D_T(t) = \frac{ct}{\sinh ct}, \quad h(t) = \exp(-\beta t) \text{ or } \exp(-\beta t^2). \tag{A.16}$$

These functions satisfy the hypothesis for $A(t)$.

When the Dingle plots are calculated, the amplitude modulation of the oscillation must be calculated, for example with equation (A.9). In particular, in the case of the two-channels models, it is found that

$$\begin{aligned}\ln\frac{\Delta\rho}{D_T} \propto&\frac{1}{2}\ln\left[(\sigma_1 h_1(t))^2 + (\sigma_2 h_2(t))^2 + 2\sigma_1\sigma_2 h_1(t)h_2(t)\cos\left((\omega_1-\omega_2)t\right)\right] \\ =&\ln\sigma_1 + \ln h_1(t) + \frac{1}{2}\ln\left[1 + \left(\frac{\sigma_2 h_2(t)}{\sigma_1 h_1(t)}\right)^2 + 2\frac{\sigma_2 h_2(t)}{\sigma_1 h_1(t)}\cos\left((\omega_1-\omega_2)t\right)\right].\end{aligned} \tag{A.17}$$

Application of this formula, with the suitable choice for $h_{1,2}(t)$ yields equations (4.14) and (4.19).

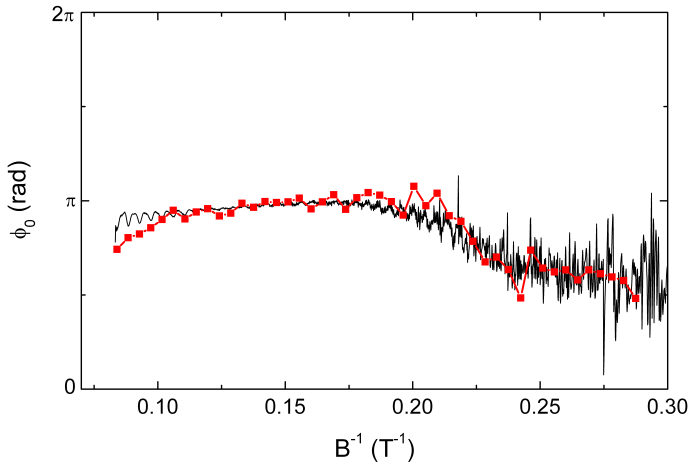

Fig. A.1: Comparison of the residual phase extracted from the position of the maxima (square symbols) and from the Hilbert transform (line).

A.2 Extraction of the residual phase from the experimental data

The investigation of oscillatory phenomena can require the extraction of the residual phase from the data.

In the case of a simple cosine wave $x(t) = \cos(\omega t + \alpha)$ the instantaneous phase is $\varphi(t) = \omega t + \alpha$, and $\alpha = \varphi(t) - \omega t$ is the initial phase.

In the case of two components, a suitable test frequency has to be chosen, for example $\omega = (\omega_1 + \omega_2)/2$; then, the quantity $\varphi(t) - \omega t$ is the residual phase. From equation (A.10), it is given by a step-like arctangent function.

In the case of the Shubnikov–deHaas effect, this quantity can be calculated from the position of the maxima $1/B_m$ and using a trial frequency f_0, through the relation

$$2\pi f_0/B_m + \phi_0 = 2\pi m, \quad m = 0, 1, 2 \ldots \tag{A.18}$$

The value ϕ_0 can then be extracted using the integer part function. An alternative method uses directly the Hilbert transform of the signal.

A comparison of the two procedures (direct calculation and Hilbert transform) to extract ϕ_0 is given in figure A.1, the experimental data being those of device 1 described in section 4.2. The phase calculated through the Hilbert transform shows oscillations superimposed to the trend with the jump. They are related to the higher harmonics components. At large B^{-1}, where the oscillations are damped, the signal is noisier.

B. MODEL FOR ROUGHNESS SCATTERING

The roughness scattering potential can be written as [23]

$$U_q^2 = \pi\Delta^2\Lambda^2\left(\frac{e^2 n_{2D}}{4\varepsilon_r\varepsilon_0}\right)^2 \exp\left(-q^2\Lambda^2/4\right), \tag{B.1}$$

where Δ is the roughness height (root mean square), and Λ is the correlation length; n_{2D} is the carrier density and $q = 2k_F \sin\Theta/2$.

Quantum and transport lifetimes are given by

$$\frac{1}{\tau_q} = \frac{m}{\pi\hbar^2}\int_0^\pi \frac{U_q^2}{\varepsilon_q^2}\mathrm{d}\Theta, \tag{B.2a}$$

$$\frac{1}{\tau_t} = \frac{m}{\pi\hbar^2}\int_0^\pi (1-\cos\Theta)\frac{U_q^2}{\varepsilon_q^2}\mathrm{d}\Theta, \tag{B.2b}$$

where $\varepsilon_q = 1 + q_s/q$ is the permittivity in the Thomas-Fermi model, and $q_s = me^2/2\pi\varepsilon_r\varepsilon_0\hbar^2$.

The ratio τ_q/τ_t is a function of Λ, of the 2DEG density (through k_F) and of the material parameters (m and ε_r):

$$\frac{\tau_q}{\tau_t} = 1 - \frac{\int_0^\pi \cos\Theta \frac{\exp\left(-q^2\Lambda^2/4\right)}{\varepsilon_q^2} d\Theta}{\int_0^\pi \frac{\exp\left(-q^2\Lambda^2/4\right)}{\varepsilon_q^2} d\Theta}. \tag{B.3}$$

A numerical integration allows to find Λ from τ_q/τ_t (see also figure B.1); Δ can be evaluated form one of the two lifetimes.

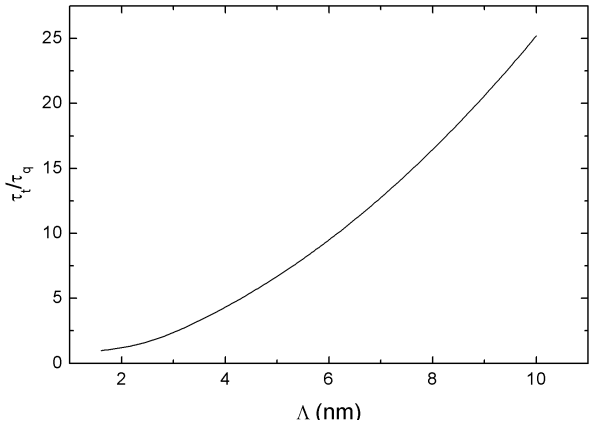

Fig. B.1: Numerical simulation of τ_t/τ_q as a function of the correlation length Λ for a 2DEG in GaN with $n_{2D} = 10^{17}$ m^{-2}.

C. SHUBNIKOV–DEHAAS OSCILLATIONS BACKGROUND

The Shubnikov–deHaas oscillations are commonly superimposed to a slowly varying background. This background is usually removed before the analysis of the oscillations. This elaboration can be simply performed with numerical (possibly multiple) differentiation of the raw signal, or with a high-pass Fourier filter; however, these techniques have their drawbacks, such as noise enhancement or distortion of the signal, and, of course, all the information on the background is discarded.

In this work, the background was extracted with the following procedure:

1. Maxima and minima of the oscillations are determined.
2. A "maximum curve" and a "minimum curve" are calculated by interpolation.
3. The average curve is calculated between maximum and minimum. In the range where no oscillation is visible, interpolations of the data (or the data itself) are taken. The resulting curve is the "background magnetoresistance".
4. The background is finally subtracted from the data.

Different terms can contribute to the magnetoresistance background. In particular, electron-electron interaction and disorder contribution to magnetoresistance will be discussed here.

In this appendix the data from sample A will be discussed in details; at the end, also the data of the sample B are reported.

Although in the discussion of the Shubnikov–deHaas data the presence of two spin-split conductive channels has been assessed, for the sake of simplicity in the following analysis a single, spin-degenerate conductive channel will be considered. This simplification has no effect on the derived background.

C.1 Electron-electron interaction

Electron-electron interaction gives rise to a negative magnetoresistance, with quadratic dependence on the magnetic field (in the simplest picture) [23].

The conductance correction is independent of the field, and is given by

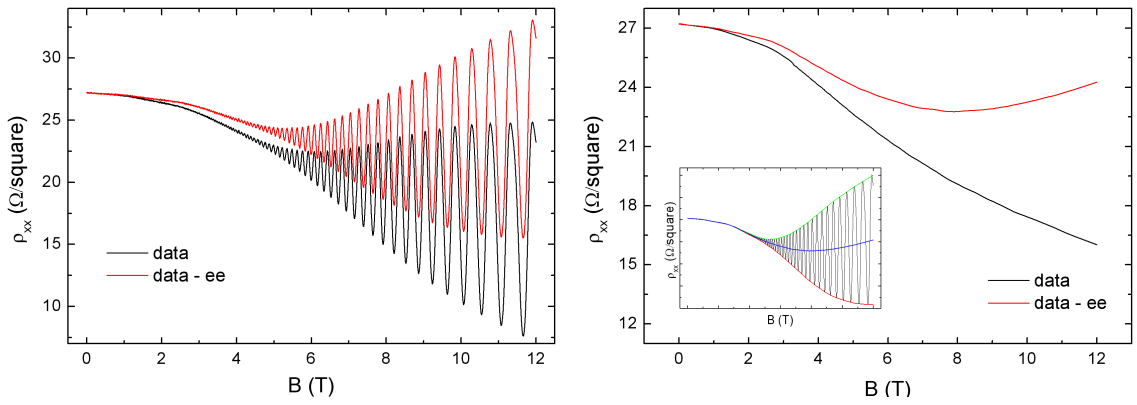

Fig. C.1: (a) Data from device 1 in sample A before and after the subtraction of the electron-electron interaction correction. (b) Magnetoresistance background before and after the subtraction of the electron-electron interaction correction; inset: Extraction of the magnetoresistance background from the SdH oscillations. Data are taken at 0.25 K.

$$\Delta\sigma_{ee} = \frac{e^2}{\pi h}\left[4 - 3\frac{\ln(1+F_0^\sigma)}{F_0^\sigma}\right]\ln\left(\frac{k_B T\tau}{\hbar}\right), \tag{C.1}$$

where F_0^σ is the Fermi liquid constant. In terms of the adimensional radius $r_s = m/(\varepsilon_r a_B\sqrt{\pi n_{2D}})$, and in the limit $r_s \ll 1$, it is given by

$$F_0^\sigma = -\frac{1}{2\pi}\frac{r_s}{\sqrt{2-r_s^2}}\ln\left(\frac{\sqrt{2}+\sqrt{2-r_s^2}}{\sqrt{2}-\sqrt{2-r_s^2}}\right). \tag{C.2}$$

The magnetoresistance is

$$\frac{\rho_{xx}(B)}{\rho_0} \simeq 1 - \frac{\Delta\sigma_{ee}}{\sigma_0} + \frac{\Delta\sigma_{ee}}{\sigma_0}(\mu B)^2. \tag{C.3}$$

The correction to the transverse resistivity ρ_{xy} is negligible.

Following Ref. [23], the following procedure is applied to subtract this contribution from the experimental data: resistivity data are converted to conductivity, then $\Delta\sigma_{ee}$ is subtracted, and data are converted back to resistivity. The parameters needed for this procedure are the carrier density, the transport lifetime, and the temperature; using the experimental values for these parameters, $\Delta\sigma_{ee}$ is calculated. The result of the subtraction of the electron-electron interaction correction from the experimental data is shown in figure C.1 for the data at 0.25 K.

We can see that a background variation is still observable. In particular, a negative magnetoresistance is found, followed by a positive trend in the highest field range. In the data taken at 4.2 K (figure C.4) only the negative magnetoresistance is found. To explain both these features of the residual magnetoresistance, models describing disorder effects are considered.

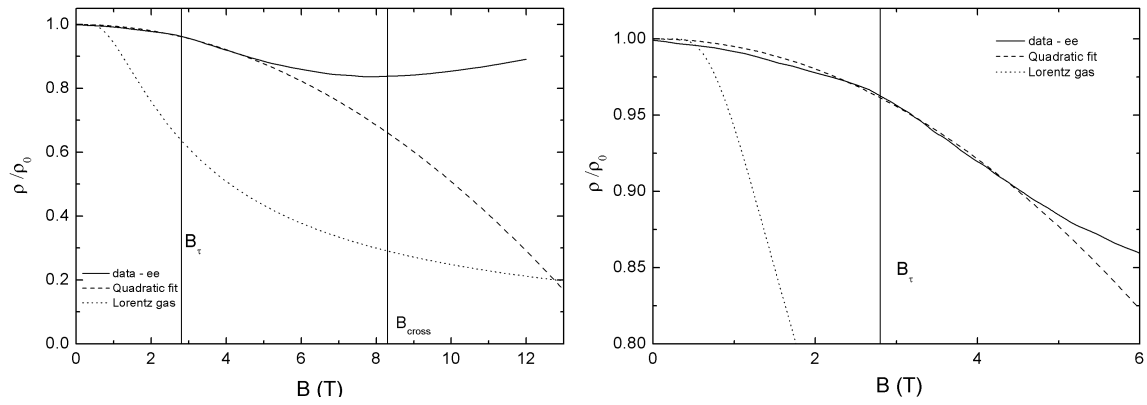

Fig. C.2: Comparison of experimental data at 250 mK to the model for disorder-induced magnetoresistance. Panel (b) is a detail of the low field region.

C.2 Disorder-induced magnetoresistance

Lorentz Gas A Lorentz gas is an electron gas moving in the presence of strong scatterers; this model predicts a negative magnetoresistance [23]. The resistivity tensor components are

$$\frac{\rho_{xx}}{\rho_0} = \frac{1-P}{1+P^2/\beta^2}, \qquad \frac{\rho_{xy}}{\rho_0} = \beta\frac{1-P^2/\beta^2}{1+P^2/\beta^2}, \tag{C.4}$$

where

$$P = \exp\left(-\frac{2\pi}{\beta}\right), \qquad \beta = \mu B. \tag{C.5}$$

The only parameter in this model is the transport mobility, which is already known from previous measurements. The calculated magnetoresistance is shown in figure C.2, along with the experimental data. The model reproduces the data only in a narrow range at low magnetic field, and definitely cannot account for the positive trend at high field.

Two-components disorder In Ref. [80] Mirlin *et al.* developed a model for the magnetoresistance of non-interacting electrons in a two-components disorder: an array of strong scatterers (impurities or interface roughness) and a weak and smooth random potential (remote impurities). In the limit with strong scatterers only the Lorentz gas is found, while in the limit with only the smooth potential a positive magnetoresistance is found, as will be shown at the end of this section.

The scatterers have radius a and density n_S, while the smooth potential has a correlation length Λ. The scattering rate is respectively τ_S^{-1} and τ_L^{-1}; we assume $\tau_S^{-1} \gg \tau_L^{-1}$: in this case, the transport scattering time is $\tau \approx \tau_S$, and the mean free path is $l \approx v_F\tau_S$.

Note that the model is valid only if the motion in the disorder is not adiabatic, that is, the centre of the orbit moves in a diffusion regime (rather than drift); the condition to be satisfied is

that the orbit centre displacement during a cyclotron orbit is much greater than Λ.

The frequency scales for this model, to be compared with the cyclotron frequency $\omega_c = eB/m$, are:

- $\omega_\tau = 2\pi/\tau$: only fields such as $\omega_c \gg \omega_\tau$ are considered;
- $\omega_0 = (2\pi n_S)^{1/2} v_F (2\gamma l_S/l_L)^{1/4}$, $\gamma \sim 1$, $l_{S,L} = v_F \tau_{S,L}$;
- $\omega_{perc} = 1.67 v_F n_S^{1/2}$: percolation threshold;
- $\omega_{cross} = v_F (4\pi n_S^2 l_S^2 l_L^{-1})$: two-components/Lorentz gas crossover;
- $\omega_{ad} = v_F (4\pi/\Lambda^2 l_L)^{1/3}$: adiabatic transport limit: the non-adiabatic motion condition is $\omega_c \ll \omega_{ad}$.

In the following, characteristic magnetic fields B_i rather than frequencies ω_i are considered; the conversion is given by $B_i = m\omega_i/e$.

For $B \ll B_0$ there is a parabolic negative magnetoresistance:

$$\frac{\rho(B)}{\rho_0} = 1 - \frac{B^2}{B_0^2}. \tag{C.6}$$

For $B \gg B_0$ the magnetoresistance is:

$$\frac{\rho(B)}{\rho_0} \sim \left(\frac{B_0}{B}\right)^4. \tag{C.7}$$

Three regimes can be distinguished according to the relative values of the frequency scales, as in figure C.3:

A: $B_0 \ll B_\tau$: Lorentz gas regime (contribution to the magnetoresistance only from the strong scatterers);

B: $B_\tau \ll B_0 \ll B_{cross} \ll B_{perc}$: Lorenz gas regime for $B < B_{cross}$;

C: $B_\tau \ll B_0 \ll B_{perc} \ll B_{cross}$: the Lorenz regime is never reached.

The quadratic model for magnetoresistance has been fitted, in the low magnetic field range, to the experimental data after subtraction of electron-electron interaction. The results are shown in figures C.2 and C.4 for data measured at 250 mK and 4.2 K, respectively.

In table C.1 the parameters extracted from the data are summarised. They are calculated as follows:

- F_0^σ, r_s, $\Delta\sigma_{ee}$, B_τ from transport parameters (carrier density and mobility) calculated from classical Hall effect.

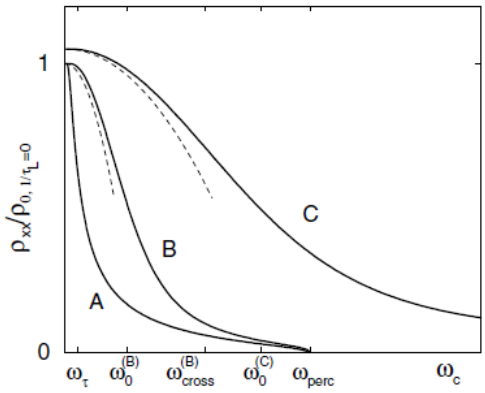

Fig. C.3: Comparison of different magnetoresistance regimes in two-components disorder model. See text for details.

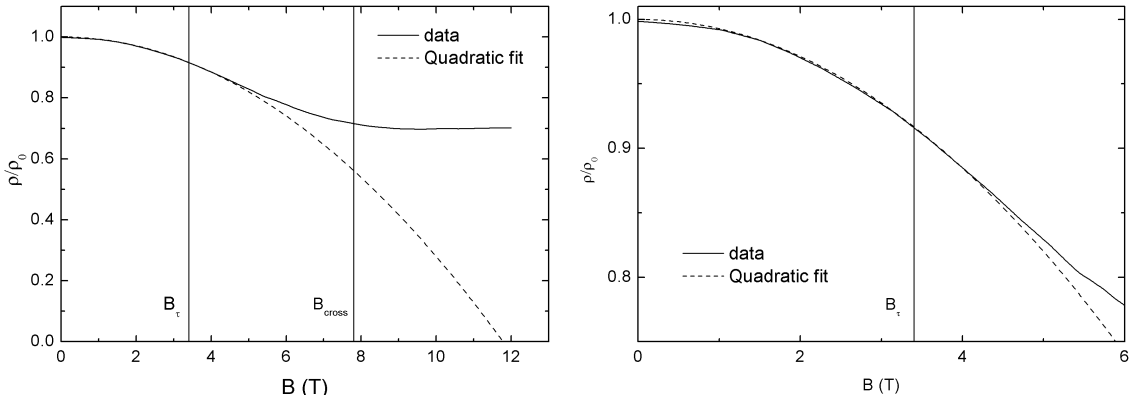

Fig. C.4: Comparison of experimental data at 4.2 K to the model for disorder-induced magnetoresistance. Panel (b) is a detail of the low field region.

Quantity	Value (250 mK)	Value (4K)
r_s	0.80	0.82
F_0^σ	−0.25	−0.26
$\Delta\sigma_{ee}$ ($10^{-5}\Omega^{-1}$)	−1.58	+0.23
B_τ (T)	2.8	3.0
B_0 (T)	14	11.8
l_S (µm)	1.1	1.1
a (nm)	5.4	5.7
n_S (10^{13} m^{-2})	7.9	8.2
B_{perc} (T)	7.9	7.9
l_L (µm)	1.2	2.2
B_{cross} (T)	8.2	7.5

Tab. C.1: Important quantities and their estimated values for the study of magnetoresistance background.

- B_0 from fit to the data (in the low field range) of equation (C.6).
- a is assumed to be the correlation length of the roughness, as calculated from the model in appendix B. From this value n_S is calculated, assuming $l_S \approx l$.
- n_S and l_L as [80]

$$n_S = \frac{1}{2l_S a}, \tag{C.8}$$

$$l_L = 2l_S \left(\frac{\sqrt{2\pi n_S} v_F}{\omega_0} \right)^4 . \tag{C.9}$$

- B_{perc}, B_{cross} using the formulae given above, with a, n_S and l_L.
- B_{ad} is assumed to be much larger than the other fields scales, assuming the correlation length of the smooth potential to be much longer than the other length scales.

The quadratic approximation describes the data up to 5 T. Since an analytical expression is not available at higher fields, we only note, comparing figure C.3 with the data, that the model qualitatively reproduces the data.

Smooth random potential When the electron gas moves in a smooth random potential whose correlation length is Λ, a positive magnetoresistance is found [79]; when $\omega_c\tau \ll (l/\Lambda)^{2/3}$ it is given by

$$\frac{\rho(B)}{\rho_0} = \frac{2\zeta(3/2)}{\pi} \left(\frac{\Lambda}{l} \right)^3 (\mu B)^{9/2} \tag{C.10}$$

where $\zeta(x)$ is the Riemann Zeta function, and $\zeta(3/2) \simeq 2.612$.

This positive contribution to magnetoresistance has to be added to the negative term described in the previous section; because of the power-law dependence as $B^{9/2}$, the positive term is relevant at higher fields than the negative term.

The positive magnetoresistance at high field at 0.25 K (figure C.2) can be explained, at least qualitatively, as due to this origin.

C.3 Sample B

Figure C.5 reports the extracted magnetoresistance background for sample B. The Lorenz gas model is also shown in the figure. It reproduces the negative magnetoresistance of the data only qualitatively. The other models described in the previous section can be applied only for field larger than $B_\tau = 2\pi/\mu_t$; in this sample its value is 13 T, which is beyond the experimental range.

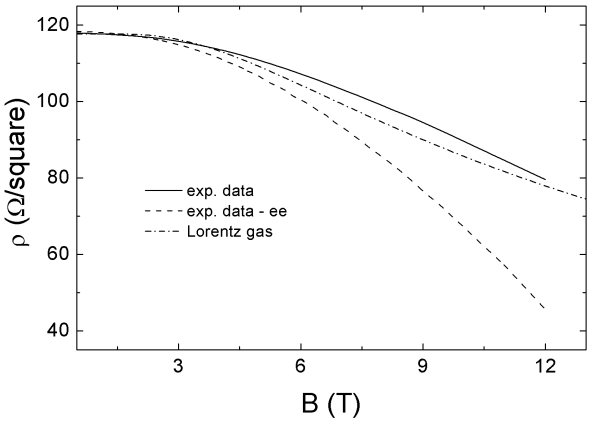

Fig. C.5: Extracted magnetoresistance background for Sample B (solid line) and background after the subtraction of the electron-electron interaction correction (dashed line). The dash-dot line represents the Lorentz gas model.

D. NUMERICAL EVALUATION OF THE WEAK ANTILOCALISATION

The models of Zduniak *et al.*, Miller *et al.* and Golub, described in section 3.3.1, require a numerical evaluation. In this appendix, I will report on how this problem can be approached.

Chronologically, I ran first into the models by Miller and Zduniak; as described below, the integrals P_N involved in them can be calculated using a composition of different methods, as proposed by McPhail *et al.* [76]; for these models, I applied directly this technique. Later, I had to deal with the Golub model, which involves other integrals in addition to P_N. For their evaluation, I have developed another calculation procedure, which could be applied also to P_N; it is simpler in the implementation, but slower in the execution.

These algorithms were implemented in PYTHON, using the packages NUMPY (for array handling), NUMEXPR (which boosts numerical evaluations involving very large arrays), MPMATH (for arbitrary precision arithmetic and special functions), and SCIPY.WEAVE to include C/C++ code. For algebraic manipulations and model fitting the MATHEMATICA software was utilised.

D.1 Evaluation of the Cooperon term

Both Zduniak and Miller models describe the weak antilocalisation in terms of the Cooperon function

$$C(x,z) = x \sum_{N=0}^{\infty} \frac{P_N^3(x,z)}{1 - P_N(x,z)}, \tag{D.1}$$

where $P_N(x,z)$ is

$$P_N(x,z) = \sqrt{\frac{2}{x}} \int_0^{\infty} \exp\left(-\sqrt{\frac{2}{x}}(1+z)t - \frac{t^2}{2}\right) L_N\left(t^2\right) \mathrm{d}t, \tag{D.2}$$

$L_N(t)$ being the N-th Laguerre polynomial. Here, x is related to the magnetic field, and z to the phase and spin relaxation. To simplify the notation, it is possible to define $s = (1+z)\sqrt{2/x}$, so

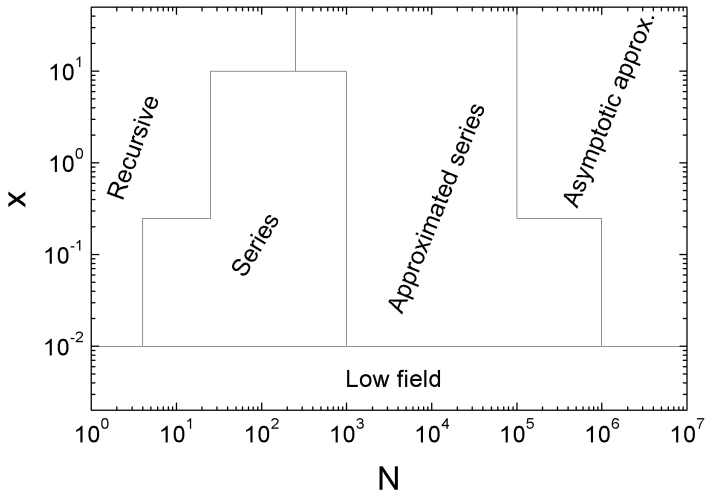

Fig. D.1: Diagram of the evaluation methods of P_N.

that the integral to be evaluated is

$$P_N = \frac{s}{1+z} \int_0^\infty \exp(-st - t^2/2) L_N(t^2) \mathrm{d}t. \tag{D.3}$$

It is found that both the integral and the series are slowly converging, so that their numerical evaluation can be tricky [77]. Kawabata [59] gives a recursive formula for P_N; however, this formula needs a very high numerical precision at large N and small x. Wittmann and Schmid [110] use a series expansion of P_N, which results to be not very accurate at small x. For a review of these methods and their limits, see Ref. [76, app. B].

Miller [77] proposed a procedure suitable for the use of these formulae in the case of a least-square fit, i.e., when several values of the parameters x and z have to be explored: he calculates the Cooperon for a wide range of the parameters space, and uses this table for the function evaluation. In the present work, this approach has been applied: a table of the values of the series in equation (D.1) was evaluated for a several values of x and z, and used through linear interpolation. The values in the table were evaluated following the method described by McPhail *et al.* [76]: P_N is evaluated using the most suitable technique for the different values of x, z and N. In particular, the recursion relation is applied only up to a small N, and then the faster series approximation is applied. The series is then evaluated up to a (large) N_{max}, and then with an asymptotic formula. The numerical results from this algorithm have been checked with the curves reported in Refs. [76, 113].

The different approximations are summarised in figure D.1 and listed below. The employed formulae are described in the following. Note that the value of z is ignored in choosing the technique, because the evaluation reveals to be not very sensitive to it.

- $x \leq 0.01$: approximated with the zero-field value

- $0.01 < x \leq 0.25$:
  - $N \leq 4$: Kawabata recursive formula
  - $5 \leq N \leq 1000$: series approximation
  - $1000 < N \leq 1000000$: approximated series
  - $N > 1000000$: asymptotic approximation
- $0.25 < x \leq 10$:
  - $N \leq 25$: Kawabata recursive formula
  - $26 \leq N \leq 1000$: series approximation
  - $1000 < N \leq 1000000$: approximated series
  - $N > 100000$: asymptotic approximation
- $x > 10$:
  - $N \leq 250$: Kawabata recursive formula
  - $251 \leq N \leq 100000$: approximated series
  - $N > 100000$: asymptotic approximation

Low field approximation At very low field, the theory of weak localisation (section 3.3) predicts that the conductivity is constant at the zero-field value for $B \ll B_\varphi$; this approximation can be applied to the evaluation of the Cooperon, since the weak localisation conductivity is proportional to it (see equation (4.41), page 82). The numerical evaluation of the Cooperon at low field is shown in figure D.2, together with the zero field limit. The constant value is given by

$$C(0, z) = \ln\left(1 + \frac{1}{z}\right). \tag{D.4}$$

Kawabata recursive formula Referring to equation (D.3), and defining $\Psi_N = P_N(1 + z)/s$, the recursive formula is given by [59]

$$\Psi_{N+1} = \frac{1}{N+1}\left[2\sum_{n=0}^{N-1}\Psi_N - (2N + s^2)\Psi_N - N\Psi_{N-1} + s\right], \tag{D.5}$$

with

$$\Psi_0 = \sqrt{\frac{\pi}{2}}\exp\left(\frac{s^2}{2}\right)\operatorname{erfc}\left(\frac{s}{2}\right), \tag{D.6}$$

$\operatorname{erfc}(x)$ being the error function. The "seed" Ψ_0 needs to be calculated with the highest precision, since the stability of the recursion is very sensitive to the initial value.

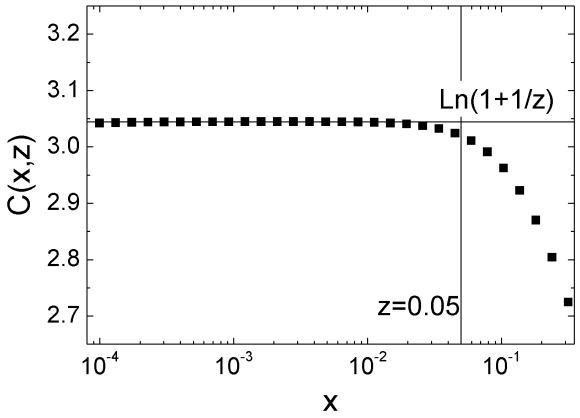

Fig. D.2: Numerical evaluation of the Cooperon at small x, for z=0.05. The horizontal line marks the zero-field value, the vertical line the z value.

Series approximation The series expansion for P_N, developed by Wittmann and Schmid [110], reads

$$P_N = \frac{1}{(1+z)^2}\frac{1}{\sqrt{1+(2N+1)x}}\sum_{k=0}^{\infty} M_N^k \frac{(-1)^k}{2^k k!}\left(\frac{1}{2}\right)_k \left[\frac{x}{1+(2N+1)x}\right]^k, \tag{D.7}$$

where $(a)_k = \Gamma(a+k)/\Gamma(a)$ is the Pochhammer symbol and $\Gamma(x)$ the gamma function; the series can be safely truncated at small k; according to the original work, the maximum k is set to 7. The coefficients M_N^k are given by:

$$M_N^k = (-1)^k \frac{d^k}{dp^k}\left\{\frac{(1-p)^N}{2p^{N+1}}\exp\left[(4N+2)(p-1/2)\right]\right\}\Bigg|_{p=1/2}. \tag{D.8}$$

The coefficients up to $k = 7$ are

$$\begin{aligned} &M_N^0 = 1, \quad M_N^1 = 0, \quad M_N^2 = 4, \\ &M_N^3 = 8(4N+2), \quad M_N^4 = 144, \quad M_N^5 = 704(4N+2) \\ &M_N^6 = 640(4N+2)^2 + 14400, \quad M_N^7 = 118656(4N+2). \end{aligned} \tag{D.9}$$

Approximated series At large N, the sum is calculated using the approximation

$$P_N \approx \frac{1}{\sqrt{x+2xN+(1+z)^2}}. \tag{D.10}$$

Large N asymptotic At very large N, $P_N \ll 1$; using the equation (D.10), the series can be

rewritten using the Hurwitz zeta function as

$$\sum_{N=N_L}^{\infty} \frac{P_N^3(x,z)}{1-P_N(x,z)} \approx \sum_{N=N_L}^{\infty} P_N^3(x,z) = \frac{1}{(2x)^{3/2}} \zeta\left(\frac{3}{2}, \frac{(1+z)^2}{2x} + \frac{1}{2} + N_L\right). \tag{D.11}$$

D.2 Evaluation of the Golub model

The Golub model [50] requires the evaluation of the integrals given in equations (4.45), page 84. They can be all rewritten in terms of the function

$$A(m,N,s) = \frac{1}{\sqrt{(N+1)_m}} \int_0^{\infty} \exp(-st - t^2/2) t^m L_N^{(m)}\left(t^2\right) \mathrm{d}t, \tag{D.12}$$

where $(N+1)_m$ is the rising factorial (or Pochhammer symbol, equal to 1 if $m = 0$).

The trigonometric identity $\sin^2 x = (1 - \cos(2x))/2$ can be applied to $S_N^{(m)}$. The integrals with the sine and cosine can then be calculated as real and imaginary parts of an integral with an exponential function with imaginary argument.

The integrals to be calculated are then given by

$$P_N = \sqrt{\frac{2}{x}} A\left(0, N, \sqrt{\frac{2}{x}}(1+z)\right), \tag{D.13a}$$

$$Q_N = \sqrt{\frac{2}{x}} A\left(1, N, \sqrt{\frac{2}{x}}\right), \tag{D.13b}$$

$$R_N^{(m)} = \sqrt{\frac{1}{x}} \mathrm{Imag}\left[A\left(m, N, \sqrt{\frac{2}{x} - 2i\Omega\tau}\right)\right], \tag{D.13c}$$

$$S_N^{(m)} = \frac{1}{2}\sqrt{\frac{2}{x}}\left\{A\left(m, N, \sqrt{\frac{2}{x}}\right) - \mathrm{Real}\left[A\left(m, N, \sqrt{\frac{2}{x} - 2i\Omega\tau}\right)\right]\right\}. \tag{D.13d}$$

For the numerical implementation, it is useful to rewrite the Laguerre polynomials in equation (D.12) using its properties.

The N-th generalised Laguerre polynomials $L_N^{(m)}(t^2)$ is

$$L_N^{(m)}(t^2) = \sum_{k=0}^{N} (-1)^k \binom{N+m}{N-k} \frac{t^{2k}}{k!}. \tag{D.14}$$

Thus, the integral in equation (D.12) can be rewritten as a sum of integrals involving only

powers and exponential functions. The result is

$$A(m,N,s) = \sum_{k=0}^{N} \binom{N+m}{N-k} \left[(-1)^k \, 2^{-1-k-\frac{m}{2}} (k+1)_{m+1} s \, U\left(1+k+\frac{m}{2}, \frac{3}{2}, \frac{s}{2}\right)\right], \tag{D.15}$$

where $U(a,b,z)$ is the confluent hypergeometric function of the second kind.

The terms in equation (D.15) in square brackets are independent of N, and can be calculated only once (for a given s), and then summed (after multiplication with the binomial coefficients) to yield the N-th term.

This formula could be applied for every value of N. With the use of this formula, the recursion relation described in the previous section is not needed, to bypass the requirements of the high precision initial value. However, for large N, it is possible to use an asymptotic approximation [48, 21], which leads to a simpler formula. In my implementation the approximation has been applied for $N > 25$.

In the limit $N \to \infty$, the Laguerre polynomial is [1, eq. 13.8.9]

$$L_N^{(m)}\left(t^2\right) \approx \binom{N+m}{N} m! \exp\left(t^2/2\right) \left(\frac{m+1}{2}+N\right)^{-\frac{m}{2}} t^{-m} J_m\left(\sqrt{2(1+m+2N)}t\right), \tag{D.16}$$

where $J_m(z)$ is the Bessel function. The integral in equation (D.12) is given by [1, eqs. 10.22.49 and 15.4.18]

$$\begin{aligned} A(m,N,s) &\approx \sqrt{(N+1)_m} \left(\frac{m+1}{2}+N\right)^{-\frac{m}{2}} \int_0^\infty \exp(-st) J_m\left(\sqrt{2(1+m+2N)}t\right) \mathrm{d}t = \\ &= \sqrt{(N+1)_m} 2^m \frac{\left(s+\sqrt{s^2+2+2m+4N}\right)^{-m}}{\sqrt{s^2+2+2m+4N}}. \end{aligned} \tag{D.17}$$

Once the integrals are calculated, the terms are inserted in the matrices in equation (4.44) and then summed as in equation (4.43); the infinite sum is truncated at a large integer ($N_{max} = 5 \cdot 10^5$ is chosen). As before, the weak antilocalisation correction has been calculated for a region in the parameters space, and interpolations of the calculated values are used for fitting. I noted that the table of calculated conductance should be dense with respect to the parameter $\Omega\tau$ to have a good approximation through interpolation, while the interpolation seems less sensitive to the density of x and z.

At small x ($x < 0.1$), it is convenient to use the low field approximation given by Golub in Ref. [50].

Finally, I report in figure D.3 the calculated values of the integral P_N and their evaluation time, at different values of N, using a numerical integration (referred as "exact" integral), the

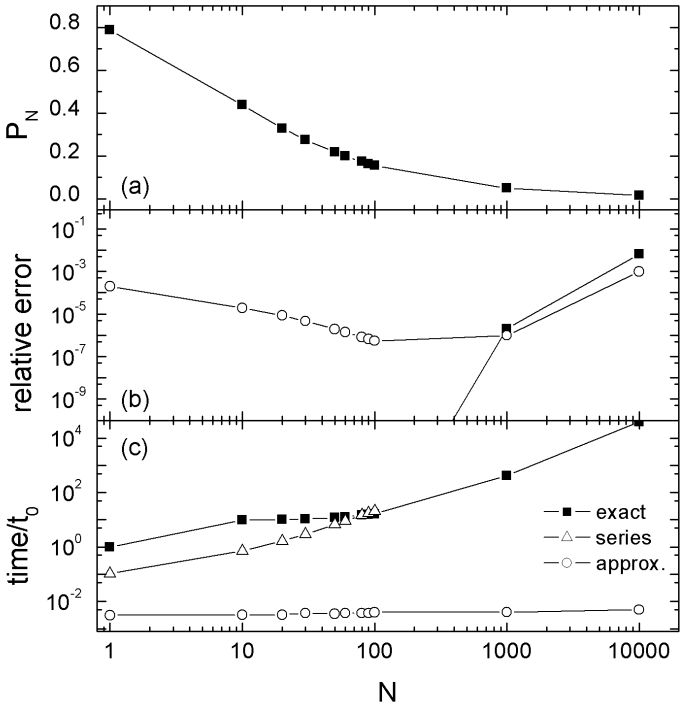

Fig. D.3: Comparison of different methods for the evaluation of the integral P_N (see text for details) at different values of N. (a) Value of the integral, calculated with numerical quadrature ("exact" value). (b) Relative error of the numerical evaluation and of the approximated formula (as compared with the numerical result). (c) Evaluation time for numerical, series and approximated method; t_0 is the time of the exact evaluation of P_1.

formula (D.15) (referred as "series") and the formula (D.17) (referred as "approximation"), at $x = 0.2$ and $z = 0.01$.

The numerical integration was performed using the `quad` function in the MPMATH package, which uses a "tanh-sinh" method, with 60 decimal digits precision.

I report in panel (b) the relative error referred to the exact integral, defined as $|P_N^{(appr)} - P_N^{(exact)}|/P_N^{(exact)}$, where $P_N^{(appr)}$ is the approximated calculation and $P_N^{(exact)}$ the numerical result. The relative error in the numerical integration (evaluated by the quadrature function itself) is reported in the graph only for the largest values of N, since it is much smaller at small N ($< 10^{-30}$ for $N < 50$, $< 10^{-16}$ for $N \leq 100$).

The series method is found to be numerically unstable for $N > 50$, probably because of the large integers calculations due to the factorials involved in it; in the region where the formula works, it gives the same value as the "exact" integration, within the error in the numerical integration.

The error in the large N approximation is expected to decrease with N, but it is found to rise at the largest N: this is due actually to the error in the "exact" value, which is shown to be very large at this large N values. The error of the approximation is smaller than 10^{-3} even at small N, and can be estimated to decrease as $0.01N^{-3/2}$.

Finally, consider the evaluation time for the different methods, reported in figure D.3c. They are normalised to the evaluation time of $P_1^{(exact)}$. Both the exact and the series times are increasing with N, the series being a little faster. The approximated function is much faster (more than 100 times), and nearly constant with N.

E. EXPERIMENTS ON GAN ONE DIMENSIONAL DEVICES

Devices for the study of one-dimensional transport were fabricated on Sample A. These measurements can demonstrate the quality of the 2DEG, and also give further information on the scattering mechanisms assumed to be effective in the sample.

These devices, the so-called quantum point contacts (QPCs), have the split-gate design. Two gate electrodes are fabricated (by electron beam lithography) close to each other; a negative bias applied to them locally depletes the 2DEG and only a narrow channel is open to the electron flow. In the constriction, electrons are free to move only in one direction, being confined by a potential well in the transverse direction: their energy spectrum has, therefore, quantised subbands (modes). The energy spectrum of such one-dimensional system [41, chap. 2] can be calculated similarly to the 2DEG spectrum, as described in section 1.1.

The lateral confinement is provided by a potential $U(x)$; the electrons flow in the y direction. The energy eigenvalues are

$$E_{nm}(k_y) = \frac{\hbar^2 k_y^2}{2m} + E_m + \epsilon_n, \tag{E.1}$$

where ϵ_n is the eigenvalue of the z part of the Schrödinger equation (the quantum well) and E_m that of the x part. For a fixed value of ϵ_n (usually only the first level of the quantum well is occupied), the spectrum is a sequence of modes with quadratic dispersion relations.

The transport through the 1D channel occurs via these discrete modes [41, chap. 3]. The conductance G is proportional to the number of modes M passing across the channel, and is calculated using the Landauer-Büttiger formula

$$G = g_s \frac{e^2}{h} M, \tag{E.2}$$

where $g_s = 2$ counts the degeneracy. The quantity $G_0 = 2e^2/h$ is referred as quantum of conductance. This phenomenon is called “quantisation of conductance”. In a split-gate device, the voltage applied to the gates tunes the number of the modes by modulating the confinement potential.

The above formula assumes the full transmission of all the modes. If the i-th mode has a

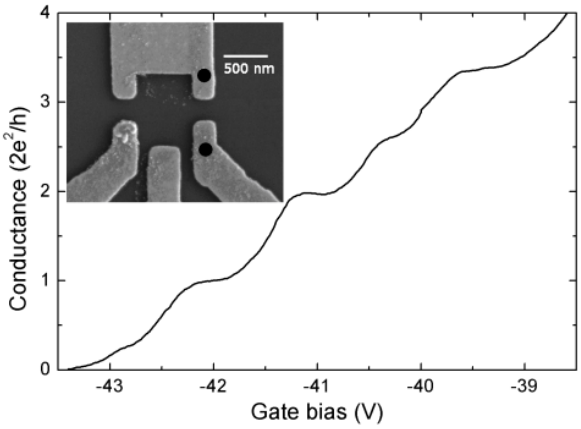

Fig. E.1: Linear conductance as a function of gate voltage in a quantum point contact. The measurement was performed at T = 0.3 K. Inset: scanning electron microscopy of the device. The quantum point contact was defined by biasing the gates marked by circles.

transmission probability T_i, then the formula is

$$G = g_s \frac{e^2}{h} \sum_i T_i. \tag{E.3}$$

Figure E.1 reports the linear conductance as a function of gate bias in a QPC, whose scanning electron microscopy image is shown in the inset; the gate voltage was applied to the electrodes marked with a circle.

Two well-defined plateaus are visible at G_0 and $2G_0$, corresponding to one and two propagating modes, respectively. The length of the plateau is proportional to the energy separation of the modes.

Plateaus at higher values are found at non-perfectly quantised conductance values: this finding may be simply due to a reduction of transmission because of scattering centres.

We cannot clearly observe the so-called 0.7 anomaly [100][41, chap. 5], an additional plateau at $0.7G_0$, which is generally attributed to electron-electron interactions. It is possible that in our high density 2DEG these interactions are screened and thus the observation of the anomaly is precluded. Indeed, these interactions are parametrised by the adimensional radius $r_s = m/(\varepsilon_r a_B \sqrt{\pi n_{2D}})$, where m is the effective mass in units of the electron mass, ε_r the relative permittivity, a_B the Bohr radius and n_{2D} the carrier density; the larger is r_s, the stronger is the interaction. In the investigated system (GaN, $m = 0.22$, $\varepsilon_r = 10$, and $n_s \approx 10^{17}$ m^{-2}), $r_s \approx 0.7$, while in sample where this phenomenon is observed it is larger (e.g., Ref. [100], GaAs, $m = 0.067$, $\varepsilon_r = 13$, and $n_s \approx 10^{15}$ m^{-2}, $r_s \approx 1.4$).

To study the scattering in more detail, a configuration where voltage difference is applied to the two gates was used (asymmetric voltage configuration).

This configuration allows to move the channel laterally with respect to the gate electrodes

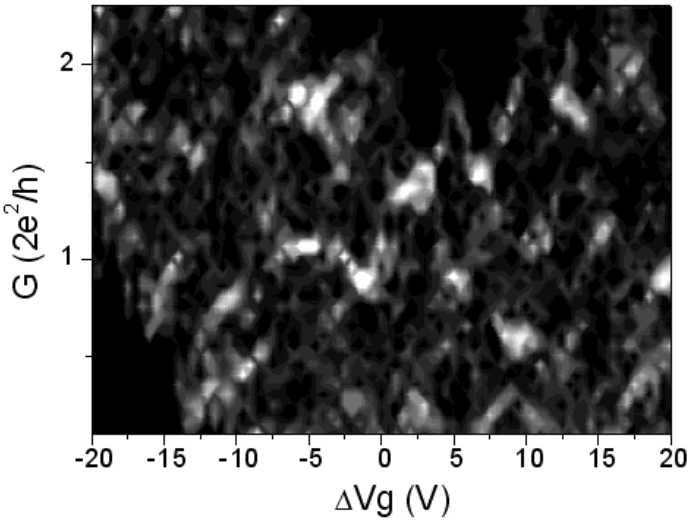

Fig. E.2: Map of the conductance histograms as a function of gate voltage asymmetry and conductance; the grey scale is calculated from the number of points per conductance value: white corresponds to high counts (plateaus), black to low counts. Temperature of the measurements was equal to 0.25 K. Conductance measurements were acquired in a different run respect to the ones reported in figure E.1.

[108]. In this manner, scattering centres, if any, will affect the conductance plateau values differently for different lateral position of the channel.

The results of these measurements are reported in figure E.2, which shows in grey scale the conductance histograms, i.e. the number of points per each conductance value from measurements as a function of gate voltage at different values of the voltage asymmetry. The peak values correspond to plateaus. The positions of the peaks (and thus the conductance values of the plateaus) move as a function of the asymmetric bias, suggesting the presence of scattering effects in our material

This kind of device was investigated also with magnetotransport measurements.

When a magnetic field perpendicular to the 2DEG is applied, an effective confining potential appears in the hamiltonian, as described in section 1.1.1; it sums to the lateral potential $U(x)$. In the simplest approximation, $U(x)$ is a harmonic potential with angular frequency ω_0: in this case the effective potential is that of a harmonic oscillator, with angular frequency $\omega(B) = (\omega_0^2 + \omega_c^2)^{1/2}$, where $\omega_c = eB/m$ is the cyclotron frequency. Then, as a function of the magnetic field, the spacing between the modes widens, and the plateaus become wider as a function of the gate voltage.

The relative increase in the energy separation as a function of the magnetic field can be written as

$$\frac{\hbar\omega(B) - \hbar\omega_0}{\hbar\omega_0} = \sqrt{1 + \frac{\omega_c^2}{\omega_0^2}} - 1 = \sqrt{1 + \frac{B^2}{B_0^2}} - 1, \tag{E.4}$$

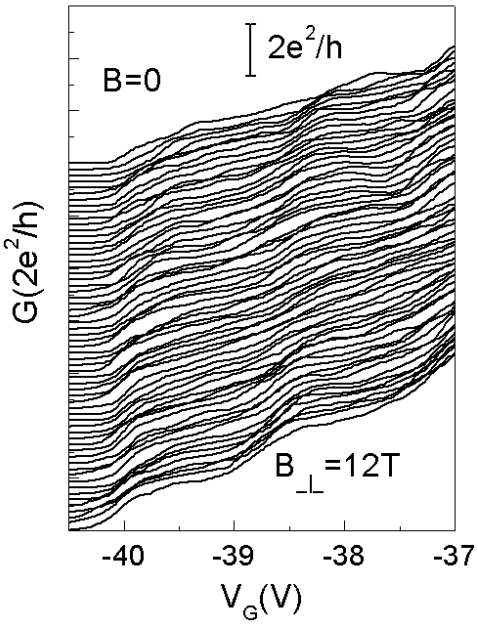

Fig. E.3: Conductance as a function of the gate voltage at different values of the perpendicular magnetic field at 0.25 K. Curves are vertically shifted for clarity.

where $B_0 = m\omega_0/e$.

In figure E.3 a set of measurements on the split gate device at magnetic fields up to 12 T is reported. As the magnetic field intensity increases, we cannot see the plateaus become significantly wider. This suggests that the confining potential is much stronger than the magnetic confinement ($\omega_0 \gg \omega_c$), and then the effect of the field is negligible ($\omega(B) \approx \omega_0$).

The strong confinement potential can be provided by the "network of channels" which were assumed to explain the quadratic Dingle plot in the discussion of Shubnikov–deHaas measurements (section 4.2.3.2). A picture of this kind of system is shown in figure E.4.

The width Λ of these channels has been estimated, from the transport measurements (see section 4.2.4 and appendix B) to be of the order of 5 nm. From this value, an estimation of ω_0 can be given, assuming that n levels are confined in the well, comparing a potential $U(x) = m\omega_0^2 x^2/2$ at $\Lambda/2$ and the value of the n-th energy level of the harmonic potential:

$$\frac{1}{2}m\omega_0^2\left(\frac{\Lambda}{2}\right)^2 = \left(n-\frac{1}{2}\right)\hbar\omega_0 \quad \Rightarrow \quad \omega_0 = \frac{8\hbar}{m\Lambda^2}\left(n-\frac{1}{2}\right),\ B_0 = \frac{8\hbar}{e\Lambda^2}\left(n-\frac{1}{2}\right). \tag{E.5}$$

If only the first level is considered, for $\Lambda = 5$ nm, $B_0 \approx 100$ T. Thus, at 12 T, the increase calculated with equation (E.4) is less than 1%.

Referring to the experimental data, the plateau length (which proportional to the energy separation) is about 1 V, while the transition region between two plateaus is about 0.5 V; thus, the effect of magnetic field can be hardly visible.

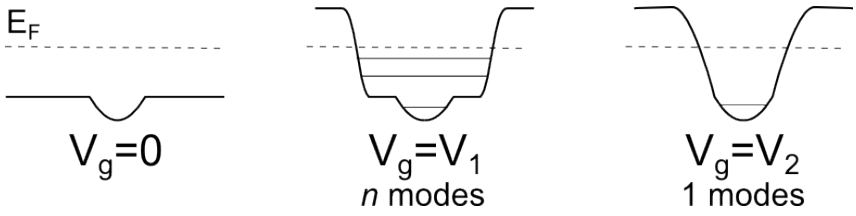

Fig. E.4: Sketch of the QPC potential profile for different applied gate voltage with a further confinement due to an impurity potential.

We can discuss this transport through small channels also in connection with the measurements with asymmetric voltage.

When the two gates are biased such as they deplete the 2DEG underneath, only a few of these channels, in the middle of the gates, will be opened. When the constriction between the two depletion regions is of the order of some correlation lengths, the electron can flow in only a single channel (see figure E.4). In such a narrow constriction the quantisation of conductance is observed. The effect of an asymmetric bias is to change the particular channel where the conduction occurs, which may have a different transmission coefficient, and thus give a peak at a different position in the map in figure E.2.

BIBLIOGRAPHY

[1] *Digital Library of Mathematical Functions*. National Institute of Standards and Technology, 2011. URL `http://dlmf.nist.gov`. Cited on page(s): 120

[2] M. Ahoujja, W. Mitchel, S. Elhamri, R. Newrock, D. Mast, J. Redwing, M. Tischler, and J. Flynn. Transport coefficients of AlGaN/GaN heterostructures. *Journal of Electronic Materials*, 27(4):210, Apr. 1998. doi: 10.1007/s11664-998-0389-4. Cited on page(s): 34

[3] R. L. Allen and D. W. Mills. *Signal Analysis*. John Wiley & Sons, Inc., Dec. 2003. ISBN 0471234419. doi: 10.1002/047166037X. Cited on page(s): 102

[4] O. Ambacher. Growth and applications of Group III-nitrides. *Journal of Physics D: Applied Physics*, 31(20):2653–2710, 1998. ISSN 0022-3727. doi: 10.1088/0022-3727/31/20/001. Cited on page(s): 3

[5] O. Ambacher, J. Smart, J. R. Shealy, N. G. Weimann, K. Chu, M. Murphy, W. J. Schaff, L. F. Eastman, R. Dimitrov, L. Wittmer, M. Stutzmann, W. Rieger, and J. Hilsenbeck. Two-dimensional electron gases induced by spontaneous and piezoelectric polarization charges in N- and Ga-face AlGaN/GaN heterostructures. *Journal of Applied Physics*, 85 (6):3222–3233, Mar. 1999. doi: 10.1063/1.369664. Cited on page(s): 5, 6, 7, 9

[6] O. Ambacher, B. Foutz, J. Smart, J. R. Shealy, N. G. Weimann, K. Chu, M. Murphy, A. J. Sierakowski, W. J. Schaff, L. F. Eastman, R. Dimitrov, A. Mitchell, and M. Stutzmann. Two dimensional electron gases induced by spontaneous and piezoelectric polarization in undoped and doped AlGaN/GaN heterostructures. *Journal of Applied Physics*, 87(1): 334–344, Jan. 2000. doi: 10.1063/1.371866. Cited on page(s): 3, 4, 6

[7] T. Ando, A. B. Fowler, and F. Stern. Electronic properties of two-dimensional systems. *Reviews of Modern Physics*, 54(2):437, Apr. 1982. doi: 10.1103/RevModPhys.54.437. Cited on page(s): 1, 55, 56

[8] A. G. Aronov and Y. B. Lyanda-Geller. Spin-orbit Berry phase in conducting rings. *Physical Review Letters*, 70(3):343, Jan. 1993. doi: 10.1103/PhysRevLett.70.343. Cited on page(s): 43

[9] D. D. Awschalom and M. E. Flatté. Challenges for semiconductor spintronics. *Nature Physics*, 3(3):153, 2007. ISSN 1745-2473. doi: 10.1038/nphys551. Cited on page(s): v

[10] R. S. Balmer, K. P. Hilton, K. J. Nash, M. J. Uren, D. J. Wallis, D. Lee, A. Wells, M. Missous, and T. Martin. Analysis of thin AlN carrier exclusion layers in AlGaN/GaN microwave heterojunction field-effect transistors. *Semiconductor Science and Technology*, 19(6):L65–L67, 2004. ISSN 0268-1242. doi: 10.1088/0268-1242/19/6/L02. Cited on page(s): 9

[11] Y. N. Barabanenkov, Y. A. Kravtsov, V. D. Ozrin, and A. I. Saichev. Enhanced backscattering: the universal wave phenomenon. *Proceedings of the IEEE*, 79(10):1367–1370, Oct. 1991. ISSN 0018-9219. doi: 10.1109/5.104211. Cited on page(s): 39

[12] C. Beenakker and H. van Houten. Quantum Transport in Semiconductor Nanostructures. *Solid State Physics*, 44:1–228, 1991. doi: 10.1016/S0081-1947(08)60091-0. Cited on page(s): 49

[13] A. E. Belyaev, V. G. Raicheva, A. M. Kurakin, N. Klein, and S. A. Vitusevich. Investigation of spin-orbit interaction in AlGaN/GaN heterostructures with large electron density. *Physical Review B*, 77(3):035311, Jan. 2008. doi: 10.1103/PhysRevB.77.035311. Cited on page(s): 24

[14] G. Bergmann. Weak anti-localization: An experimental proof for the destructive interference of rotated spin 1/2. *Solid State Communications*, 42(11):815–817, June 1982. ISSN 00381098. doi: 10.1016/0038-1098(82)90013-8. Cited on page(s): 39

[15] G. Bergmann. Weak localization in thin films: a time-of-flight experiment with conduction electrons. *Physics Reports*, 107(1):1, May 1984. doi: 10.1016/0370-1573(84)90103-0. Cited on page(s): 38, 40, 44

[16] S. Brosig, K. Ensslin, R. J. Warburton, C. Nguyen, B. Brar, M. Thomas, and H. Kroemer. Zero-field spin splitting in InAs-AlSb quantum wells revisited. *Physical Review B*, 60 (20):R13989, Nov. 1999. doi: 10.1103/PhysRevB.60.R13989. Cited on page(s): 71

[17] D. Brunner, H. Angerer, E. Bustarret, F. Freudenberg, R. Höpler, R. Dimitrov, O. Ambacher, and M. Stutzmann. Optical constants of epitaxial AlGaN films and their temperature dependence. *Journal of Applied Physics*, 82(10):5090, 1997. ISSN 00218979. doi: 10.1063/1.366309. Cited on page(s): 8

[18] M. G. Burt. The justification for applying the effective-mass approximation to microstructures. *Journal of Physics: Condensed Matter*, 4:6651, 1992. doi: 10.1088/0953-8984/4/32/003. Cited on page(s): 1

[19] Y. A. Bychkov and E. I. Rashba. Oscillatory effects and the magnetic susceptibility of carriers in inversion layers. *Journal of Physics C: Solid State Physics*, 17(33):6039–6045, 1984. ISSN 0022-3719. doi: 10.1088/0022-3719/17/33/015. Cited on page(s): 14

[20] M. Cahay and S. Bandyopadhyay. Phase-coherent quantum mechanical spin transport in a weakly disordered quasi-one-dimensional channel. *Physical Review B*, 69(4):045303, Jan. 2004. doi: 10.1103/PhysRevB.69.045303. Cited on page(s): v

[21] A. Cassam-Chenai and B. Shapiro. Two dimensional weak localization beyond the diffusion approximation. *Journal de Physique I*, 4(10):11, 1994. doi: 10.1051/jp1:1994103. Cited on page(s): 120

[22] H. Cheng, N. Biyikli, Ü. Özgür, Ç. Kurdak, H. Morkoç, and V. Litvinov. Measurement of linear and cubic spin-orbit coupling parameters in AlGaN/AlN/GaN heterostructures with a polarization-induced two-dimensional electron gas. *Physica E: Low-dimensional Systems and Nanostructures*, 40(5):1586–1589, Mar. 2008. ISSN 1386-9477. doi: 10.1016/j.physe.2007.09.184. Cited on page(s): 24

[23] H. Cho, G. Gusev, Z. Kvon, V. Renard, J. Lee, and J. Portal. Negative quasiclassical magnetoresistance in a high density two-dimensional electron gas in a $Al_xGa_{1-x}N$/GaN heterostructure. *Physical Review B*, 71(24):245323, June 2005. ISSN 1098-0121. doi: 10.1103/PhysRevB.71.245323. Cited on page(s): 71, 77, 105, 107, 108, 109

[24] K. S. Cho, T. Huang, H. Wang, M. Lin, T. Chen, C. Liang, Y. F. Chen, and I. Lo. Zero-field spin splitting in modulation-doped $Al_xGa_{1-x}N$/GaN two-dimensional electron systems. *Applied Physics Letters*, 86(22):222102, May 2005. doi: 10.1063/1.1929876. Cited on page(s): 24

[25] H. T. Chou, S. Luscher, D. Goldhaber-Gordon, M. J. Manfra, A. M. Sergent, K. W. West, and R. J. Molnar. High-quality quantum point contacts in GaN/AlGaN heterostructures. *Applied Physics Letters*, 86(7):073108, Feb. 2005. doi: 10.1063/1.1862339. Cited on page(s): vii

[26] H. T. Chou, D. Goldhaber-Gordon, S. Schmult, M. J. Manfra, A. M. Sergent, and R. J. Molnar. Single-electron transistors in GaN/AlGaN heterostructures. *Applied Physics Letters*, 89(3):033104, July 2006. doi: 10.1063/1.2226454. Cited on page(s): vii

[27] T. P. Chow and R. Tyagi. Wide bandgap compound semiconductors for superior high-voltage unipolar power devices. *IEEE Transactions on Electron Devices*, 41(8):1481–1483, Aug. 1994. ISSN 0018-9383. doi: 10.1109/16.297751. Cited on page(s): vii

[28] P. T. Coleridge. Inter-subband scattering in a 2D electron gas. *Semiconductor Science and Technology*, 5(9):961–966, 1990. ISSN 0268-1242. doi: 10.1088/0268-1242/5/9/006. Cited on page(s): 65

[29] P. T. Coleridge. Small-angle scattering in two-dimensional electron gases. *Physical Review B*, 44(8):3793, 1991. doi: 10.1103/PhysRevB.44.3793. Cited on page(s): 56

[30] P. T. Coleridge. Correlation lengths for scattering potentials in two-dimensional electron gases. *Semiconductor Science and Technology*, 12(1):22, 1997. Cited on page(s): 55, 60, 61

[31] P. T. Coleridge, R. Stoner, and R. Fletcher. Low-field transport coefficients in GaAs/$Ga_{1-x}Al_xAs$ heterostructures. *Physical Review B*, 39(2):1120, Jan. 1989. doi: 10.1103/PhysRevB.39.1120. Cited on page(s): 55, 56

[32] B. Das, D. C. Miller, S. Datta, R. Reifenberger, W. P. Hong, P. K. Bhattacharya, J. Singh, and M. Jaffe. Evidence for spin splitting in $In_xGa_{1-x}As/In_{0.52}Al_{0.48}As$ heterostructures as $B \rightarrow 0$. *Physical Review B*, 39(2):1411, Jan. 1989. doi: 10.1103/PhysRevB.39.1411. Cited on page(s): 34, 36

[33] S. Datta. *Electronic transport in mesoscopic systems*. Cambridge university press, 2007. ISBN 0-521-59943-1. Cited on page(s): 39, 41, 44

[34] S. Datta and B. Das. Electronic analog of the electro-optic modulator. *Applied Physics Letters*, 56(7):665–667, Feb. 1990. doi: 10.1063/1.102730. Cited on page(s): v, vi, viii

[35] J. H. Davies. *The physics of low-dimensional semiconductors: an introduction*. Cambridge University Press, 1998. ISBN 9780521481489. Cited on page(s): 1, 11, 93

[36] C. Di Castro and R. Raimondi. Disordered Electron Systems. *arXiv:cond-mat/0402203*, Feb. 2004. URL `http://arxiv.org/abs/cond-mat/0402203`. Cited on page(s): 32, 44

[37] A. P. Dmitriev, V. Y. Kachorovskii, and I. V. Gornyi. Nonbackscattering contribution to weak localization. *Physical Review B*, 56(15):9910, Oct. 1997. doi: 10.1103/PhysRevB.56.9910. Cited on page(s): 41

[38] A. Endo and Y. Iye. The Effect of Oscillating Fermi Energy on the Line Shape of the Shubnikov-de Haas Oscillation in a Two-Dimensional Electron Gas. *Journal of the Physical Society of Japan*, 77:064713, 2008. ISSN 0031-9015. doi: 10.1143/JPSJ.77.064713. Cited on page(s): 55, 56, 60

[39] J. Fabian, A. Matos-Abiague, C. Ertler, P. Stano, and I. Zutic. *Semiconductor Spintronics*. arXiv:cond-mat/0711.1461, Nov. 2007. URL http://arxiv.org/abs/0711.1461. Cited on page(s): v, vi, vii, 12, 20

[40] J. Farvacque and Z. Bougrioua. Carrier mobility versus carrier density in $Al_xGa_{1-x}N$/GaN quantum wells. *Physical Review B*, 68(3):035335, July 2003. doi: 10.1103/PhysRevB.68.035335. Cited on page(s): 9

[41] D. K. Ferry, S. M. Goodnick, and J. Bird. *Transport in Nanostructures*. Cambridge University Press, 2nd edition, Sept. 2009. ISBN 0521877482, 9780521877480. Cited on page(s): 44, 54, 123, 124

[42] J. Y. Fu and M. W. Wu. Spin-orbit coupling in bulk ZnO and GaN. *Journal of Applied Physics*, 104(9):093712, 2008. ISSN 00218979. doi: 10.1063/1.3018600. Cited on page(s): 13, 16

[43] H. Fukuyama. Theory of weakly localized regime of the Anderson localizaton in two dimensions. *Surface Science*, 113(1-3):489, 1982. doi: 10.1016/0039-6028(82)90638-0. Cited on page(s): 44

[44] S. D. Ganichev and W. Prettl. Spin photocurrents in quantum wells. *Journal of Physics: Condensed Matter*, 15(20):R935–R983, May 2003. ISSN 0953-8984. doi: 10.1088/0953-8984/15/20/204. Cited on page(s): 20

[45] S. D. Ganichev, U. Rössler, W. Prettl, E. L. Ivchenko, V. V. Bel'kov, R. Neumann, K. Brunner, and G. Abstreiter. Removal of spin degeneracy in p-SiGe quantum wells demonstrated by spin photocurrents. *Physical Review B*, 66(7):075328, 2002. doi: 10.1103/PhysRevB.66.075328. Cited on page(s): 71

[46] S. D. Ganichev, V. V. Bel'kov, L. E. Golub, E. L. Ivchenko, P. Schneider, S. Giglberger, J. Eroms, J. De Boeck, G. Borghs, W. Wegscheider, D. Weiss, and W. Prettl. Experimental Separation of Rashba and Dresselhaus Spin Splittings in Semiconductor Quantum Wells. *Physical Review Letters*, 92(25):256601, June 2004. doi: 10.1103/PhysRevLett.92.256601. Cited on page(s): 14

[47] J. A. Garrido, J. L. Sanchez-Rojas, A. Jimenez, E. Munoz, F. Omnes, and P. Gibart. Polarization fields determination in AlGaN/GaN heterostructure field-effect transistors from charge control analysis. *Applied Physics Letters*, 75(16):2407–2409, Oct. 1999. doi: 10.1063/1.125029. Cited on page(s): 15

[48] M. Glazov and L. Golub. Nondiffusive weak localization in two-dimensional systems with spin-orbit splitting of the spectrum. *Semiconductors*, 40(10):1209, 2006. doi: 10.1134/S1063782606100150. Cited on page(s): 44, 120

[49] M. M. Glazov and L. E. Golub. Spin-orbit interaction and weak localization in heterostructures. *arXiv:0902.2724*, Feb. 2009. URL `http://arxiv.org/abs/0902.2724`. Cited on page(s): 83

[50] L. E. Golub. Weak antilocalization in high-mobility two-dimensional systems. *Physical Review B*, 71(23):235310, June 2005. doi: 10.1103/PhysRevB.71.235310. Cited on page(s): 44, 46, 83, 119, 120

[51] F. Gross. *Relativistic Quantum Mechanics and Field Theory*. Wiley-Interscience, May 1993. ISBN 0471591130. Cited on page(s): 11

[52] G. Grosso and G. P. Parravicini. *Solid state physics*. Academic Press, Mar. 2000. ISBN 9780123044600. Cited on page(s): 27

[53] D. Grundler. Large Rashba Splitting in InAs Quantum Wells due to Electron Wave Function Penetration into the Barrier Layers. *Physical Review Letters*, 84(26):6074, June 2000. doi: 10.1103/PhysRevLett.84.6074. Cited on page(s): vii

[54] J. P. Heida, B. J. van Wees, J. J. Kuipers, T. M. Klapwijk, and G. Borghs. Spin-orbit interaction in a two-dimensional electron gas in a InAs/AlSb quantum well with gate-controlled electron density. *Physical Review B*, 57(19):11911, May 1998. doi: 10.1103/PhysRevB.57.11911. Cited on page(s): vii

[55] S. Hikami, A. I. Larkin, and Y. Nagaoka. Spin-Orbit Interaction and Magnetoresistance in the Two Dimensional Random System. *Progress of Theoretical Physics*, 63(2):707–710, Feb. 1980. ISSN 0033-068X. doi: 10.1143/PTP.63.707. Cited on page(s): 41, 43, 44, 80

[56] S. Iordanskii, Y. Lyanda-Geller, and G. Pikus. Weak-localisation in quantum-wells with spin-orbit interaction. *JETP letters*, 60(3):206, Aug. 1994. ISSN 0021-3640. Cited on page(s): 43, 44, 78

[57] A. Isihara and L. Smrcka. Density and magnetic field dependences of the conductivity of two-dimensional electron systems. *Journal of Physics C: Solid State Physics*, 19:6777, 1986. doi: 10.1088/0022-3719/19/34/015. Cited on page(s): 55, 56

[58] B. Jusserand, D. Richards, H. Peric, and B. Etienne. Zero-magnetic-field spin splitting in the GaAs conduction band from Raman scattering on modulation-doped quantum wells. *Physical Review Letters*, 69(5):848, 1992. doi: 10.1103/PhysRevLett.69.848. Cited on page(s): 20

[59] A. Kawabata. On the Field Dependence of Magnetoresistance in Two-Dimensional Systems. *Journal of the Physical Society of Japan*, 53:3540–3544, 1984. ISSN 0031-9015. doi: 10.1143/JPSJ.53.3540. Cited on page(s): 41, 43, 44, 80, 116, 117

[60] S. Keller, S. Heikman, L. Shen, I. P. Smorchkova, S. P. DenBaars, and U. K. Mishra. GaN–GaN junctions with ultrathin AlN interlayers: Expanding heterojunction design. *Applied Physics Letters*, 80(23):4387–4389, June 2002. doi: 10.1063/1.1484551. Cited on page(s): 8

[61] J. S. Kim, D. G. Seiler, and W. F. Tseng. Multicarrier characterization method for extracting mobilities and carrier densities of semiconductors from variable magnetic field measurements. *Journal of Applied Physics*, 73(12):8324, June 1993. doi: 10.1063/1.353424. Cited on page(s): 29, 32

[62] H. C. Koo, J. H. Kwon, J. Eom, J. Chang, S. H. Han, and M. Johnson. Gate modulation of spin precession in a semiconductor channel. *Journal of Physics D: Applied Physics*, 44(6):064006, Feb. 2011. ISSN 0022-3727. doi: 10.1088/0022-3727/44/6/064006. Cited on page(s): v

[63] A. M. Kreshchuk, S. V. Novikov, T. A. Polyanskaya, I. G. Savel'ev, and A. Y. Shik. Quantum transport effects in a two-dimensional electron gas as a tool for the investigation of heterointerfaces. *Journal of Crystal Growth*, 146(1-4):153–158, Jan. 1995. ISSN 0022-0248. doi: 10.1016/0022-0248(94)00564-8. Cited on page(s): 63

[64] Ç. Kurdak, N. Biyikli, Ü. Özgür, H. Morkoç, and V. I. Litvinov. Weak antilocalization and zero-field electron spin splitting in $Al_xGa_{1-x}N$/AlN/GaN heterostructures with a polarization-induced two-dimensional electron gas. *Physical Review B*, 74(11):113308, 2006. doi: 10.1103/PhysRevB.74.113308. Cited on page(s): 21, 24, 93

[65] D. R. Leadley, R. Fletcher, R. J. Nicholas, F. Tao, C. T. Foxon, and J. J. Harris. Intersubband resonant scattering in GaAs-$Ga_{1-x}Al_xAs$ heterojunctions. *Physical Review B*, 46 (19):12439, Nov. 1992. doi: 10.1103/PhysRevB.46.12439. Cited on page(s): 65

[66] L. C. Lew Yan Voon, M. Willatzen, M. Cardona, and N. E. Christensen. Terms linear in k in the band structure of wurtzite-type semiconductors. *Physical Review B*, 53(16): 10703, Apr. 1996. doi: 10.1103/PhysRevB.53.10703. Cited on page(s): 15

[67] S. B. Lisesivdin, N. Balkan, O. Makarovsky, A. Patane, A. Yildiz, M. D. Caliskan, M. Kasap, S. Ozcelik, and E. Ozbay. Large zero-field spin splitting in AlGaN/AlN/GaN/AlN heterostructures. *Journal of Applied Physics*, 105(9):093701, May 2009. doi: 10.1063/1.3120782. Cited on page(s): 21, 24

[68] V. I. Litvinov. Electron spin splitting in polarization-doped group-III nitrides. *Physical Review B*, 68(15):155314, Oct. 2003. doi: 10.1103/PhysRevB.68.155314. Cited on page(s): 14, 15, 16, 92

[69] V. I. Litvinov. Polarization-induced Rashba spin-orbit coupling in structurally symmetric III-nitride quantum wells. *Applied Physics Letters*, 89(22):222108, Nov. 2006. doi: 10.1063/1.2397559. Cited on page(s): 14

[70] V. I. Litvinov and V. K. Dugaev. Ferromagnetism in Magnetically Doped III-V Semiconductors. *Physical Review Letters*, 86(24):5593, June 2001. doi: 10.1103/PhysRevLett.86.5593. Cited on page(s): vii

[71] I. Lo, J. K. Tsai, W. J. Yao, P. C. Ho, L. Tu, T. C. Chang, S. Elhamri, W. C. Mitchel, K. Y. Hsieh, J. H. Huang, H. L. Huang, and W. Tsai. Spin splitting in modulation-doped $Al_xGa_{1-x}N$/GaN heterostructures. *Physical Review B*, 65(16):161306, Apr. 2002. doi: 10.1103/PhysRevB.65.161306. Cited on page(s): 24

[72] I. Lo, W. T. Wang, M. H. Gau, S. F. Tsay, and J. C. Chiang. Wurtzite structure effects on spin splitting in GaN/AlN quantum wells. *Physical Review B*, 72(24):245329, Dec. 2005. doi: 10.1103/PhysRevB.72.245329. Cited on page(s): 16, 17, 18, 19

[73] I. Lo, M. H. Gau, J. K. Tsai, Y. L. Chen, Z. J. Chang, W. T. Wang, J. C. Chiang, T. Aggerstam, and S. Lourdudoss. Anomalous k-dependent spin splitting in wurtzite $Al_xGa_{1-x}N$/GaN heterostructures. *Physical Review B*, 75(24):245307, June 2007. doi: 10.1103/PhysRevB.75.245307. Cited on page(s): 17, 21, 24, 25, 92

[74] G. D. Mahan. *Many-particle physics*. Physics of solids and liquids. Kluwer/Plenum Publishers, New York, 3rd edition, 2000. ISBN 0-306-46338-5. Cited on page(s): 32

[75] M. J. Manfra, N. G. Weimann, J. W. P. Hsu, L. N. Pfeiffer, K. W. West, S. Syed, H. L. Stormer, W. Pan, D. V. Lang, S. N. G. Chu, G. Kowach, A. M. Sergent, J. Caissie, K. M. Molvar, L. J. Mahoney, and R. J. Molnar. High mobility AlGaN/GaN heterostructures grown by plasma-assisted molecular beam epitaxy on semi-insulating GaN templates prepared by hydride vapor phase epitaxy. *Journal of Applied Physics*, 92(1):338–345, July 2002. doi: 10.1063/1.1484227. Cited on page(s): vii

[76] S. McPhail, C. E. Yasin, A. R. Hamilton, M. Y. Simmons, E. H. Linfield, M. Pepper, and D. A. Ritchie. Weak localization in high-quality two-dimensional systems. *Physical Review B*, 70(24):245311, Dec. 2004. doi: 10.1103/PhysRevB.70.245311. Cited on page(s): 41, 81, 89, 115, 116

[77] J. B. Miller. *Electron Transport in GaAs Heterostructures at Various Magnetic Field Strengths*. PhD thesis, Harvard, 2007. Cited on page(s): 116

[78] J. B. Miller, D. M. Zumbühl, C. M. Marcus, Y. B. Lyanda-Geller, D. Goldhaber-Gordon, K. Campman, and A. C. Gossard. Gate-Controlled Spin-Orbit Quantum Interference

Effects in Lateral Transport. *Physical Review Letters*, 90(7):076807, Feb. 2003. doi: 10.1103/PhysRevLett.90.076807. Cited on page(s): vii, 13, 14, 43, 44, 82

[79] A. D. Mirlin, J. Wilke, F. Evers, D. G. Polyakov, and P. Wölfle. Strong Magnetoresistance Induced by Long-Range Disorder. *Physical Review Letters*, 83(14):2801, Oct. 1999. doi: 10.1103/PhysRevLett.83.2801. Cited on page(s): 112

[80] A. D. Mirlin, D. G. Polyakov, F. Evers, and P. Wölfle. Quasiclassical Negative Magnetoresistance of a 2D Electron Gas: Interplay of Strong Scatterers and Smooth Disorder. *Physical Review Letters*, 87(12):126805, 2001. doi: 10.1103/PhysRevLett.87.126805. Cited on page(s): 109, 112

[81] U. Mishra, S. Likun, T. Kazior, and Y. Wu. GaN-Based RF Power Devices and Amplifiers. *Proceedings of the IEEE*, 96(2):287, 2008. doi: 10.1109/JPROC.2007.911060. Cited on page(s): vii

[82] E. B. Olshanetsky, Z. D. Kvon, S. Sassine, J. C. Portal, H. I. Cho, and J. H. Lee. The weak antilocalization and quantum scattering time in a two-dimensional electron gas in AlGaN/GaN heterostructure. *Applied Physics Letters*, 92(24):242112, 2008. ISSN 00036951. doi: 10.1063/1.2945883. Cited on page(s): 21, 25, 42

[83] A. Potts, R. Shepherd, W. G. Herrenden-Harker, M. Elliott, C. L. Jones, A. Usher, G. A. C. Jones, D. A. Ritchie, E. H. Linfield, and M. Grimshaw. Magnetization studies of Landau level broadening in two-dimensional electron systems. *Journal of Physics: Condensed Matter*, 8:5189, 1996. doi: 10.1088/0953-8984/8/28/004. Cited on page(s): 55

[84] A. Punnoose. Magnetoconductivity in the presence of Bychkov-Rashba spin-orbit interaction. *Applied Physics Letters*, 88(25):252113, June 2006. doi: 10.1063/1.2216027. Cited on page(s): 43, 44, 78, 81

[85] M. E. Raikh and T. V. Shahbazyan. Magnetointersubband oscillations of conductivity in a two-dimensional electronic system. *Physical Review B*, 49(8):5531, Feb. 1994. doi: 10.1103/PhysRevB.49.5531. Cited on page(s): 56, 65

[86] M. L. Reed, N. A. El-Masry, H. H. Stadelmaier, M. K. Ritums, M. J. Reed, C. A. Parker, J. C. Roberts, and S. M. Bedair. Room temperature ferromagnetic properties of (Ga, Mn)N. *Applied Physics Letters*, 79:3473, 2001. ISSN 00036951. doi: 10.1063/1.1419231. Cited on page(s): vii

[87] P. Ruterana, M. Albrecht, and J. Neugebauer, editors. *Nitride semiconductors: handbook on materials and devices*. Wiley-VCH, 2003. ISBN 9783527403875. Cited on page(s): vii

[88] T. H. Sander, S. N. Holmes, J. J. Harris, D. K. Maude, and J. C. Portal. Determination of the phase of magneto-intersubband scattering oscillations in heterojunctions and quantum wells. *Physical Review B*, 58(20):13856, Nov. 1998. doi: 10.1103/PhysRevB.58.13856. Cited on page(s): 65

[89] S. Schmult, M. J. Manfra, A. Punnoose, A. M. Sergent, K. W. Baldwin, and R. J. Molnar. Large Bychkov-Rashba spin-orbit coupling in high-mobility GaN/$Al_xGa_{1-x}N$ heterostructures. *Physical Review B*, 74(3):033302, July 2006. doi: 10.1103/PhysRevB.74.033302. Cited on page(s): 21, 25

[90] L. Shen, S. Heikman, B. Moran, R. Coffie, N. Zhang, D. Buttari, I. Smorchkova, S. Keller, S. DenBaars, and U. Mishra. AlGaN/AlN/GaN high-power microwave HEMT. *IEEE Electron Device Letters*, 22(10):457–459, Oct. 2001. ISSN 07413106. doi: 10.1109/55.954910. Cited on page(s): 8

[91] E. Skuras, R. Kumar, R. Williams, R. Strading, J. Dmochowski, E. Johnson, A. Mackinnon, J. J. Harris, R. Beall, C. Skierbeszewski, J. Singleton, P. van der Wel, and P. Wisniewski. Subband dependent mobilities and carrier saturation mechanisms in thin Si doping layers in GaAs in the high density limit. *Semiconductor Science and Technology*, 6(6):535–546, 1991. ISSN 0268-1242. doi: 10.1088/0268-1242/6/6/023. Cited on page(s): 58

[92] I. P. Smorchkova, L. Chen, T. Mates, L. Shen, S. Heikman, B. Moran, S. Keller, S. P. DenBaars, J. S. Speck, and U. K. Mishra. AlN/GaN and (Al,Ga)N/AlN/GaN two-dimensional electron gas structures grown by plasma-assisted molecular-beam epitaxy. *Journal of Applied Physics*, 90(10):5196–5201, Nov. 2001. doi: 10.1063/1.1412273. Cited on page(s): 8, 49

[93] D. Spirito, G. Frucci, A. Di Gaspare, L. Di Gaspare, E. Giovine, A. Notargiacomo, S. Roddaro, F. Beltram, and F. Evangelisti. Quantum transport in low-dimensional AlGaN/GaN systems. *Journal of Nanoparticle Research*, Nov. 2010. ISSN 1388-0764. doi: 10.1007/s11051-010-0136-7. Cited on page(s): 71

[94] S. Syed, M. J. Manfra, Y. J. Wang, R. J. Molnar, and H. L. Stormer. Electron scattering in AlGaN/GaN structures. *Applied Physics Letters*, 84(9):1507, 2004. ISSN 00036951. doi: 10.1063/1.1655704. Cited on page(s): 63

[95] I. Tan, G. L. Snider, L. D. Chang, and E. L. Hu. A self-consistent solution of Schroödinger–Poisson equations using a nonuniform mesh. *Journal of Applied Physics*, 68(8):4071, 1990. ISSN 00218979. doi: 10.1063/1.346245. Cited on page(s): 70

[96] N. Tang, B. Shen, M. J. Wang, K. Han, Z. J. Yang, K. Xu, G. Y. Zhang, T. Lin, B. Zhu, W. Z. Zhou, and J. H. Chu. Beating patterns in the oscillatory magnetoresistance originated from zero-field spin splitting in $Al_xGa_{1-x}N$/GaN heterostructures. *Applied Physics Letters*, 88(17):172112, Apr. 2006. doi: 10.1063/1.2197313. Cited on page(s): 25, 37

[97] N. Tang, B. Shen, K. Han, F. Lu, F. Xu, Z. Qin, and G. Zhang. Zero-field spin splitting in $Al_xGa_{1-x}N$/GaN heterostructures with various Al compositions. *Applied Physics Letters*, 93(17):172113, Oct. 2008. doi: 10.1063/1.3012361. Cited on page(s): 25

[98] N. Thillosen, S. Cabanas, N. Kaluza, V. A. Guzenko, H. Hardtdegen, and T. Schapers. Weak antilocalization in gate-controlled $Al_xGa_{1-x}N$/GaN two-dimensional electron gases. *Physical Review B*, 73(24):241311, June 2006. doi: 10.1103/PhysRevB.73.241311. Cited on page(s): 21, 25, 90, 91, 93

[99] N. Thillosen, T. Schapers, N. Kaluza, H. Hardtdegen, and V. A. Guzenko. Weak antilocalization in a polarization-doped $Al_xGa_{1-x}N$/GaN heterostructure with single subband occupation. *Applied Physics Letters*, 88(2):022111, Jan. 2006. doi: 10.1063/1.2162871. Cited on page(s): 25

[100] K. J. Thomas, J. T. Nicholls, M. Y. Simmons, M. Pepper, D. R. Mace, and D. A. Ritchie. Possible Spin Polarization in a One-Dimensional Electron Gas. *Physical Review Letters*, 77(1):135, July 1996. doi: 10.1103/PhysRevLett.77.135. Cited on page(s): 124

[101] K. Tsubaki, N. Maeda, T. Saitoh, and N. Kobayashi. Spin splitting in modulation-doped AlGaN/GaN two-dimensional electron gas. *Applied Physics Letters*, 80(17):3126–3128, Apr. 2002. doi: 10.1063/1.1474599. Cited on page(s): 21, 25

[102] I. Žutic, J. Fabian, and S. Das Sarma. Spintronics: Fundamentals and applications. *Reviews of Modern Physics*, 76(2):323, Apr. 2004. doi: 10.1103/RevModPhys.76.323. Cited on page(s): v

[103] W. Wang, C. L. Wu, S. F. Tsay, M. H. Gau, I. Lo, H. F. Kao, D. J. Jang, J. Chiang, M. Lee, Y. Chang, C. Chen, and H. C. Hsueh. Dresselhaus effect in bulk wurtzite materials. *Applied Physics Letters*, 91(8):082110, 2007. doi: 10.1063/1.2775038. Cited on page(s): 16, 17

[104] W. Wang, C. L. Wu, J. C. Chiang, I. Lo, H. F. Kao, Y. C. Hsu, W. Y. Pang, D. J. Jang, M. Lee, Y. Chang, and C. Chen. Spin-degenerate surface and the resonant spin lifetime transistor in wurtzite structures. *Journal of Applied Physics*, 108(8):083718, 2010. ISSN 00218979. doi: 10.1063/1.3484042. Cited on page(s): 16

[105] S. Washburn and R. A. Webb. Quantum transport in small disordered samples from the diffusive to the ballistic regime. *Reports on Progress in Physics*, 55(8):1311–1383, Aug. 1992. ISSN 0034-4885. doi: 10.1088/0034-4885/55/8/004. Cited on page(s): 77

[106] W. Weber, S. D. Ganichev, S. N. Danilov, D. Weiss, W. Prettl, Z. D. Kvon, V. V. Bel'kov, L. E. Golub, H. Cho, and J. Lee. Demonstration of Rashba spin splitting in GaN-based heterostructures. *Applied Physics Letters*, 87(26):262106, Dec. 2005. doi: 10.1063/1.2158024. Cited on page(s): 20

[107] Wikipedia. Spintronics — Wikipedia, The Free Encyclopedia, 2011. URL `http://en.wikipedia.org/w/index.php?title=Spintronics&oldid=447246860`. Accessed 14-September-2011. Cited on page(s): v

[108] J. G. Williamson, C. E. Timmering, C. J. P. M. Harmans, J. J. Harris, and C. T. Foxon. Quantum point contact as a local probe of the electrostatic potential contours. *Physical Review B*, 42(12):7675, Oct. 1990. doi: 10.1103/PhysRevB.42.7675. Cited on page(s): 125

[109] R. Winkler. *Spin-orbit Coupling Effects in Two-Dimensional Electron and Hole Systems*. Springer, 1st edition, Dec. 2003. ISBN 3540011870. Cited on page(s): 12

[110] H. Wittmann and A. Schmid. Anomalous magnetoconductance beyond the diffusion limit. *Journal of Low Temperature Physics*, 69(1-2):131, Oct. 1987. ISSN 0022-2291. doi: 10.1007/BF00681627. Cited on page(s): 41, 116, 118

[111] E. T. Yu, G. J. Sullivan, P. M. Asbeck, C. D. Wang, D. Qiao, and S. S. Lau. Measurement of piezoelectrically induced charge in GaN/AlGaN heterostructure field-effect transistors. *Applied Physics Letters*, 71(19):2794–2796, Nov. 1997. doi: 10.1063/1.120138. Cited on page(s): 7

[112] W. Zawadzki and P. Pfeffer. Spin splitting of subband energies due to inversion asymmetry in semiconductor heterostructures. *Semiconductor Science and Technology*, 19(1): R1–R17, 2004. ISSN 0268-1242. doi: 10.1088/0268-1242/19/1/R01. Cited on page(s): 20

[113] A. Zduniak, M. I. Dyakonov, and W. Knap. Universal behavior of magnetoconductance due to weak localization in two dimensions. *Physical Review B*, 56(4):1996, July 1997. doi: 10.1103/PhysRevB.56.1996. Cited on page(s): 41, 43, 44, 80, 116

[114] Z. W. Zheng, B. Shen, Y. S. Gui, C. P. Jiang, N. Tang, R. Zhang, Y. Shi, Y. D. Zheng, S. L. Guo, G. Z. Zheng, J. H. Chu, T. Someya, and Y. Arakawa. Transport properties of two-dimensional electron gas in different subbands in triangular quantum wells at

$Al_xGa_{1-x}N$/GaN heterointerfaces. *Applied Physics Letters*, 82(12):1872, 2003. ISSN 00036951. doi: 10.1063/1.1557772. Cited on page(s): 70

[115] W. Z. Zhou, T. Lin, L. Y. Shang, L. Sun, K. H. Gao, Y. M. Zhou, G. Yu, N. Tang, K. Han, B. Shen, S. L. Guo, Y. S. Gui, and J. H. Chu. Weak antilocalization and beating pattern in high electron mobility $Al_xGa_{1-x}N$/GaN two-dimensional electron gas with strong Rashba spin-orbit coupling. *Journal of Applied Physics*, 104(5):053703, 2008. doi: 10.1063/1.2974091. Cited on page(s): 21, 25, 90, 91